이학박사학위논문

Terahertz Spectroscopic Study on Hydration Dynamics of the Human Skin

피부의 수화동역학에 대한 테라헤르츠 분광학 연구

2017년 8월

서울대학교 대학원
물리천문학부
백인근

Terahertz Spectroscopic Study on Hydration Dynamics of the Human Skin

피부의 수화동역학에 대한 테라헤르츠 분광학 연구

지도교수 박 건 식

이 논문을 이학박사 학위논문으로 제출함
2017년 6월

서울대학교 대학원
물리천문학부
백인근

백인근의 박사 학위논문을 인준함
2017년 6월

위 원 장 제 원 호 (인)
부위원장 박 건 식 (인)
위 원 김 대 식 (인)
위 원 전 헌 수 (인)
위 원 이 민 걸 (인)

Terahertz Spectroscopic Study on Hydration Dynamics of the Human Skin

In-Keun Baek

Supervised by

Professor Gun-Sik Park

A Dissertation
Submitted to the Faculty of
Seoul National University
In Partial Fulfillment of
the Requirement for the Degree of
Doctor of Philosophy
August 2017

Department of Physics and Astronomy
The Graduate School
Seoul National University

Abstract

The aim of this study is to understand the spectroscopic characteristics of the palm skin in the frequency range of sub-terahertz and terahertz waves and to develop a novel electron beam emitter for compact high power terahertz wave source applicable to the skin in the future. Studies on the human skin have focused primarily on understanding the properties of sub-terahertz and terahertz waves originated from the structural characteristics of the palm skin, as well as changes in dielectric properties of skin layers due to physiological phenomena. The thicknesses of the stratum corneum, epidermis, and dermis, and the structures of the helical sweat glands and fingerprints, which are sub-structures of the palm skin, which can strongly affect the spectrum, were measured using optical coherence tomography. The dielectric constant of each skin layer was estimated using a fitting method based on the Debye dielectric relaxation model. It is also observed that the fingerprint structure has a resonance in the frequency region of terahertz wave and the resonance is modulated by the occlusion. Through the monitoring of the terahertz resonance frequency, the hydration dynamics of the stratum corneum of the fingerprint due to occlusion which occurred when the skin contacts the object were analyzed. Experimental observations of hydration dynamics for each part of the fingerprint structure suggest that the fingerprint structure can influence finger friction through controlling hydration of contact region.

Though, terahertz waves are a very important tool for diagnosing the

physiological characteristics of the skin, lack of a compact high power source for skin research and application is one of the critical issues. To solve this issue, graphene-based electron beam emitter is fabricated for terahertz wave application. The fabricated graphene film can be precisely cut due to its excellent mechanical strength and showed uniform electron beam emission characteristics for a long time period through the edge having high aspect ratio. This graphene-based electron beam emitter will accelerate the realization of compact high power terahertz source applicable to skin as well as existing applications such as field emission displays and electron microscopes.

Keywords : dielectric properties of skin, terahertz spectroscopy, skin hydration, friction ridge, graphene field emission cathode

Student Number : 2009-20412

Contents

I. Introduction **1**
1.1 Terahertz Wave 1
1.2 Motivation and Goal 3
1.3 Outline 4
Bibliography 6

II. Literature Review **7**
2.1 THz Waves for Skin Diagnostic Applications 7
2.2 Structure of Palm Skin 9
2.2.1 Multi-Layered Skin 9
2.2.2 Sweat Duct 11
Bibliography 13

III. Dielectric Property of Palm Skin **17**
3.1 Introduction 17
3.2 Dielectric Properties of Biological Tissues 18
3.2.1 Dielectric Relaxation Model 18
3.2.2 Effective Medium Model 20
3.2.3 Layered Skin Model for Estimating Skin Properties . 22
3.3 Experimental Methods and Devices 24
3.3.1 THz Time Domain Spectroscopy 24
3.3.2 Vector Network Analyzer 25
3.3.3 Optical Coherent Tomography 27
3.4 Morphology of Sweat Gland Ducts and its Spectral Responses 29
3.4.1 Skin Layers 30
3.4.2 Sweat Duct Dimensions 34
3.4.3 Estimation of Operating Frequency of Sweat Gland Ducts 36

3.4.4 Spectral Response of Sweat Gland Ducts using FDTD Simulation . . . 38
3.4.5 FDTD Simulation using Multi-layered Skin Model . 44
3.5 Time Domain Reflectometry for Noise Elimination 47
3.6 Estimation of Dielectric Property of Palm Skin 51
3.6.1 Measurement Protocol 51
3.6.2 Experimental Results 51
3.7 Conclusion 56
Bibliography 57

IV. Spectroscopic Study on Hydration Dynamics of Friction Ridge 61
4.1 Introduction 61
4.2 Effect of Skin Hydration on Friction 63
4.2.1 Perspiration of Palm Skin 63
4.2.2 Friction of Skin in Moist Condition 64
4.3 Experimental Investigation of Skin Hydration and Friction Dynamics 66
4.3.1 Hydration Sensing using Capacitive Sensor 66
4.3.2 Friction Measurement Setup 67
4.3.3 Measurement Procedure 68
4.3.4 Results and Discussion 69
4.4 Resonant Behavior of Friction Ridge Skin 74
4.4.1 Morphology of Friction Ridge 74
4.4.2 Estimation of Spectral Response of Friction Ridge . 75
4.4.3 THz Time Domain Polarimetry 78
4.4.4 Reconstruction of Time Domain Signal 80
4.4.5 Polarization Dependence of Resonance Spectrum . . 82
4.5 Hydration Dynamics of Friction Ridge Skin 85
4.6 Conclusion 89
Bibliography 90

V. Compact THz Source Development: Electron Source 95
5.1 Introduction 95

5.2 Preparation of Graphene-based Films for Field Emitters . . . 99
5.2.1 Film Synthesis . . . 99
5.2.2 Mechanical Shaping . . . 100
5.3 Experimental Results . . . 103
5.4 Conclusion . . . 108
Bibliography . . . 110

VI. Conclusion . . . 115

Appendix . . . 117

Publication List . . . 125

국문초록 . . . 127

List of figures

Figure 1.1. Terahertz band in the electromagnetic spectrum [1]. . 1
Figure 1.2. Research orientation. 3
Figure 2.1. Visible and THz image of excised disease tissue. The solid black line marks the region of diseased tissue. Marked areas d1 and d2, i1 and i2, n1 and n2 are selected as diseased tissue, inflammation and normal tissue, respectively [7]. 8
Figure 2.2. Structure of palm skin (Saferstein, 1995). 10
Figure 2.3. The helix-like shape of the sweat gland ducts obtained by optical coherent tomography [25]. 11
Figure 3.1. Typical frequency response of biological tissues and the corresponding real and imaginary part of the permittivity [5]. 19
Figure 3.2. Polarization mechanisms for relaxations in frequency ranges displayed in Figure 3.1 [5]. 20
Figure 3.3. a) Two layer skin model. ε_1, ε_2 and d_1, d_2 represent dielectric constant and thickness of each layer respectively. b) Algorithm of estimating dielectric constant of 1st layer, stratum corneum in case of palm skin. 23
Figure 3.4. Schematic of THz generation and detection setup using femtosecond laser technology [11]. 24
Figure 3.5. Typical vector network analyzer. 26
Figure 3.6. Schematic of measuring Impedance at Higher Frequencies using vector network analyzer. 26
Figure 3.7. Typical swept source OCT system [13]. 28
Figure 3.8. Typical swept source OCT image of palm skin. White line above the friction ridge is edge of window material. 29

Figure 3.9. Typical OCT image of palm skin. Thickness of stratum corneum in palm skin measured using ImageJ software. 30
Figure 3.10. Reflection of electromagnetic wave in two layered dielectric material. 31
Figure 3.11. A) Reflected time domain signal of THz wave from palm skin obtained with three male subjects. B)THz spectrum of palm skin obtained with three male subjects. 33
Figure 3.12. Morphology of sweat duct in palm skin obtained by optical coherent tomography. 35
Figure 3.13. (a) Measurement sites to obtain sweat duct dimentions. Black dotted circle represent measurement positions. 1 : index finger, 2 : middle finger, 3 : palm (center), 4 : palm (hyphothenor), 5 : palm (thenor) (b) Illustration of morphology of sweat duct. D : diameter of helix, h : height of sweat duct, d : diameter of sweat duct. 35
Figure 3.14. (a) Radiation pattern of normal operation mode of helical antenna. (b) Radiation pattern of axial mode of helical antenna. (c) and (d) show current distribution along helix structure for normal and axial mode respectively. 37
Figure 3.15. Simulation geometry of skin and sweat duct. Discrete port is assigned end of sweat duct to obtain s-parameter. 39
Figure 3.16. Change of S-parameter of sweat duct by electrical conductivity. It shows multiple modes at 100 GHz, 200 GHz, 300 GHz, 350 GHz. 41

Figure 3.17. Radiation modes of sweat duct as transmission antenna. a) Simulation configuration using CST. b) Radiated electric field spectrum. c)-f) Radiation field pattern of sweat duct antenna for 4 distinguished modes shown in spectrum. 42
Figure 3.18. Local field pattern of adjacent to sweat duct. Electric field pattern in radiation condition: a) Normal mode operation at 100 GHz and b) axial mode operation at 350 GHz. Electric field pattern in receiving condition: c) Normal mode operation at 100 GHz and d) axial mode operation at 350 GHz. 43
Figure 3.19. Simulation geometry of two layered skin in CST. . . 45
Figure 3.20. Reflection spectrum of the skin according to the conductivity of the sweat gland and the polarization of the incident wave. 45
Figure 3.21. Diagram of working principle of TDR. 47
Figure 3.22. Diagram of working principle of typical VNA. . . . 48
Figure 3.23. Relation between FFT and IFFT. Frequency resolution Δf has relation with Δt as $\Delta f = 1/N\Delta t$. 48
Figure 3.24. Block diagram of relationship between FFT and IFFT. 49
Figure 3.25. Three series of measurements (air, metal and skin) for calibration and application of TDR to measurement data. 50
Figure 3.26. Schematic of experimental setup. Multiple physiological parameter are measured with reflection of skin simultaneously. a) Blood cuff for blood pressure and pulse rate. b) Thermometer for skin temperature. c) A gypsum frame was used to rest the hand of subject. d) Reflection measurement using open-ended rectangular waveguide probe. white dotted circle indicate temperature sensor attached on skin surface. e) Illustration of measurement. 52

Figure 3.27. a) Time varying physiological parameters. b) Variation of S11 of palm skin during measurement time (15 min). 53
Figure 3.28. Estimated dielectric properties of palm skin. a) Reflection of skin is fitted using two-layer skin with Debye relaxation model. b) Comparison with estimated and literature value [22] of dielectric constant of palm skin. 55
Figure 4.1. Regional variation of sweat glands duct density [10]. Inset shows finger pad in sweating condition. Sweat is secreted along the ridge of fingerprint. 63
Figure 4.2. The bell-curve behavior of the friction coefficient µof human skin as a function of skin hydration. [24]. 65
Figure 4.3. a) Schematic representation of the measuring probe of the capacitance apparatus, Corneometer CM 825. b) Corneometer values shows linear relation with dielectric constant which in linked to hydration level. Date in [25] is reploted. 66
Figure 4.4. Finger friction measurement setup combined with motorized stage. 68
Figure 4.5. Dynamics of hydration level of skin surfaces. The tendency of hydration according to time of fingerprinted skin and fingerprintless skin shows different behavior. Gray dashed line indicates saturation of hydration value of friction ridge skin normalized by its contact area (inset). 70
Figure 4.6. Dynamics of hydration level of skin surfaces of different initial conditions. 71
Figure 4.7. Dynamics of friction coefficient of fingerprint in different initial conditions. 72
Figure 4.8. Relationship between friction coefficient and hydration level for friction ridge skin. 73

Figure 4.9. Morphology of friction ridge obtained by OCT. a) 3D view of finger pad morphology. It is clearly shown that friction ridge has trapezoidal shaped (Inset). b) Top view and c) cut view of finger pad. White solid line shown in a) and c) is window/air or window/ridge interface. Solid red line in b) indicated cut line for cut view. Height and distance between ridges are measure with help of green dot marker in c). Inset of c) shows how to measure height and distance between ridges. 75
Figure 4.10. Diffraction modes of trapezoidal dielectric grating structure. D and h_{eff} represent period and effective height. Due to periodical structure, reflection (0th) and diffraction (nth) modes can be occur. 76
Figure 4.11. a) Simulation geometry. b) Ridge height dependence of resonance frequency. c) Comparison of resonance frequency obtained from simulation and calculation using equation 4.2 respectively. 77
Figure 4.12. Schematic of THz time domain polarimetry. 79
Figure 4.13. a) Raw data of reflected wave on polycarbonate with thickness of 0.5 mm. b) Reshaped signal of a). . . . 81
Figure 4.14. a) Typical waveform of reflected wave on friction ridge skin. b) Reflected wave reconstruction to impulse function. Green solid represents fitting curve to distinguish overlapped waves. Inset shows morphology of measurement position. 82
Figure 4.15. Polarization dependence of reflected signal. Tale part of reflected signal reduced when polarization of incident THz wave become perpendicular to friction ridge. 83

Figure 4.16. Polarization dependence of resonance spectrum. Resonance become week when polarization of incident THz wave become perpendicular to friction ridge. Resonance spectrums are located above the noise level, which confirms validity of data. 84
Figure 4.17. Dynamics of resonance frequency during touch action. 86
Figure 4.18. The correlation graph between normalized RH% and resonance frequency, obtained for 300 sec after touch action. 87
Figure 4.19. FDTD simulation results on the assumption sweat accumulation in valley of friction ridge. Inset shows simulation geometry. *h* indicates moisture accumulation height in valley of fingerprint structure. 88
Figure 5.1. a) Fabricated reduced graphene oxide (rGO) film. b) Sufficiently robust for mechanical handling. 99
Figure 5.2. Uniformity of the rGO-film cut edge using various cutting methods. 100
Figure 5.3. Schematic of the a) rGO film mounting method b) total test setup; c) Experimental setup installed in a vacuum chamber. Inset shows the vertically aligned rGO film between the anode and cathode blocks. . . 102
Figure 5.4. Field emission tendency to be saturated by sequential electrical aging. 103
Figure 5.5. (a) I-V curves of the rGO field emitter before (red) and after (blue) treatment and (b) F-N plot of the rGO field emitter before (red) and after (blue) treatment. 104
Figure 5.6. a) Before electrical conditioning and b) after electrical conditioning. It can be clearly seen that the protrusions are removed after electrical aging, in the beam images. 106
Figure 5.7. Long term field emission stability test in a DC voltage condition. 107

List of tables

Table 1.1. Frequently used units and their conversions at 1 THz. . 2
Table 3.1. Penetration depths of human skin for incident plain wave in THz frequency ranges [8]. 22
Table 3.2. Estimated thickness and minimum frequency by time delay of THz reflection signal 32
Table 3.3. Sectional variation of sweat gland duct dimensions. . . 36
Table 3.4. Skin layer diemsion and permitivity 39
Table 3.5. Sweat duct diemsion and permitivity 40
Table 3.6. Fitted Debye parameter (Equation 3.11) of skin layers . 52

Chapter 1

Introduction

1.1 Terahertz Wave

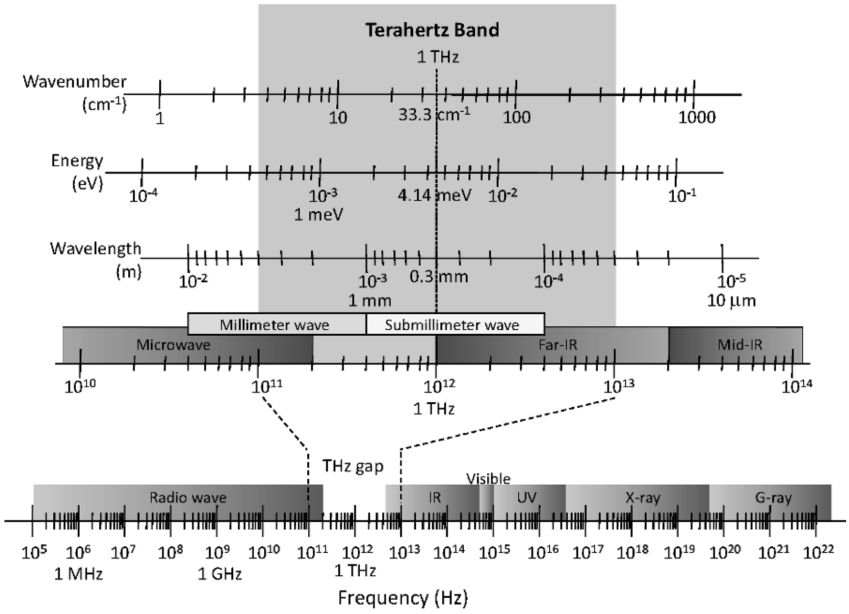

Figure 1.1: Terahertz band in the electromagnetic spectrum [1].

Terahertz (THz) wave is electromagnetic wave whose spectrum is between the microwave and infrared regions. Although through blackbody radiations terahertz wave fills our daily life, this part of the electromagnetic spectrum remains a largely unexplored area due to technical difficulties to develop efficient THz sources and detectors. Due to lack of relative technol-

ogy, the THz frequency region is called the THz-gap. This technological gap has been rapidly filling up over the last decades. Recently, optical technologies has led to the development of broadband THz spectroscopic systems using femtosecond laser, while microwave technology is approaching the THz area from low frequency region. Up to now, THz technology had been independently developed by researchers in various fields such as photonics, electronics and vacuum tubes etc. Therefore, various units are used in different fields for describing THz wave. Frequently used units and their conversions at 1 THz are as shown in Table 1.1.

Table 1.1: Frequently used units and their conversions at 1 THz.

Parameter	Units
Frequency	f = 1 THz = 1000 GHz
Angular frequency	$\omega = 2\pi f$ = 6.28 THz
Period	$\tau = 1/f$ = 1 ps
Wavelength:	$\lambda = c/f$ = 0.3 mm = 300 μm
Wavenumber	$1/\lambda$ = 33.3 cm^{-1}
Photon energy	hf = 4.14 meV
Temperature	$T = hf/k_B$ = 48 K

where c is the speed of light in vacuum, h is Plank constant, and k_B is Boltzmann constant. In physics μm and meV as units of photon wavelength and energy are frequently used. In chemistry, cm^{-1} as a unit of wavenumber and In engineering mm and GHz as units of wavelength and frequency are frequency used, respectively. In general, the THz band refers to 0.1-10 THz. Figure 1.1 illustrates the THz band in the electromagnetic spectrum [1].

1.2 Motivation and Goal

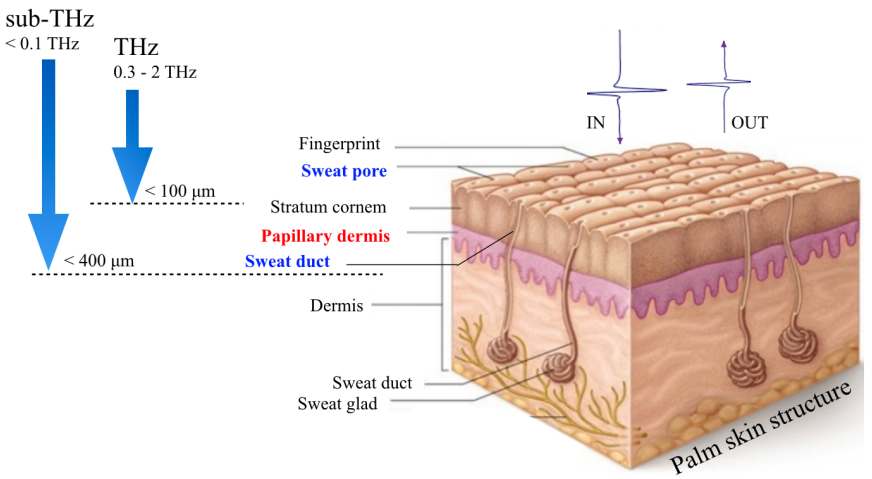

Figure 1.2: Research orientation.

With the recent development of high-resolution optical coherence tomography (OCT), it has become more obvious that skin sub-structures such as multi layered tissues, helical sweat ducts and fingerprints were found to have a size similar to the wavelength of the THz wave (0.1 mm to 1 mm) [2, 3]. THz wave, it refers to an unexplored electromagnetic wave lying in the spectrum between the millimeter wave and the infrared, which has a frequency of 0.3 THz to 3 THz, and is called a dream electromagnetic wave that can be applied to medical, security, communication, etc. [4]. Thus, the goal of this study is to achieve understanding of the spectroscopic characteristics of the human palm skin in sub-THz and THz wave range and to develop novel electron sources for compact high-power THz sources for future applications on skin.

1.3 Outline

This study primarily concentrates on understanding the changes in the dielectric properties of skin due to physiological phenomena, as well as the characteristics of sub-THz and THz waves, mainly due to the structural nature of palm skin.

In chapter 2, previous studies on THz-skin interaction for bio-medical application is presented.

In chapter 3, dielectric properties of palm skin in sub-THz and THz wave is estimated. To do this, it is measured morphology of palm such as thickness of the stratum corneum, the epidermis, the spiral sweat gland duct, and the shape of the fingerprint structure, which are sub-structures of the human palm skin, which could influence spectral responses, using OCT. Dielectric property of each layer of skin was estimated using the Debye dielectric relaxation model in sub-THz and THz frequency regime. Experimental studies to obtain the spectrum of palm skin were performed using vector network analyzer for the sub-THz frequency domain and THz time-domain spectroscopy (THz-TDS) for the THz frequency domain, respectively. The dielectric properties of palm skin have shown to be dispersive by the water contained in the skin. In particular, the increase in blood pressure due to exercise showed that physiological changes in the lower part of the epidermis, including capillaries, affect the permittivity of the epidermal layer.

In chapter 4, spectroscopic study on hydration dynamics of friction ridge (fingeprint) is performed. It was revealed that the ridge structure of the skin surface of the palm is resonance structure in THz frequency range, and

the resonance is modulated by occlusion. Occlusion during touch action was analyzed by monitoring of time-varying THz resonance of the human palm skin. Analysis on dynamics of surface hydration using capacitive sensor and THz resonance with occlusion time can be applied to explain the mechanism by which skin friction is optimally modulated during contact. Experimental evidences have implied that hydration of the valley portion of the friction ridge can affect grip friction.

Development of graphene-based electron sources for compact THz source is presented in chapter 5. The field emission properties of the controlled emission edge of a vertically aligned graphene-based thin film are performed. A current and current density of above 7 mA and 200 A/cm^2, respectively, with uniform electron emission, are achieved. Uniform high current and current density emissions can be realized by the pre-mechanical shaping and post electrical conditioning of reduced graphene oxide (rGO) film emission, owing to the robustness, thinness ($<$1 μm), and well-defined uniform film thickness. Field emission luminance demonstrates uniform emission over the entire emission area with a high aspect ratio. Along with a high current emission, the rGO film exhibits excellent emission stability, long-term. This graphene-based electron beam emitter will accelerate the realization of compact high power THz source applicable to skin as well as existing applications such as field emission.

Bibliography

[1] Y.-S. Lee, *Principles of Terahertz Science and Technology*. Springer, Oct. 2010.

[2] P. Cimalla, J. Walther, M. Mehner, M. Cuevas, and E. Koch, "Simultaneous dual-band optical coherence tomography in the spectral domain for high resolution in vivo imaging," *Optics Express*, vol. 17, no. 22, p. 19486, 2009.

[3] M. J. Adams, S. A. Johnson, P. Lefevre, V. Levesque, V. Hayward, T. Andre, and J. L. Thonnard, "Finger pad friction and its role in grip and touch," *Journal of The Royal Society Interface*, vol. 10, pp. 20120467–20120467, Dec. 2012.

[4] M. Tonouchi, "Cutting-edge terahertz technology," *Nature Photonics*, vol. 1, no. 2, pp. 97–105, 2007.

Chapter 2

Literature Review

2.1 THz Waves for Skin Diagnostic Applications

THz waves are useful to measure water contents in skin because it shows a large contrast in spectrum depending on the presence of water molecules due to electromagnetic wave absorption caused by rearrangement of water molecule [1, 2]. For last decays, huge number of studies have been performed on skin burn assessment [3, 4, 5], diagnosis of blood characteristics, and measurement of blood glucose level [6], medical imaging of skin and breast to distinguish cancer cells from normal cells [7, 8, 9, 10, 11], which have different moisture content.

On the other hand, several studies have been conducted to utilize the THz spectrum of the skin to diagnose a physiological condition of a person. Fabry-perot interference phenomena arising from various layers constituting the skin [12, 12], The antenna resonance of the sweat gland tube is used [13, 14, 15]. The reason why the multi-layer structure of the skin or the antenna structure of the sweat gland tube can determine the skin reflection spectrum of the THz wave is that the thickness of the skin layer and the size of the helical structure of the gland tube are closely related to the wavelength of the THz wave. In this case, strong absorption or scattering occurs at a narrow specific frequency, and the spectrum formed thereby is very distinct,

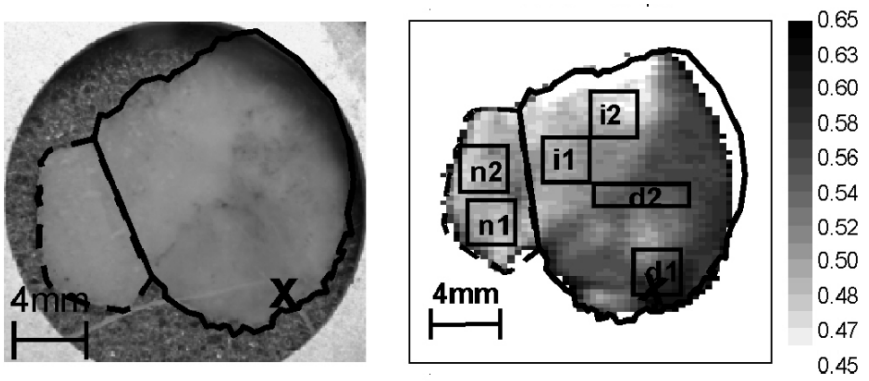

Figure 2.1: Visible and THz image of excised disease tissue. The solid black line marks the region of diseased tissue. Marked areas d1 and d2, i1 and i2, n1 and n2 are selected as diseased tissue, inflammation and normal tissue, respectively [7].

which can be very effectively used for the medical diagnosis of the human body composition and physiological phenomenon [16]. This is because it also spawns or absorbs only a specific frequency range in a narrow region, thus suggesting the potential for non-thermal effects of bio frequency or THz waves of untapped research [17, 18, 19]. However, in order to measure the physiological changes such as moisture using the multi-layered structure of the skin or the resonance of the structures inside the skin such as the glands of the sweat gland, there is a limit to be difficult to distinguish due to the small absorption of the THz waves [12, 20, 21]. If a structure that has an overwhelming influence on the spectrum is found for the purpose of original diagnostic purpose or study of non-thermal effect, it can be very meaningful. Since the size of the fingerprint is a THz wavelength region, It is a good candidate.

2.2 Structure of Palm Skin

The human skin is the largest organ of the human body and constitutes the interface between the body and the environment. The structure of the skin can be classified according to various criteria such as the constituent of the cell, the organ of the cell, and the presence of the blood. The most commonly divided units are largely divided into epidermis and dermis. The epidermis is a layered squamous epithelium that is continuously reproduced keratinized structures, such as nail and stratum corneum. The epidermis occupies a thickness of 0.4-1.5 mm, which is a little less than half of the total skin thickness of 1.5-4 mm. For glabrous skin, such as the palms and feet, the thickness of the stratum corneum is 10 times greater than that of the forearm. When considering the penetration depth of the skin, the multi-layered structure of the skin is a major parameter for determining the reflection spectrum of the skin. This section therefore presents the structure of the palm of the skin from a morphological point of view.

2.2.1 Multi-Layered Skin

The epidermis and the dermis are two distinct layers that largely consist of human skin as shown in Figure 2.2. The epidermis is composed by five layer, that are stratum corneum, stratum lucidum, stratum granulosum, stratum spinsum and stratum basale in order, where the stratum corneum is the outside layer and stratum basale is the innermost layer of the epidermis. The inner stratum basale divides, moves, and becomes the stratum corneum that is dead cells and has no nucleus. Once the cells of stratum basale divide

into new cells, half new-borne cells are transferred to the outer layer, and the other cells stay in the stratum basale for the next division [22]. When the transferred new-borne cells arrive in the stratum spinsum layer, they synthesize keratins, eliminate their nuclear and become dead and dry [23]. The thickness of the stratum corneum is measured to be only 0.06mm to 0.1mm in the most parts of the body. The stratum corneum on the palm and feet soles is the thickest in order to give help to protect more as they have strong relationship with the daily activities unlike other parts of the body.

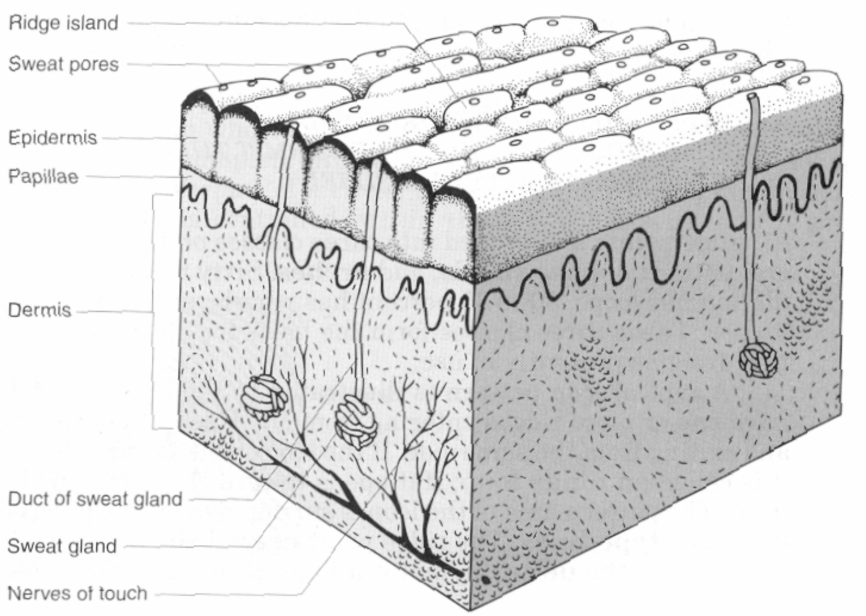

Figure 2.2: Structure of palm skin (Saferstein, 1995).

The dermis is located under the epidermis. It is about 5-7 times thicker than the epidermis, and is composed of two layers; papillary and reticular. The papillary layer has papillae structure and is the interface between dermis and epidermis. This papillae structure builds the pattern of ridges of the

palm and feet soles on the basis. Furthermore, the papillary layer has a lot of connective tissues cells, loose and small of collagen and elastin fibers. In the contrast of papillary layer, the reticular layer has collagens, elastin and the extrafibrillar matrix in high density, that gives support to the skin and provides skin with the extensibility and elasticity [23, 24].

2.2.2 Sweat Duct

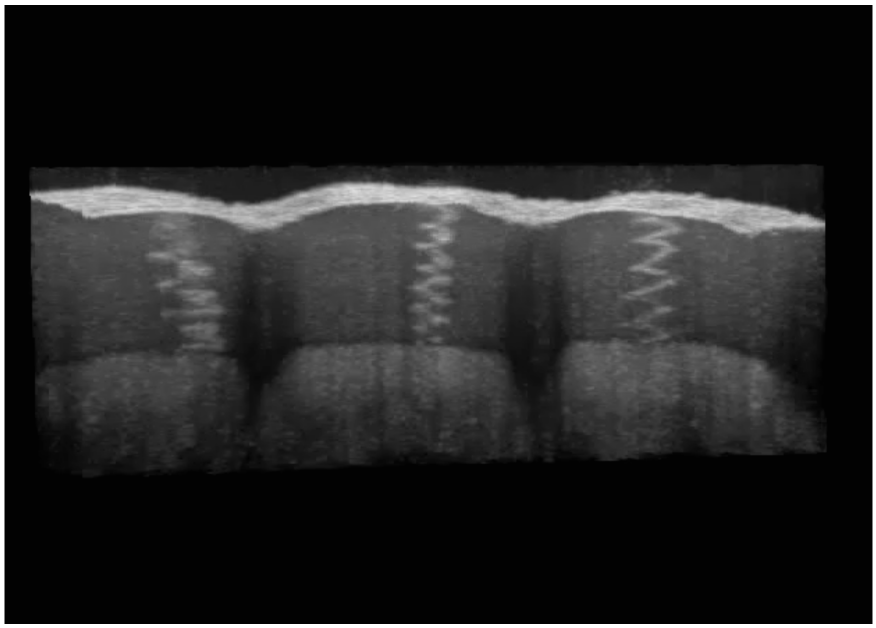

Figure 2.3: The helix-like shape of the sweat gland ducts obtained by optical coherent tomography [25].

Skin has the sweat glands which are located at the lower part of the dermis and are wholely distributed throughout the skin. The main function of the sweat glands is the regulation of body temperature; They also perform adjusting the moisture content in order to maintain the level of hydration of

stratum corneum. There are two kinds of sweat glands; eccrine and apocrine. The eccrine are almost spread of the human body, in particular, are high in density in palms and soles. Apocrine mainly exists in the axilla and perianal areas in human body [22]. Sweat glands are composed of a secretory unit in the shape of coil located in the dermis and a duct that carries the secreted sweat to a pore on the horny layer [26]. The secretory coils are encircled by contractile myoepithelial cells [27]. The autonomic nervous system and the circulating hormones control these myoepithelial cells and they stimulate discharging function of secretion [28]. The duct in the eccrine sweat glands leads from the pore to the stratum corneum, whose end part in the dermis has helical shape which meets the secretory coil. shows a detail of an image of the skin using optical coherent tomography . The end part of the secretory unit situated in the stratum corneum shows clearly in helix-like nature as seen in this image.

Bibliography

[1] S. Fan, Y. He, B. S. Ung, and E. Pickwell-MacPherson, "The growth of biomedical terahertz research," *Journal of Physics D: Applied Physics*, vol. 47, pp. 374009–9, Aug. 2014.

[2] B. C. Q. Truong, H. D. Tuan, A. J. Fitzgerald, V. P. Wallace, and H. T. Nguyen, "A Dielectric Model of Human Breast Tissue in Terahertz Regime," *IEEE Transactions on Biomedical Engineering*, vol. 62, no. 2, pp. 699–707, 2015.

[3] Z. . D. . Taylor, R. S. Singh, M. O. Culjat, J. Y. Suen, W. . S. . Grundfest, H. Lee, and E. . R. . Brown, "Reflective terahertz imaging of porcine skin burns," *Optics Letters*, vol. 33, no. 11, p. 1258, 2008.

[4] P. Tewari, C. P. Kealey, D. B. Bennett, N. Bajwa, K. S. Barnett, R. S. Singh, M. O. Culjat, A. Stojadinovic, W. S. Grundfest, and Z. D. Taylor, "In vivo terahertz imaging of rat skin burns," *Journal of Biomedical Optics*, vol. 17, no. 4, p. 040503, 2012.

[5] Z. D. Taylor, B. Nowroozi, S. Sung, J. Garritano, N. Bajwa, P. Tewari, and W. S. Grundfest, "Exploration of wound physiology using THz imaging," in *2014 39th International Conference on Infrared, Millimeter, and Terahertz waves (IRMMW-THz)*, pp. 1–1, IEEE, 2014.

[6] O. Cherkasova, M. Nazarov, and A. Shkurinov, "Noninvasive blood glucose monitoring in the terahertz frequency range," *Optical and Quantum Electronics*, vol. 48, p. 614, Mar. 2016.

[7] R. M. Woodward, B. E. Cole, V. P. Wallace, R. J. Pye, D. D. Arnone, E. H. Linfield, and M. Pepper, "Terahertz pulse imaging in reflection geometry of human skin cancer and skin tissue," *Physics in Medicine and Biology*, vol. 47, pp. 3853–3863, Oct. 2002.

[8] P. C. Ashworth, E. Pickwell-MacPherson, E. Provenzano, S. E. Pinder, A. D. Purushotham, M. Pepper, and V. P. Wallace, "Terahertz pulsed spectroscopy of freshly excised human breast cancer," *Optics Express*, vol. 17, no. 15, p. 12444, 2009.

[9] C. B. Reid, A. Fitzgerald, G. Reese, R. Goldin, P. Tekkis, P. S. O'Kelly, E. Pickwell-MacPherson, A. P. Gibson, and V. P. Wallace, "Terahertz pulsed imaging of freshly excised human colonic tissues," *Physics in Medicine and Biology*, vol. 56, pp. 4333–4353, June 2011.

[10] A. Balakin, A. Kolesnikov, P. Solyankin, A. Angeluts, M. Nazarov, M. Evdokimov, M. Spencer, A. Nikitin, A. Shkurinov, V. Tuchin, and A. Yaroslavsky, "Terahertz image processing for the skin cancer diagnostic," in *2014 39th International Conference on Infrared, Millimeter, and Terahertz waves (IRMMW-THz)*, pp. 1–1, IEEE, 2014.

[11] A. J. Fitzgerald, E. Pickwell-MacPherson, and V. P. Wallace, "Use of Finite Difference Time Domain Simulations and Debye Theory for Modelling the Terahertz Reflection Response of Normal and Tumour Breast Tissue," *PLOS ONE*, vol. 9, p. e99291, July 2014.

[12] M. Ney and I. Abdulhalim, "Modeling of reflectometric and ellipsometric spectra from the skin in the terahertz and submillimeter waves region," *Journal of Biomedical Optics*, vol. 16, no. 6, p. 067006, 2011.

[13] Y. Feldman, A. Puzenko, P. Ben Ishai, A. Caduff, and A. J. Agranat, "Human Skin as Arrays of Helical Antennas in the Millimeter and Submillimeter Wave Range," *Physical Review Letters*, vol. 100, p. 879, Mar. 2008.

[14] Y. Feldman, A. Puzenko, P. Ben Ishai, A. Caduff, I. Davidovich, F. Sakran, and A. J. Agranat, "The electromagnetic response of human skin in the millimetre and submillimetre wave range," *Physics in Medicine and Biology*, vol. 54, pp. 3341–3363, May 2009.

[15] S. R. Tripathi, E. Miyata, P. B. Ishai, and K. Kawase, "Morphology of human sweat ducts observed by optical coherence tomography and their frequency of resonance in the terahertz frequency region," *Scientific Reports*, vol. 5, p. S266, Mar. 2015.

[16] K. Mizukoshi, K. Yonekura, H. Ogura, Y. Guan, and K. Kawase, "Terahertz wave techniques using a metal mesh for evaluating the components of the stratum corneum," *Skin Research and Technology*, vol. 19, pp. e383–e389, June 2012.

[17] J. Bock, Y. Fukuyo, S. Kang, M. . L. Phipps, L. B. . Alexandrov, K. Ø. . Rasmussen, A. R. . Bishop, E. D. Rosen, J. S. . Martinez, H.-T. Chen, G. Rodriguez, B. S. . Alexandrov, and A. Usheva, "Mammalian Stem Cells Reprogramming in Response to Terahertz Radiation," *PLOS ONE*, vol. 5, p. e15806, Dec. 2010.

[18] L. V. Titova, A. K. Ayesheshim, and A. Golubov, "Intense THz pulses cause H2AX phosphorylation and activate DNA damage response in human skin tissue," *Biomedical optics . . .*, 2013.

[19] B. S. . Alexandrov, M. . L. Phipps, L. B. . Alexandrov, L. G. . Booshehri, A. Erat, J. Zabolotny, C. H. . Mielke, H.-T. Chen, G. Rodriguez, K. Ø. . Rasmussen, J. S. . Martinez, A. R. . Bishop, and A. Usheva, "Specificity and Heterogeneity of Terahertz Radiation Effect on Gene Expression in Mouse Mesenchymal Stem Cells," *Scientific Reports*, vol. 3, p. 910, Jan. 2013.

[20] I. Hayut, A. Puzenko, P. Ben Ishai, A. Polsman, A. J. Agranat, and Y. Feldman, "The Helical Structure of Sweat Ducts: Their Influence on the Electromagnetic Reflection Spectrum of the Skin," *Terahertz Science and Technology, IEEE Transactions on*, vol. 3, no. 2, pp. 207–215, 2013.

[21] I. Hayut, P. Ben Ishai, A. J. Agranat, and Y. Feldman, "Circular polarization induced by the three-dimensional chiral structure of human sweat ducts," *Physical Review E*, vol. 89, p. 042715, Apr. 2014.

[22] I. M. Freedberg, *Dermatology*, vol. 282 of *Fitzpatrick's Dermatology in General Medicine, vols 1-2*. JAMA, Aug. 1999.

[23] L. A. Jones and S. J. Lederman, *Human hand function*. Oxford University Press, 2006.

[24] G. J. Tortora, B. R. Funke, C. L. Case, and T. R. Johnson, *Microbiology: an introduction*, vol. 9. Benjamin Cummings San Francisco, 2004.

[25] P. Cimalla, J. Walther, M. Mehner, M. Cuevas, and E. Koch, "Simultaneous dual-band optical coherence tomography in the spectral domain for high resolution in vivo imaging," *Optics Express*, vol. 17, no. 22, p. 19486, 2009.

[26] W. C. Randall, "Quantitation and regional distribution of sweat glands in man," *Journal of Clinical Investigation*, vol. 25, no. 5, p. 761, 1946.

[27] H. Gray and C. Clemente, "The organs of the senses and the common integument," *Anatomy of the Human Body. Retrieved July*, vol. 1, p. 2002, 1918.

[28] M. Schaller and G. Plewig, “Structure and function of eccrine, apocrine and sebaceous glands,” *Dermatology,*, 2012.

Chapter 3

Dielectric Property of Palm Skin

3.1 Introduction

The human skin layers, the stratum corneum and the epidermis, do not have its own vasculature. Blood is mainly localized in the uppermost dermis-the sub-papillary or upper vascular plexus [1] with typical blood content 20% [2]. The human skin can be considered by major two layers representing non-blood contained stratum corneum with epidermis and blood contained dermis in sub-THz region ($f < 0.2$ THz) because the penetration depth of this frequency region is less than 1 mm, up to the upper dermis region [3]. Therefore, the skin reflection coefficient of the sub-THz waves can be expressed as superposition of the electromagnetic waves reflected from the various layers. In other words, if a proper model is used, the permittivity of skin layers from skin reflection waves can be deduced.

3.2 Dielectric Properties of Biological Tissues

3.2.1 Dielectric Relaxation Model

The interaction of electromagnetic waves with matter is described by Maxwell equations given in Equations 3.1 to 3.4.

$$\nabla \times \mathbf{E} = -\frac{\partial \mathbf{B}}{\partial t} \tag{3.1}$$

$$\nabla \times \mathbf{H} = \mathbf{J} + \frac{\partial \mathbf{D}}{\partial t} \tag{3.2}$$

$$\nabla \cdot \mathbf{D} = \rho \tag{3.3}$$

$$\nabla \cdot \mathbf{B} = 0 \tag{3.4}$$

where **D** and **E** are electric flux density and electric field respectively. **H**, **B** and ρ are magnetic field, magnetic flux density and charge density respectively [4]. Considering only the field near the source with respect to the region containing a small charge or current in space compared with the wavelength λ, it is called quasi-static. At the local site, the field still varies with time, but if the frequency of interest is sufficiently low, it can be considered to change very slowly over time. In other words, since the electromagnetic field changes slowly over time, it can assume electric and magnetic field are similar to field generated by the fixed source, and the time differential term in the Maxwell equations can be ignored. Then **D** can be expressed as Equation 3.5.

$$\mathbf{D} = \varepsilon(\mathbf{E} + \mathbf{P}) = \varepsilon^* \varepsilon_0 \mathbf{E} \tag{3.5}$$

where the polarization **P**, dielectric permittivity ε^* and the dielectric permittivity of vacuum ε_0. If the polarization has relaxation behavior, the time-

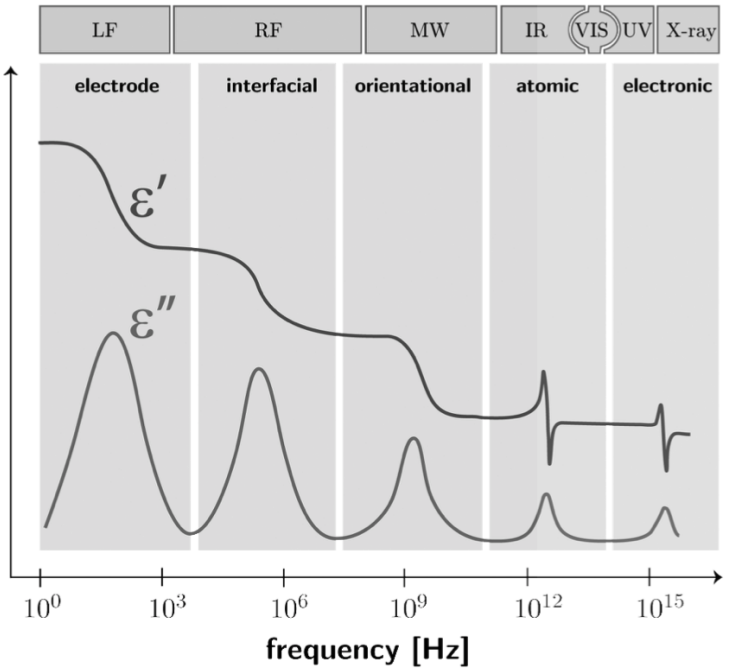

Figure 3.1: Typical frequency response of biological tissues and the corresponding real and imaginary part of the permittivity [5].

dependence of the polarization **P** can be described by given in Equation 3.6.

$$\frac{d\mathbf{P}(t)}{dt} = -\frac{1}{\tau_0}\mathbf{P}(\mathbf{t}) \tag{3.6}$$

The equation has general solution $F(t)$ expressed in Equation 3.7.

$$F(t) = e^{-\frac{t}{\tau_0}} \tag{3.7}$$

After Fourier transformation of Equation 2.18 and the relation in Equation 3.6 one can obtain the frequency-dependent permittivity, known as Debye relaxation formula as given follows:

$$\varepsilon^*(\omega) = \varepsilon_\infty + \frac{\varepsilon_{stat} - \varepsilon_\infty}{1 - i\omega\tau_0} \tag{3.8}$$

Figure 3.1 and 3.2 shows typical dielectric relaxation and mechanism in each frequency range.

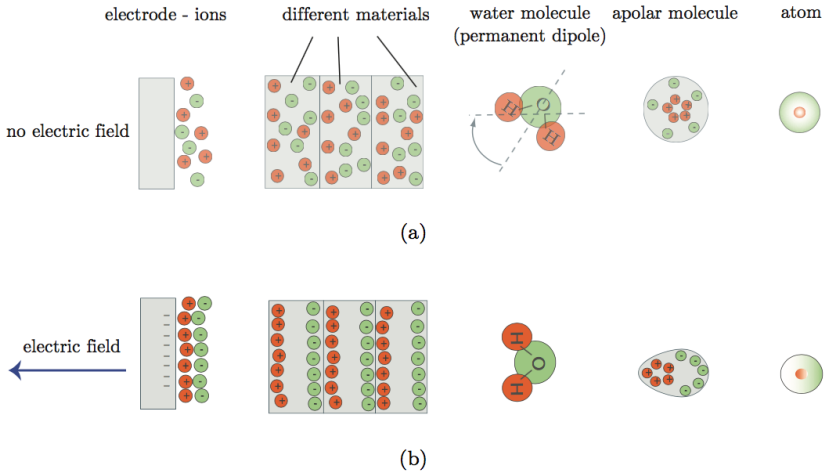

Figure 3.2: Polarization mechanisms for relaxations in frequency ranges displayed in Figure 3.1 [5].

3.2.2 Effective Medium Model

Effective medium theory is used to obtain the dielectric properties of a medium composed of multiple phase materials that are morphologically complex, such as skin and biological tissues, by matching them with a homogeneous bulk material with the same electromagnetic response. As the

simplest model to apply effective medium theory, it can be considered that colloidal particles floating inside a liquid. When colloidal particles, which are the microstructure of these objects, are much smaller than the wavelength of electromagnetic waves oscillating at frequency f, quasi-static regions can be applied and this medium have effective dielectric properties ε_{eff}. In the quasi-static region, the oscillation of the electric field covers in a much larger volume region than the microstructure, microscopically the oscillation is flattened and only the slow change is remained. Thus the averaged fields $\langle \mathbf{D} \rangle$ and $\langle \mathbf{E} \rangle$ are related by the effective permittivity matrix ε_{eff} as in Equation 3.9.

$$\langle \mathbf{D} \rangle = \langle \varepsilon \mathbf{E} \rangle = \varepsilon_{\text{eff}} \langle \mathbf{E} \rangle \tag{3.9}$$

In the situation where spherical particles with a dielectric constant ε_1 are in a medium with a dielectric constant ε_h, the effective response to the electric field of the incident electromagnetic wave can be analytically expressed. The effective permittivity of a material with a volume fraction φ of a material with a dielectric constant of ε_i is given by the Bruggeman formula as follows [6].

$$\varphi_1 \frac{\varepsilon_i - \varepsilon_{\text{eff}}}{\varepsilon_i + 2\varepsilon_{\text{eff}}} = \varphi_h \frac{\varepsilon_h - \varepsilon_{\text{eff}}}{\varepsilon_h + 2\varepsilon_{\text{eff}}} \tag{3.10}$$

with ε_h and ε_i being the volume fractions of host and inclusion, respectively. The Bruggeman formula, for two phases is said to provide excellent agreement with experiments for volume fractions up to '$\varphi < 0.8$ for colloidal suspensions containing homogeneous spherical particles [7]. For binary materials (two phase) for volume fractions up to '$\varphi < 0.8$, the Bruggeman formula is reported to provide excellent agreement with the experimental

results [7]. In the THz frequency region, skin can be regarded as a binary material of protein-water mixture. Size of tissue cell or microorganisms in skin are much smaller than wavelength of THz waves. Therefore, effective medium model could be adopted to estimate skin dielectric properties in this frequency regime. On the other hand, skin sub-structures of a size similar to wavelength of THz wave such as skin multilayer structure and helical sweat gland and fingerprint, the influence of these structures should be considered.

3.2.3 Layered Skin Model for Estimating Skin Properties

In the sub-THz wave, the penetration depth of the skin is about 300 μm (Table 3.1).

Table 3.1: Penetration depths of human skin for incident plain wave in THz frequency ranges [8].

Frequency (GHz)	δ (μm)
0.1	300
1.0	100
1.5	80
2.0	75

Except for thick finger pad or toe, depth of uppermost dermis, which is blood-containing layer, is reachable. Thus, it is not surprising that the skin can be simplified to one layer without blood and another layer with blood. Figure 3.3 a) shows a model in which skin is simply divided into two layers. Each layer has a different permittivity, and the first layer has a finite thickness. The second layer is assumed to be a layer with infinite thickness

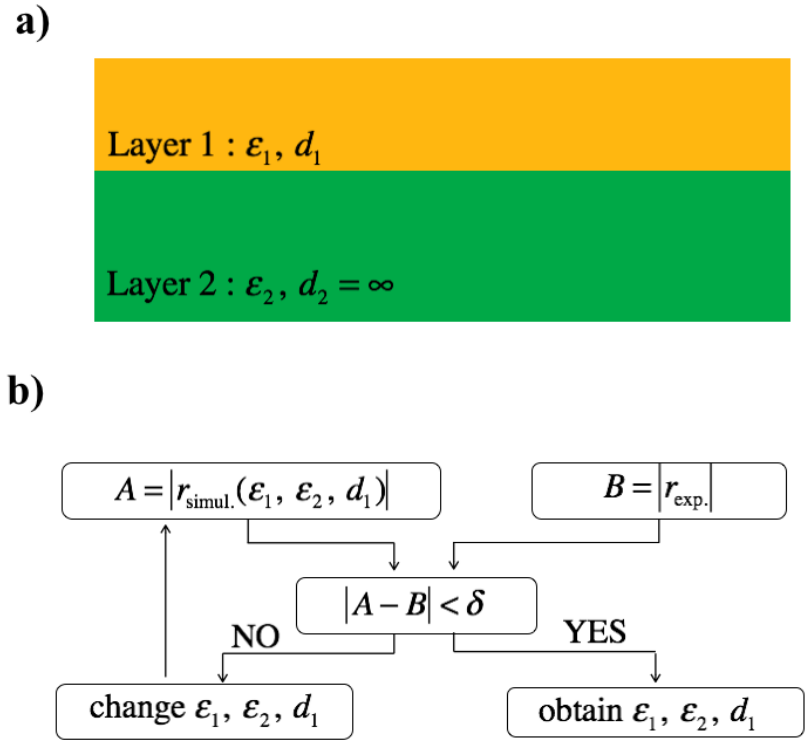

Figure 3.3: a) Two layer skin model. ε_1, ε_2 and d_1, d_2 represent dielectric constant and thickness of each layer respectively. b) Algorithm of estimating dielectric constant of 1st layer, stratum corneum in case of palm skin.

for simplicity of calculation. This is a quite reasonable assumption, since the subcutaneous penetration depth of the sub-THz wave is limited to the upper part of the second layer. Thanks to simple configuration, the reflectance of the skin with the dielectric and thickness of each layer can be numerically calculated. The permittivity of each layer is given by the Debye dielectric relaxation formula of Equation 3.11.

$$\varepsilon_i(\omega) = \varepsilon_{i\infty} + \frac{\Delta\varepsilon_i}{1 + i\omega\tau} + \frac{\sigma_i}{i\omega\varepsilon_0} \tag{3.11}$$

There are three input variables in the Debye relaxation model with conductivity considering the blood contents; ε_∞, $\Delta\varepsilon$ and σ [9, 10]. The input variables are obtained when the difference between the experimentally obtained skin reflectance and the reflectance obtained from the calculation becomes less than a certain value. Figure 3.3 b) shows the algorithm for extracting the permittivity and thickness of each layer by comparing the calculated skin reflectance and the measured skin reflectance.

3.3 Experimental Methods and Devices

3.3.1 THz Time Domain Spectroscopy

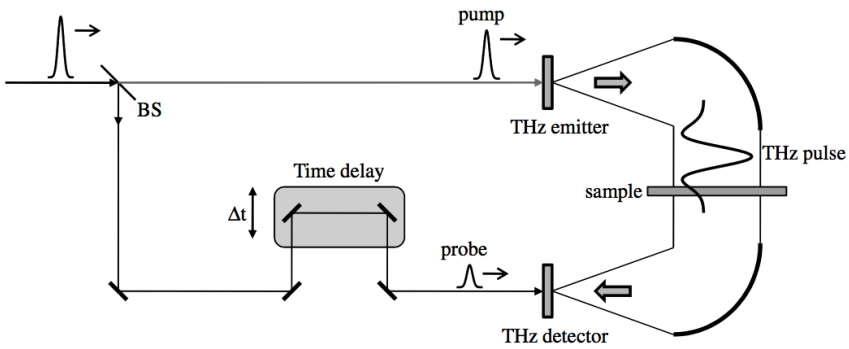

Figure 3.4: Schematic of THz generation and detection setup using femtosecond laser technology [11].

Though there are many kinds of THz devices such as gunn diode devices, vacuum electronic devices, and quantum cascade laser, most suitable for spectroscopy study is THz time domain spectroscopy (THz-TDS) based on non-linear electron excitation on photo-conductive antenna induced by

femtosecond laser pulses [11]. The femtosecond laser is also used to generate and detect THz pulses by irradiating the photoconductive antenna or nonlinear optical crystal. A schematic diagram of a typical setup of THz-TDS is shown in Figure 3.4. The laser is divided into two parts using a beam splitter. One is used to generate the THz pulse and the other is used to detect the THz pulse. This approach is very similar to pump-probe technology. To investigate the THz reflection or transmission characteristics of a sample, the time domain data measured in the presence and absence of the sample are Fourier transformed and divided.

3.3.2 Vector Network Analyzer

Vector network analyzer (VNA) is an important analysis instrument in the field of vacuum devices or communication engineering. It is possible to analyze not only the magnitude of reflected or transmitted power for input signal, but also how much it changes in phase. Figure 3.5 shows the VNA of the typical sub-THz frequency band. The basic principle of VNA measurement is to measure the impedance of a circuit, element, or more generally device under test (DUT) for millimeter or sub-THz waves. Sub-THz electromagnetic waves generated by the VNA stimulate the DUT and receive the response of the DUT. That is, by measuring the phase and amplitude of the signal reflected from the DUT, a variable defined as an S-parameter is measured. The variable we are interested in is the S11 (reflection coefficient). The operation of the schematic VNA is illustrated in Figure 3.6.

Figure 3.5: Typical vector network analyzer.

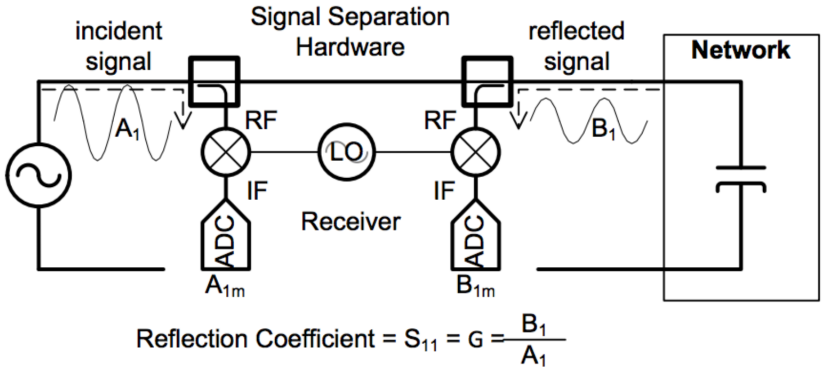

Figure 3.6: Schematic of measuring Impedance at Higher Frequencies using vector network analyzer.

3.3.3 Optical Coherent Tomography

Optical Coherence Tomography (OCT) is a non-invasive imaging technique that analyzes signals from a white light interferometer and provides the internal structure of the biological sample at a high resolution close to the microscope [12]. Based on an interferometer using a white light source, it consists of a light source, a reference stage, a sample stage, and a detection stage. The light splitter divides the white light emitted from the light source into a reference end and a sample end. Light entering the sample stage is condensed by the objective lens and enters the sample, some of which is reflected or scattered back from the sample internal structure.

When the light reflected from the mirror of the reference end is combined with the light from the sample end, optical interference occurs due to the difference in the light path between the two ends. Therefore, if the optical interference signal is extracted, only the signal from the sample located at the same depth as the length of the reference end can be selected. If we want to see samples at different depths, we can simply change the length of the baseline. If the position of the irradiation light is moved also in left and right directions, two-dimensional or three-dimensional tomographic information can be obtained. In general OCT, only the structure information according to the refractive index distribution in the sample is provided because it uses only the intensity of the interference signal. However, studies have been carried out to obtain more information by using not only the intensity of the interference signal but also the phase information. Polarization-sensitive OCT (PSOCT) [14], Doppler OCT (DOCT)[15], and OCT angiog-

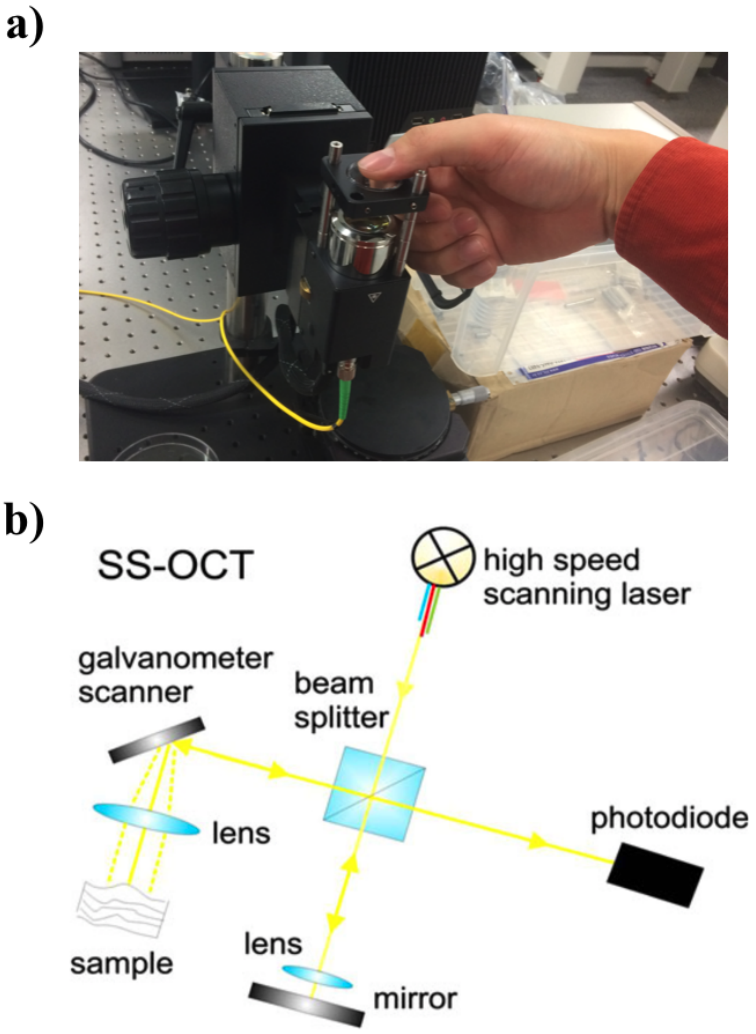

Figure 3.7: Typical swept source OCT system [13].

raphy (OCTA) are examples.

It become important diagnosis tool in dermatology because of capability to show morphology of skin structures. The OCT can provides depth-resolved images of skin tissues with pixel resolution a few micrometers in

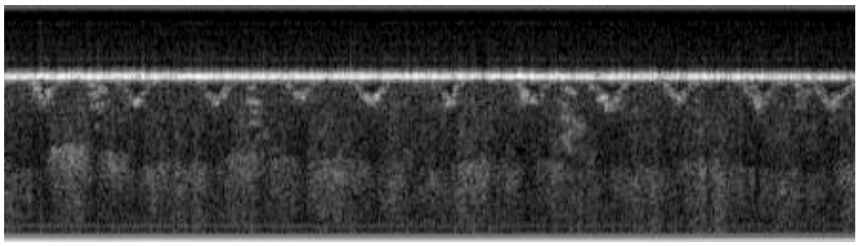

Figure 3.8: Typical swept source OCT image of palm skin. White line above the friction ridge is edge of window material.

case of skin. Many recents studies on evaluating skin structure using OCT have been conducted over the past decade. it have shown that this imaging technique is useful for visualizing sub-structure of human skin, including stratum corneum, epidermis, sweat glands and friction ridge of finger-pad [13]. Here, we use sweep source OCT (Thorlab, MEMS-VESEL SSOCT) to obtain morphology of palm skin and tis substructures.

3.4 Morphology of Sweat Gland Ducts and its Spectral Responses

The multi-layered structure of the skin, the size of the spiral sweat glands, is similar to the wavelength of a THz wave. Therefore, in order to analyze the response characteristics of sub-THz and THz waves of the skin, it is important to measure the shape and size of sub-structure of the human skin. In this section, OCT was used to measure the shape and size of sub-structure of the human skin and implement this information in simulation code to estimate the sub-THz and THz wave characteristics of the human skin.

3.4.1 Skin Layers

OCT was used to measure skin structures. Figure 3.9 shows a typical OCT image of the palm skin. The skin is clearly composed with layers as stratum corneum with spiral sweat glands and epidermis with dermis. Thickness of stratum corneum varies with measurement position. The human skin can be considered by major two layers representing non-blood contained stratum corneum with epidermis and blood contained dermis in sub-THz region because the penetration depth of this frequency region is less than 1 mm, up to the upper dermis region [3]. The palm skin was simplified to two-layer dielectric model and effect of multilayer structure of the skin on the reflection spectrum was analyzed. The reflection of the electromagnetic wave incident on simplified skin model can be modeled as shown in Figure 3.10. When an electromagnetic wave is incident from a medium having a dielectric constant of ε_1 into a medium having two layers having dielectric constant ε_2 with thickness d and dielectric constant ε_3 with infinite

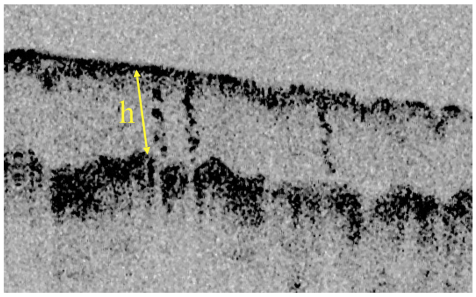

Position	Thickness h (um)
index finger	520
middle finger	520
palm (center)	400
palm (hypothenor)	350
palm (thenor)	250

Figure 3.9: Typical OCT image of palm skin. Thickness of stratum corneum in palm skin measured using ImageJ software.

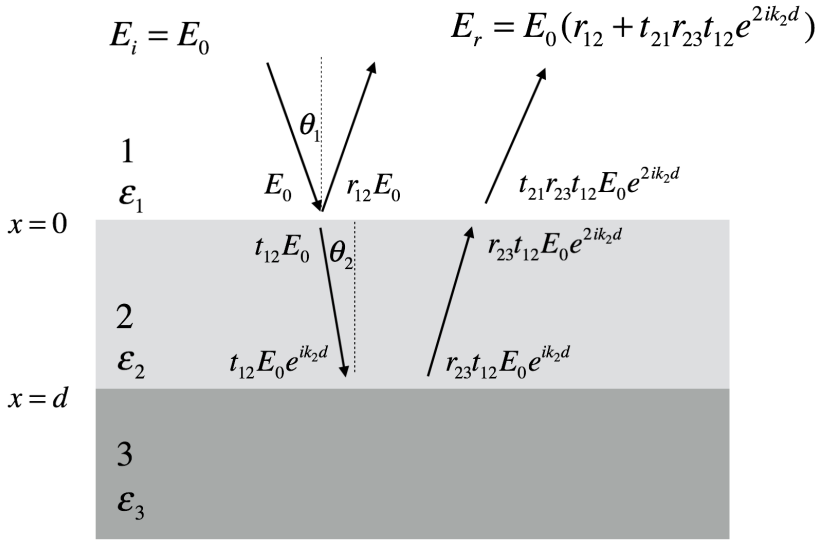

Figure 3.10: Reflection of electromagnetic wave in two layered dielectric material.

thickness, the reflected electric field can be expressed as Equation 3.12.

$$E_r = E_0(r_{12} + t_{21}r_{23}t_{12}e^{2ik_2d}) \tag{3.12}$$

where E_0 is electric field intensity of incident wave, t_{ij} is transmission coefficient when incident from medium i to medium j (Equation 3.13), r_{ij} is reflection coefficient when incident from medium i to medium j (Equation 3.14) and k_i is wavenumber in medium i (Equation 3.15).

$$t_{lm} = \frac{2\sqrt{\varepsilon_m}}{\sqrt{\varepsilon_l} + \sqrt{\varepsilon_m}} = |t_{lm}|\, e^{i\psi_{lm}} \tag{3.13}$$

$$r_{lm} = \frac{\sqrt{\varepsilon_l} - \sqrt{\varepsilon_m}}{\sqrt{\varepsilon_l} + \sqrt{\varepsilon_m}} = |r_{lm}|\, e^{i\phi_{lm}} \tag{3.14}$$

$$k_l = 2\pi c / f \mathrm{Re}\left(\sqrt{\varepsilon_l}\right) \tag{3.15}$$

The electromagnetic wave incident from the medium i in the medium j has a phase change of ψ_{ij} or ϕ_{ij} when it transmitted or reflected at the interface respectively. Thus the reflected electric field can be expressed as Equation 3.16.

$$E_r = E_0 |r_{12}| e^{i\phi_{12}} + E_0 |t_{21}| |r_{23}| |t_{12}| e^{i(2k_2 d\cos(\theta_2)+\psi_{21}+\phi_{23}+\psi_{12})} \tag{3.16}$$

The reflected electromagnetic waves are represented by the superposition of the two reflected waves reflected as shown in Equation 3.16. When two reflected waves interfere in destructive manner, resonance occurs on the spectrum. In other words, Fabry-Perot resonance is predicted by multiple layers of skin. In order to cause destructive interference, the phase components of the two waves must differ by π. The frequency at which resonance is predicted using this condition is calculated as follows.

$$f = c\frac{m + 0.5 + (\psi_{21} + \phi_{23} + \psi_{12} - \phi_{12})/2\pi}{2\mathrm{Re}\left(\sqrt{\varepsilon_2}\right) d\cos(\theta_2)} \tag{3.17}$$

Table 3.2: Estimated thickness and minimum frequency by time delay of THz reflection signal

Subject	τ_{delay} (ps)	f_{min} (GHz)	$d_{\mathrm{estm.}}$ (μm)	$f_{\mathrm{res.}}$ (GHz)
1	2.9	164.7	280.8	172.4
2	3.45	135.4	334	144.9
3	3.9	124.4	377.6	128.2

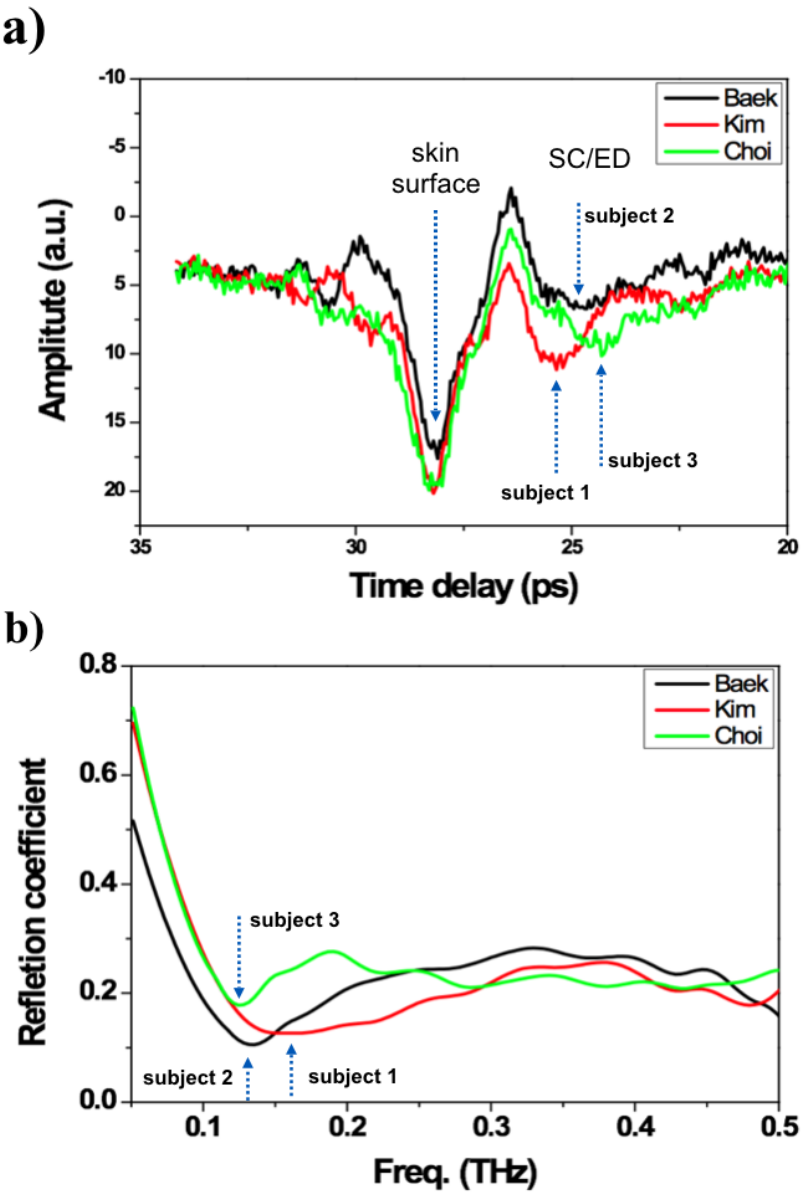

Figure 3.11: A) Reflected time domain signal of THz wave from palm skin obtained with three male subjects. B)THz spectrum of palm skin obtained with three male subjects.

When the reflection waveform of the palm skin is confirmed using THz-TDS, it can be confirmed that there are mainly two reflected waves. The time difference between the two waves (τ_{delay}) can be obtained from the reflected waveform measured on the hypothenor of 3 healthy male (ages 23-30) (Figure 3.11). Assuming that the dielectric constant ε of the stratum corneum is 2.2, the thickness ($d_{estm.}$) and resonance frequency ($f_{res.}$) of the stratum corneum can be calculated from the time difference (Table 3.2).

3.4.2 Sweat Duct Dimensions

Despite the fact that it is known that sweat glands are in the form of spirals [16], most textbooks describe them in a straight line instead of a spiral [17]. OCT was used to measure the shape and dimensions of the spiral glands. As shown in Figure 3.12, sweat glands were observed in the stratum corneum inside the palm of skin. The pixel resolution of the OCT using the 1300 nm wavelength is about 5 μ m, which is sufficient to measure the shape and dimension of the glands. The measurement site is the center of the palm, stop, index finger, as shown in Figure 3.13 a). To record the spiral shape of the gland tube, the diameter D of the helix, the diameter d of the duct, the height h of the helix, and the number of turn are measured for each site as shown in Figure 3.13 b) and can be seen in Table 3.3.

The obtained data was implemented in simulation code and used to determine the effect of spiral glands on the spectral reflectance of sub-THz waves. The height of the spiral glands was the largest in the fingers, so the turn was the largest in the fingers too. This is thought to be proportional to the thickness of the stratum corneum. The helix diameter D and the duct

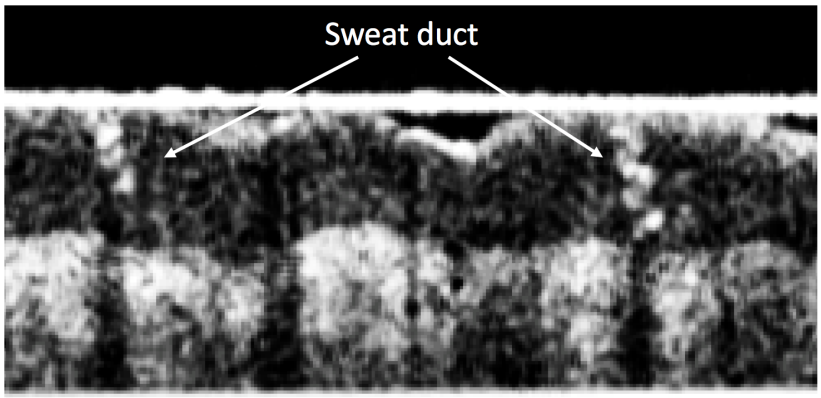

Figure 3.12: Morphology of sweat duct in palm skin obtained by optical coherent tomography.

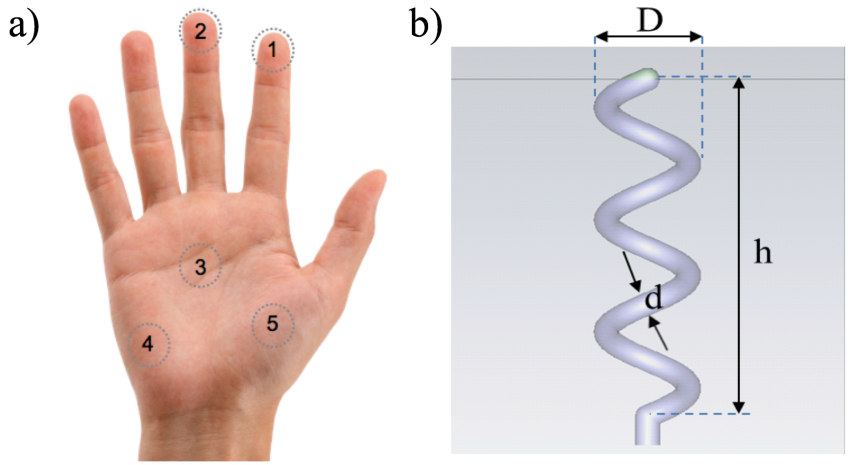

Figure 3.13: (a) Measurement sites to obtain sweat duct dimentions. Black dotted circle represent measurement positions. 1 : index finger, 2 : middle finger, 3 : palm (center), 4 : palm (hyphothenor), 5 : palm (thenor) (b) Illustration of morphology of sweat duct. D : diameter of helix, h : height of sweat duct, d : diameter of sweat duct.

diameter *d* of the sweat gland spiral were found to have a constant value even though various sites were measured. The constant dimension of the

Table 3.3: Sectional variation of sweat gland duct dimensions.

Section	h (μm)	D (μm)	d (μm)	N
1. index finger	520	80-100	30	4-6
2. middle finger	520	80-90	30	4-5
3. palm (center)	400	60-80	30	3-5
4. palm (hypothenor)	320-370	80-100	30	4-5
5. palm (thenor)	250	70-140	20-40	3

gland tube means that it has a constant operating frequency irrespective of the region of the skin, assuming it is a helical antenna as shown in [18]. The interaction between the operating frequency and the electromagnetic wave when the gland tube is assumed to be an antenna is discussed in detail in the following section 3.4.2 and 3.4.3. Therefore, we used $D = 80\mu m$ and $d = 26\mu m$ for the simulation code.

3.4.3 Estimation of Operating Frequency of Sweat Gland Ducts

Sweat glands might function as helical antennas, the operating frequency of which is dependent on the structural parameters of the helical ducts: height L, diameter D and number of turns of the helix N. This parameter allows you to calculate other parameters such as circumference, pitch angle, and overall length. According to electromagnetic theory, a helical antenna operates in two modes. First, there is 'normal' in which the radial direction is perpendicular to the axial direction of the helix (Figure 3.14 a), and secondly, there is an 'axial mode' in which the radial direction is the same as the axial direction of the helix (Figure 3.14 b). Each mode operates at a

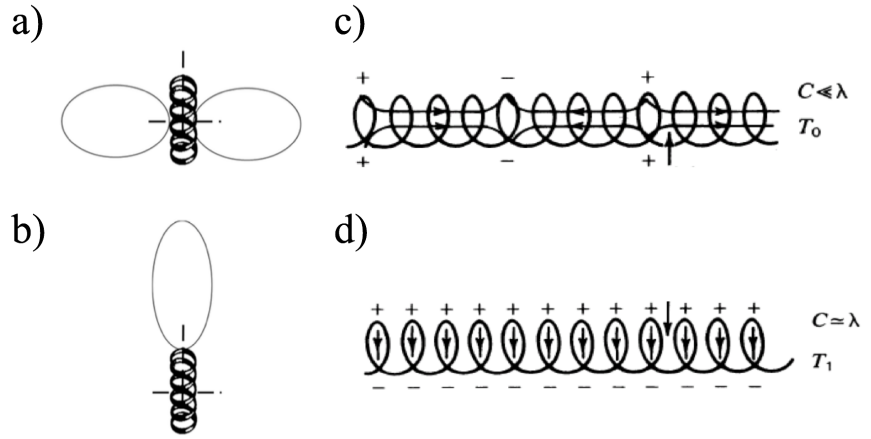

Figure 3.14: (a) Radiation pattern of normal operation mode of helical antenna. (b) Radiation pattern of axial mode of helical antenna. (c) and (d) show current distribution along helix structure for normal and axial mode respectively.

different frequency because the supported frequencies are different depending on the current distribution inside the antenna. In the normal mode, the current distribution has the characteristic that the polarity crosses along the axial direction of the antenna (Figure 3.14 c). Has a frequency determined by the length (h) of the antenna rather than the structure of the helix of the antenna. The normal mode frequency is determined by the Equation 3.18.

$$f = \frac{c}{n}\frac{2S}{\pi^2 D^2} \tag{3.18}$$

$$f = \frac{c}{\pi D n} \tag{3.19}$$

Therefore, the helical antenna is driven to normal when the circumstance of the helix is smaller than the operating frequency wavelength. In axial mode, the current distribution has the characteristic that the polarity of the current is repeatedly crossed according to the internal structure of the helix (Figure 3.14 d). Therefore, it has a frequency determined by the circumstance of the helix structure. The frequency of the axial mode is determined by the Equation 3.19.

3.4.4 Spectral Response of Sweat Gland Ducts using FDTD Simulation

FDTD simulation was performed using the CST Microwave Studio program to check antenna characteristics of spiral glands [19]. In the simulation, the unit of length was set to 'μm', frequency was set to 0 - 500 GHz and background was set to 'normal'. The boundary condition was set to 'periodic'. Figure 3.15 shows the simulation geometry with simulated glands. The size of the unit cell containing the gland tube was set to a = 450 μm on one side. This is a value corresponding to 500 duct/cm^2 density of sweat glands in palm skin [20]. The sweat glands were assigned in the middle of unit cell inside the stratum corneum with thickness t1 = 420 μm (Figure 3.15). The geometry of the glands was measured using OCT Table xx. The thickness and permittivity of each skin layer set in the simulations are given in Table 3.4. The geometry of the glands measured using OCT was assigned as shown in Table 3.5. Conductivity of the glandular tube was set from 3.5×10^2 S/m as shown in the reference to the perfect electric conduc-

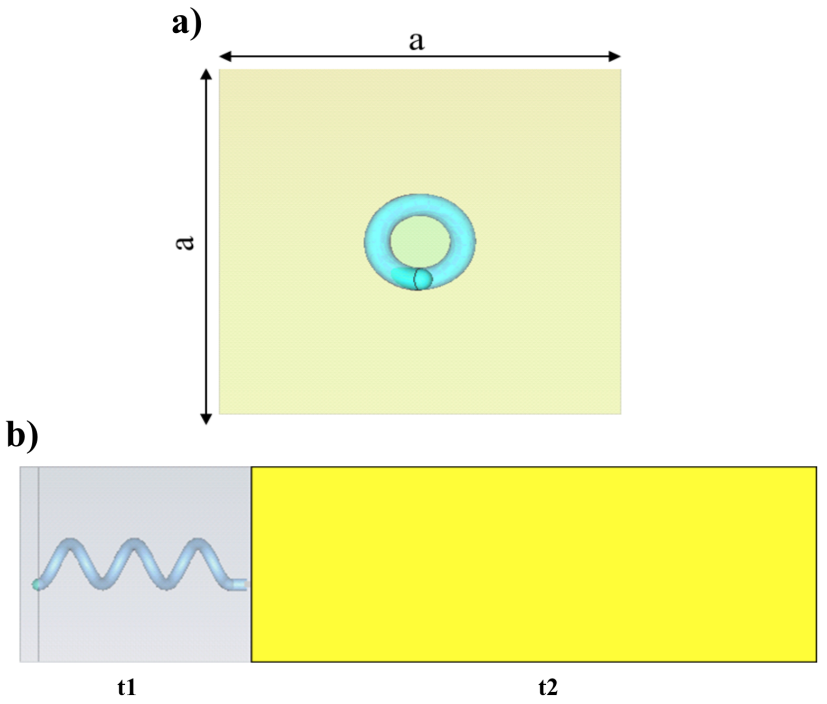

Figure 3.15: Simulation geometry of skin and sweat duct. Discrete port is assigned end of sweat duct to obtain s-parameter.

tor conductivity of 1.0×10^6 S/m.

Table 3.4: Skin layer diemsion and permitivity

Layer	Dimension (μm)	Permittivity	conductivity (S/m)
Stratum corneum	$t1 = 420$	3.2	1
Epidermis + Dermis	$t2 = 1000$	3.6	30

The pH of the skin surface is about 5, while the pH of the dermal layer where sweat gland tube coils are located is about 7. This difference in pH is sufficient to generate current through the 'proton transfer' mechanism, which is a rapid transfer mechanism of the hydrogen ions contained in the

Table 3.5: Sweat duct diemsion and permitivity

Section	Dimension (μm)	Permittivity	conductivity
Helix diameter	$D = 80$		3.5×10^2
Height	$h = 350$	4	to
Duct diameter	$d = 24$		1×10^6

sweat [9]. As a result, the sweat glands can have a higher electrical conductivity than other parts of the skin, which can lead to antenna characteristics.

In order to evaluate the characteristics of the sweat glands as a antenna, a 'discrete port' was set near the boundary between the stratum corneum and the epidermal layer where the sweat glands started, and input current was assigned. By analyzing the reflected signal of inserted current, it is possible to evaluate which frequency forms and radiates through sweat glands antenna.

The S11 parameters of the discrete port in the given frequency band were monitored with varying conductivity of the sweat duct from 3.5×10^2 to 1.0×10^6 S/m. Figure 3.16 shows the S-parameter in 0 - 500 GHz range of sweat duct antenna according to the change in its conductivity. When the electric conductivity is less than 1.0×10^4 S/m, no resonant behavior is shown in the S-parameter graph. It is confirmed that when the conductivity is higher than that, the antenna characteristic appears. The sweat duct antenna has four modes within a given frequency range. According to Equation 3.18 and Equation 3.19, the mode of the 100 GHz region is assumed to be the normal mode, and the mode of the 300 GHz region is assumed to be the axial mode.

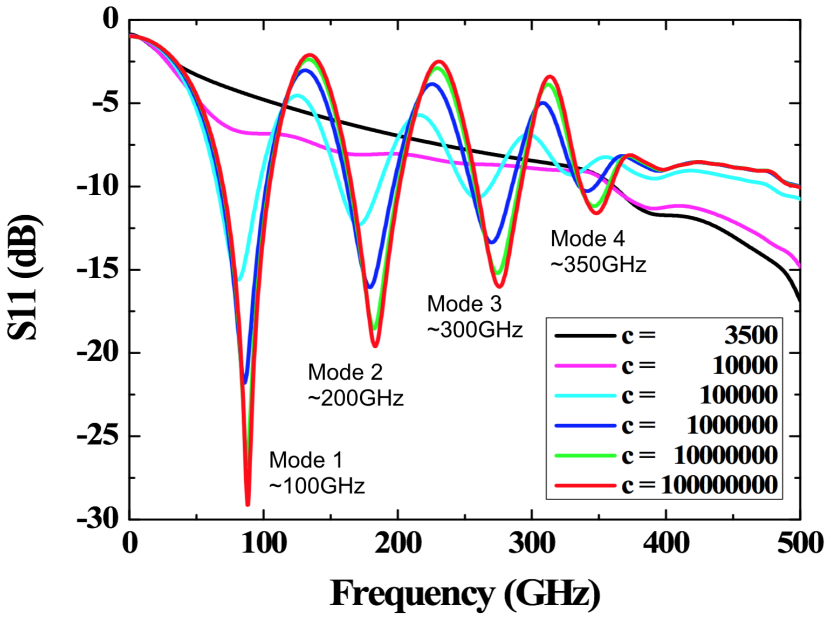

Figure 3.16: Change of S-parameter of sweat duct by electrical conductivity. It shows multiple modes at 100 GHz, 200 GHz, 300 GHz, 350 GHz.

To confirm the radiation characteristics of the sweat duct antenna, a simulation was performed with a field monitor located at a distance of about 2 mm normal to the skin. Figure 3.17 a) shows the configuration of the simulation. It is shown that the radiation frequency also had four different modes, as confirmed in the current input characteristic simulation of the sweat duct. Among them, the mode near 350 GHz has the highest radiation power in the direction perpendicular to the skin (Figure 3.17 b). At frequencies above 300 GHz, the operating sweat duct antenna radiates in the axial direction, which can be seen in the radiation pattern of each mode. Figure 3.17 c) - f) show the radiation pattern of each mode of the sweat duct antenna. The mode cor-

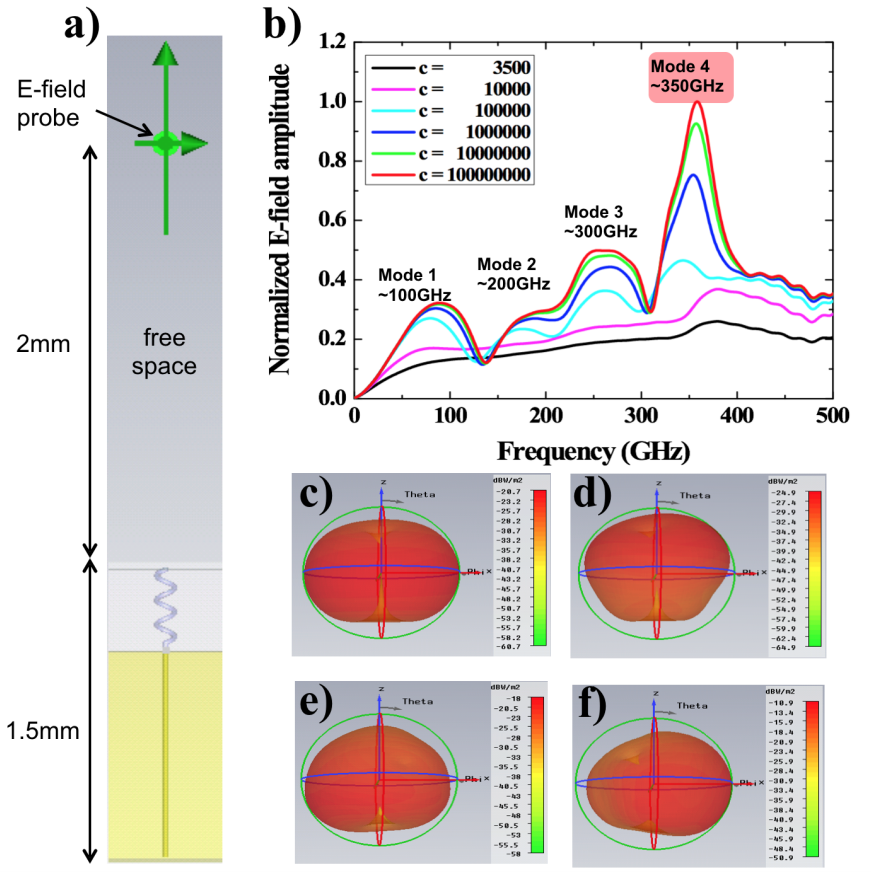

Figure 3.17: Radiation modes of sweat duct as transmission antenna. a) Simulation configuration using CST. b) Radiated electric field spectrum. c)-f) Radiation field pattern of sweat duct antenna for 4 distinguished modes shown in spectrum.

responding to Figure 3.17 f) has the highest output radiation component in the direction normal to the skin (axial mode). It is necessary to examine how the sweat duct reacts to the electromagnetic waves coming from outside the skin before confirming the reflection characteristics of the skin due to the sweat duct antenna. Figures 3.18 a) and c) show the local field ad-

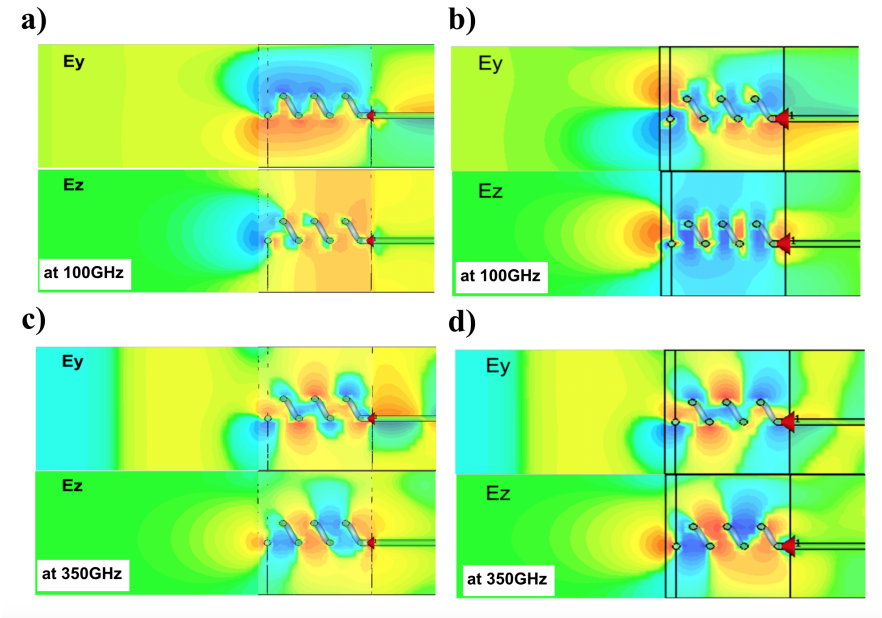

Figure 3.18: Local field pattern of adjacent to sweat duct. Electric field pattern in radiation condition: a) Normal mode operation at 100 GHz and b) axial mode operation at 350 GHz. Electric field pattern in receiving condition: c) Normal mode operation at 100 GHz and d) axial mode operation at 350 GHz.

jacent the sweat duct antenna when the sweat duct radiates. The local field at 100 GHz has a similar field distribution with the current distribution of normal mode as shown in Figure 3.14 c) and the local field at 350 GHz shows the field distribution in axial mode as shown in Figure 3.14 d). On the other hand, Figures 3.18 b) and d) show the local field distribution of the sweat duct due to the electromagnetic wave incident from outside the skin. Since the transmitting mode and the receiving mode show the same field distribution, it can be checked whether the antenna works as a receiving antenna in the corresponding mode by checking the field distribution excited

by the normal incident wave. In the normal mode, the local field distribution excited by incident wave is different from the field distribution when it transmitting (compare Figures 3.18 a) and c)). Normal mode radiates electromagnetic waves in a direction perpendicular to the helix axis direction. In order to excite the normal mode by incident wave, incident wave must have electric field component parallel to axis of helix. Therefore, electromagnetic waves incident on the skin are hard to excite the normal mode of the glandular tube antenna. Hence the influence of the sweat duct antenna could be neglected when considering the reflection characteristics of the skin. On the other hand, the field distribution near the sweat duct by the 350 GHz incident wave is very similar to the filed distribution when it radiate in axial mode. Considering the reflection characteristics of the skin, around 300 GHz, the sweat duct may act as an antenna and affect the reflection spectrum of skin. In spite of this discussion, it is difficult to say that the sweat duct acts as an antenna, even though the axial mode field distribution similar to excited field distribution. First, conductivity of swat duct should be huge in order to act as antenna. Second, radiation pattern as shown in Figure 3.17 f) shows pure radiation directivity to axial direction. In fact, the axial mode radiation pattern of a well designed helical antenna has more than 10 turns N to obtain high directivity, whereas $N < 5$ for sweat duct and embedded in lossy material, human skin.

3.4.5 FDTD Simulation using Multi-layered Skin Model

FDTD simulation was performed with two layer skin model using the CST Microwave Studio as like sweat duct simulation. In simulation, all the

unit of length, frequency range, background, boundary conditions and size of unit cell was set as described in Section 3.4.4. In simulation configura-

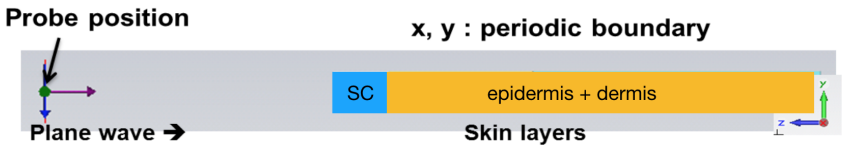

Figure 3.19: Simulation geometry of two layered skin in CST.

tion, plane wave is incident normal to skin surface and skin are assigned by two layer stratum corneum (SC) and epidermis (with dermis) as shown in Figure 3.19. The sweat glands were assigned in the middle of unit cell inside the stratum corneum (Figure 3.15).

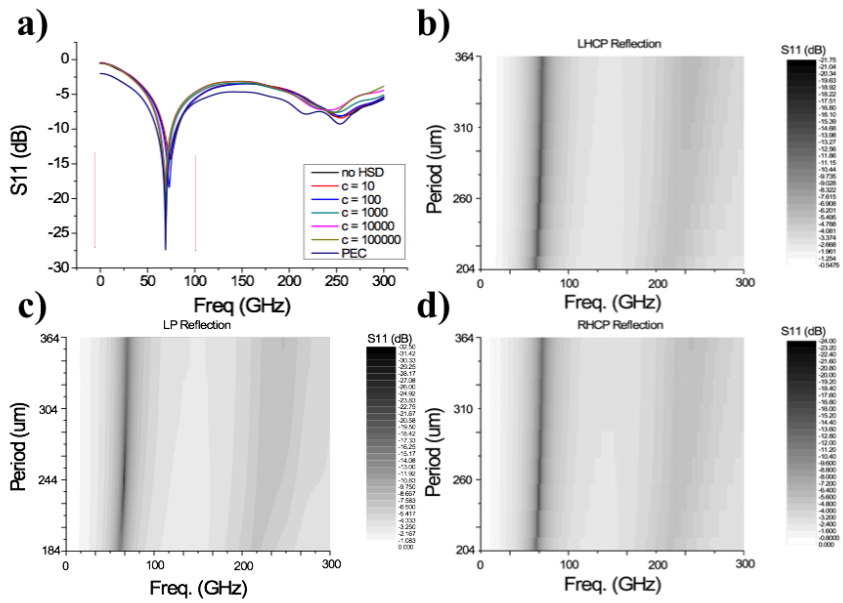

Figure 3.20: Reflection spectrum of the skin according to the conductivity of the sweat gland and the polarization of the incident wave.

In order to monitor the reflected wave, incident plane wave perpendicular to the skin was assigned. A E-field probe was assigned at 1 mm distance normal to the skin. In order to evaluate the effect of spiral sweat glands as well as multilayer reflection of the skin, the conductivity of the sweat glands was changed. The reflection spectrum of the skin was simulated by changing the polarization type of the incident wave into linear polarization, left polarization and right polarization to examine effect of helical sweat duct. Figure 3.20 shows the reflection spectrum of the skin according to the conductivity of the sweat gland and the polarization of the incident wave. Though there is minor change in the reflection spectrum according to the conductivity of the glands, though high conductivity was applied as 1.0×10^5 S/m or more. Fabry-Perot resonance due to multi-layer reflection of the skin is observed at around 80 GHz. From this simulation results, the multi-layered structure of the skin mainly determines the reflection spectrum of the skin, and the effect of the sweat glands duct on the reflection spectrum of the skin is secondary. Since the sweat gland duct has a spiral shape, the antenna characteristics of the sweat duct can be evaluated more finely by comparing with the case where the circularly polarized electromagnetic wave incidence to the skin with proper direction of circular polarization. Figure 3.20 b) to d) show the reflection spectrum of the skin according to the polarization of incident wave. Regardless of polarizations, and regardless of the distance between sweat duct assigned in the skin, the skin reflectance spectrum has a strong resonance around 80 GHz (Fabry-Perot interference by multi-layered skin). Results of simulations imply that the effect of the sweat duct on the reflection spectrum of the skin as an antenna is minimal and spectral re-

sponse of skin in sub-THz wave can be analyze by multi-reflection from skin layers.

3.5 Time Domain Reflectometry for Noise Elimination

Time Domain Reflectometry (TDR) is one of the important functions of a digital sampling oscilloscope or VNA. This can be used to measure the time response of a circuit or system, which is very useful in removing the disturbing noise signal when trying to view the original response of a system or circuit [21]. VNA is a representative equipment with TDR function as an option. This section describes principle TDR and how to realize in Matlab code for eliminating noise to obtain valid reflected signal of palm skin. The basic diagram of the TDR instrument is shown in Figure 3.21.

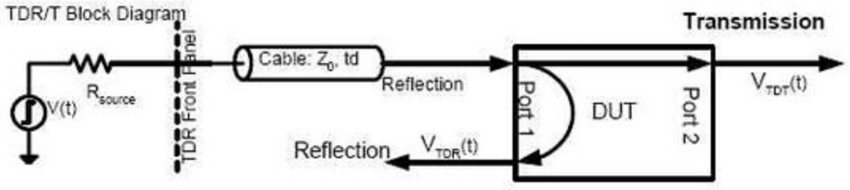

Figure 3.21: Diagram of working principle of TDR.

A remarkable fact is that the above diagram is similar to working diagram of VNA in Figure 3.22. Due to this similarity, it is possible to analyze the data measured VNA data using the TDR function to eliminate noise or to analyze reflection surfaces. The only difference between these two is that the TDR analyzes the signal in the time domain and the S-parameter

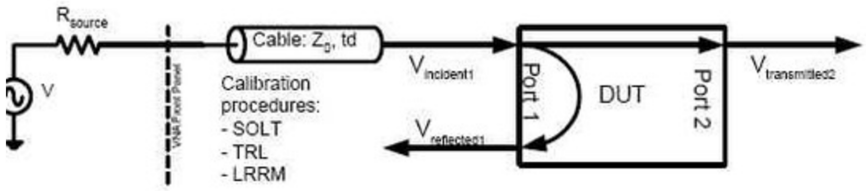

Figure 3.22: Diagram of working principle of typical VNA.

measured in the VNA is in the frequency domain. Therefore, it is possible to convert between two data using Fast Fourier Transform (FFT) and Inverse Fast Fourier Transform (IFFT). As the number of points of data in the time

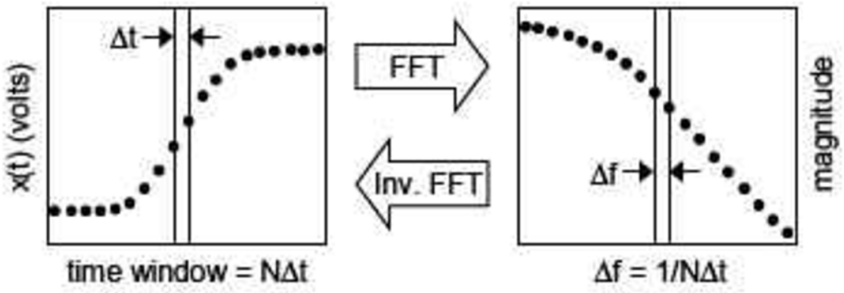

Figure 3.23: Relation between FFT and IFFT. Frequency resolution Δf has relation with Δt as $\Delta f = 1/N\Delta t$.

domain increases, the resolution of the frequency domain is improved. On the other hand, as the number of frequency domain data points increases, the resolution of the time domain is improved. The detailed relationship between resolution and data points is shown (Figure 3.23).

The TDR function can be implemented from the basic theory of FFT and IFFT. General relationship between time domain and frequency domain is as shown in Figure 3.24. When there is a system called $h(t)$ in time do-

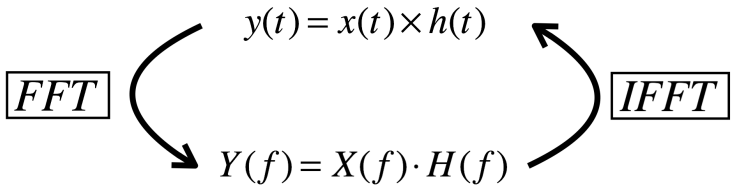

Figure 3.24: Block diagram of relationship between FFT and IFFT.

main, if the input $x(t)$ is applied, the output $y(t)$ can be found by the convolution of $x(t)$ and $h(t)$. However, if we convert it to the frequency domain, output $Y(f)$ can be represented the by simply multiplying two functions $X(f)$ and $H(f)$. Here, $H(f)$ can be regarded as S-parameter of VNA as follows.

$$H(f) = S_{11} \tag{3.20}$$

Then TDR is expressed as:

$$IFFT(FFT(V_{source}(t) \cdot S_{11}) = IFFT(V_{source}(f) \cdot S_{11}) = \rho_{S_{11}} \tag{3.21}$$

Here are more things to consider: when deriving the sampling frequency, f_s, from the source's sampling time, t_s, it should be more than twice the Nyquist frequency, $f_{\max}$.

$$f_s = \frac{1}{t_s} \geq f_{\max} \tag{3.22}$$

If the upper limit of the frequency to be analyzed is 110 GHz, the sampling frequency should be more than 220 GHz. As a result, the sampling time must be less than $1/(110\text{GHz}) = 25\text{ps}$ ps in order to satisfy the sampling frequency condition (Equation 3.22). Finally, analysis frequency is defined

as follows.

$$f_{\text{anal}} = \frac{f_{\text{end}}}{N} \tag{3.23}$$

where $N = t_{\text{end}}/t_{\text{s}}$ is sampling number and t_{end} is total time. If the analysis frequency matches the upper limit of S-parameter measurement band, TDR can be realized using FFT and IFFT. Figure 3.25 shows an example of

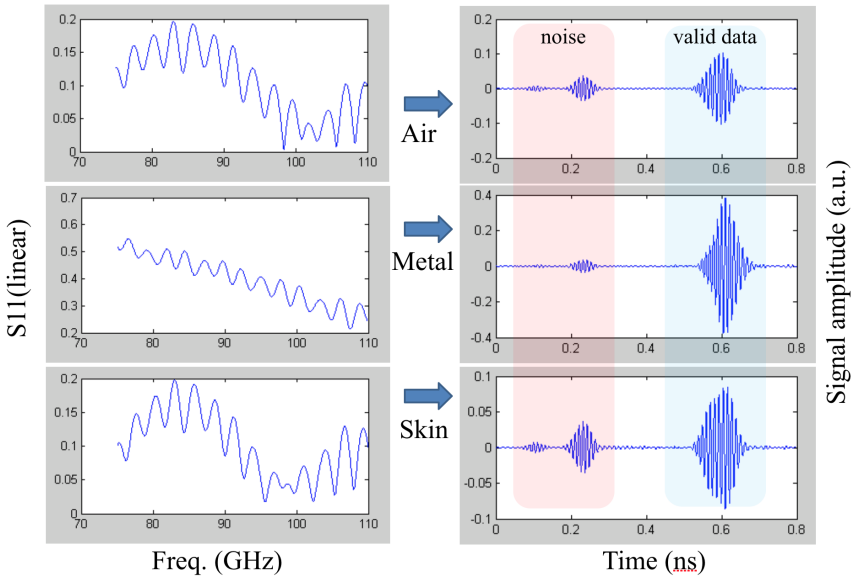

Figure 3.25: Three series of measurements (air, metal and skin) for calibration and application of TDR to measurement data.

converting measured S-parameter in frequency domain to time domain using the TDR function. In time-domain converted data, the noise signal and valid data can be clearly distinguished. Detailed code using Matlab software is described in Appendix.

3.6 Estimation of Dielectric Property of Palm Skin

3.6.1 Measurement Protocol

In vivo measurements was performed of the palm skin reflection coefficient. Subject palm skin is measured right after moderate exercise during 10 min. Physiological parameters are recorded simultaneously to estimate those effect on dielectric constant of each skin layer. The blood pressure, the heart pulse rate and temperature of the skin were measured as shown in Figure 3.26 a), b) and d). In order to prevent the movement of the hand of subject, the target hand was fixed to a frame made of gypsum. The measurement site is marked on the palm (hypothenar) as shown in Figure 3.26 c). The measurements were done using a VNA (Anritsu MS4640B VectorStar) in the spectral range of $75-110$ GHz (W-band). The results of these measurements compared with reflectance calculated by two-layer model where the dielectric constant of each layer is assigned by Debye relaxation theory.

3.6.2 Experimental Results

The dielectric constant of the palm was estimated using Equation 3.11. A schematic of measurements for subject is presented in Figure 3.26 e). As can be seen in Figure 3.27, reflection spectrum gradually changes during measurement time 15 minute. It is measured right after the exercise described in Section 3.6.1. In the subsequent measurements, as the subject relaxed back to the calm state. Measured physiological parameters were

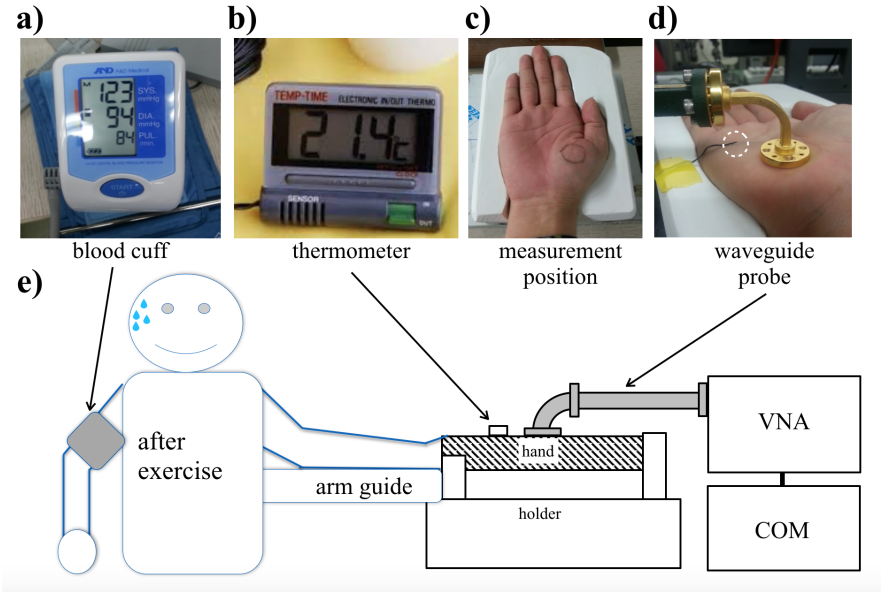

Figure 3.26: Schematic of experimental setup. Multiple physiological parameter are measured with reflection of skin simultaneously. a) Blood cuff for blood pressure and pulse rate. b) Thermometer for skin temperature. c) A gypsum frame was used to rest the hand of subject. d) Reflection measurement using open-ended rectangular waveguide probe. white dotted circle indicate temperature sensor attached on skin surface. e) Illustration of measurement.

Table 3.6: Fitted Debye parameter (Equation 3.11) of skin layers

Parameter	Lower boundary	Fitting value	Upper boundary	Literature [22]
$\varepsilon_{1,\infty}$	2	3.93	10	3.63
$\Delta\varepsilon_1$	3	11.38	15	9.7
σ_1	0	0.65	1	0
$\varepsilon_{2,\infty}$	2	5.54	10	4.52
$\Delta\varepsilon_2$	3	17.11	40	27.2
σ_2	0	3.88	7	1.4
d_1	200	300.97	400	420

observed to change rapidly at the beginning of the measurement. The S11 parameters, reflection coefficient of the skin varies in similar manner. It is

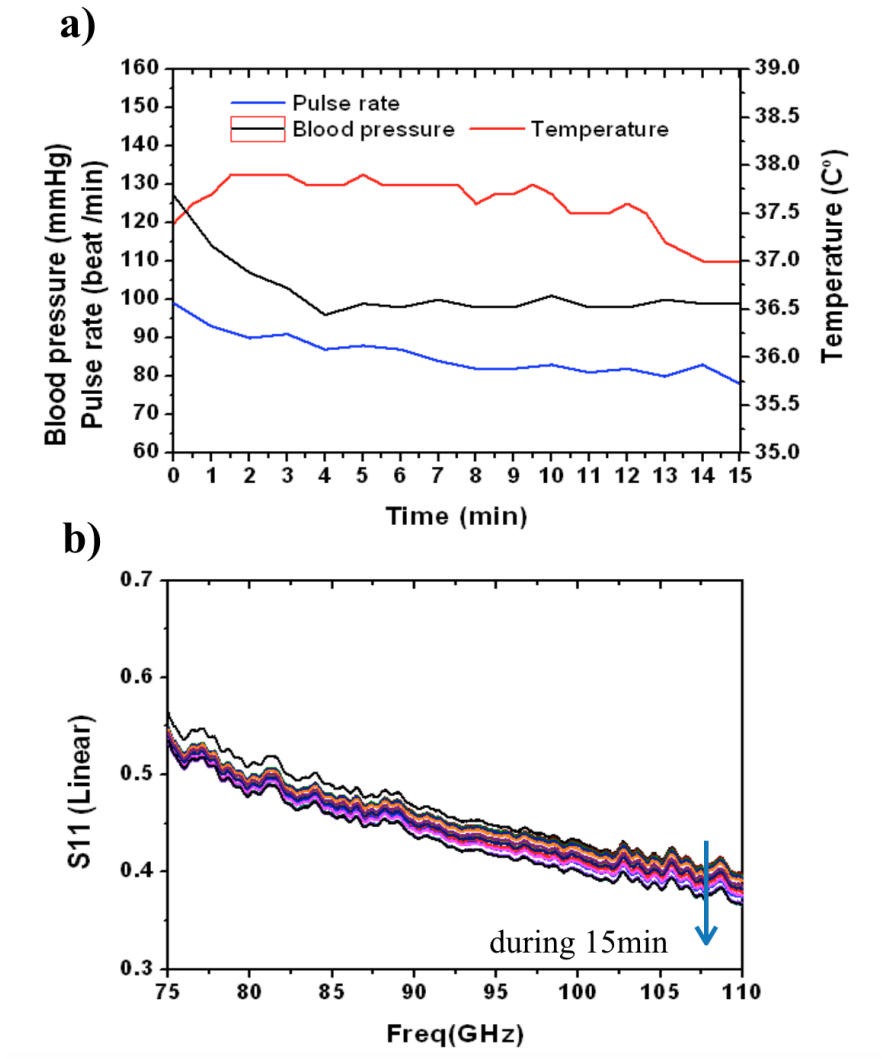

Figure 3.27: a) Time varying physiological parameters. b) Variation of S11 of palm skin during measurement time (15 min).

implies that the physiological condition of the person could affect the reflection characteristic of skin by changing its the dielectric constant. As shown in Figure 3.28 a), the reflection coefficient (Equation 3.12) calculated from

the measured S-parameter and the two-layer model (Figure 3.10). Dielectric constant of each layer is expressed by the Debye relaxation model and is fitted according to the algorithm described in Figure 3.19 by nonlinear least-square method. The fitting values for the parameters of the Debye mitigation model for each layer are given in Table 3.6. The fitting results were compared with the literature values [22] and confirmed to be well estimated. Figure 3.28 b) is a comparing the real values of the dielectric constant of each layer obtained from the two-layer skin model with the literature values.

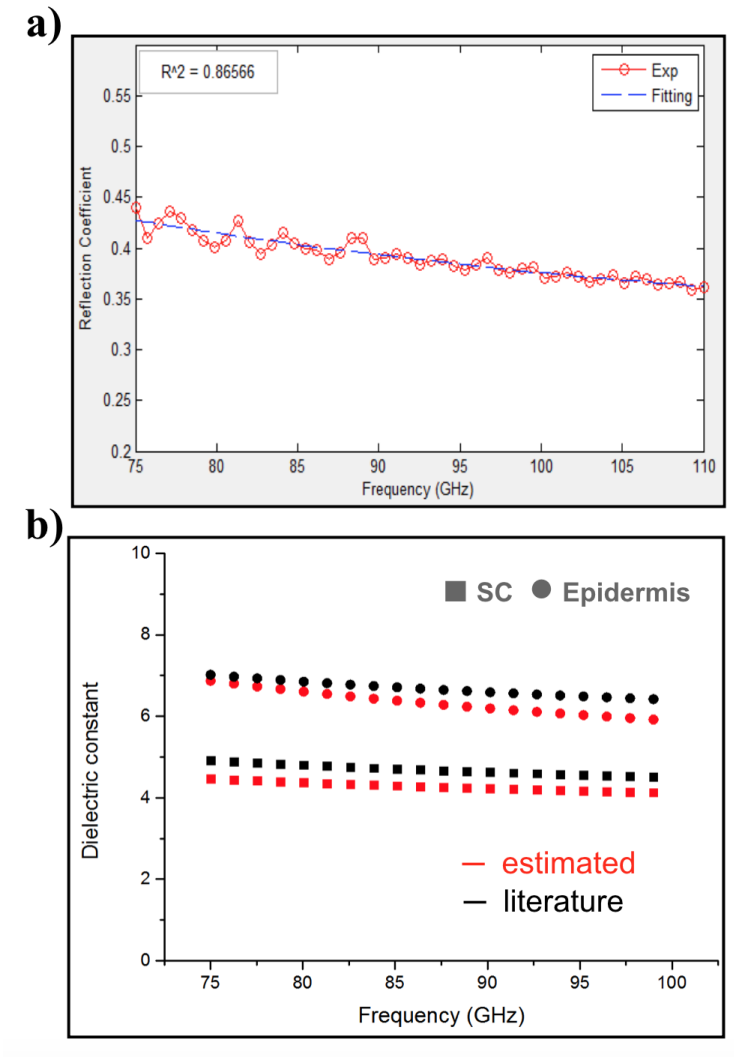

Figure 3.28: Estimated dielectric properties of palm skin. a) Reflection of skin is fitted using two-layer skin with Debye relaxation model. b) Comparison with estimated and literature value [22] of dielectric constant of palm skin.

3.7 Conclusion

The sub-structure of palm skin was measured using OCT. The major sub-structures were the multilayered skin and the helical sweat duct in stratum corneum. Considering the penetration depth of sub-THz, the skin could be simplified to a dielectric material with a stratum corneum and a epidermal/dermal layer. The antenna properties of modeled sweat glands were evaluated using FDTD simulation. Although the sweat glands had an antenna characteristic due to the spiral shape, it was confirmed that the effect was not great when the conductivity of the sweat glands and the glands of the sweat glands were within the lossy skin. Simulation shows that the main reason for determining the reflection spectrum of the skin in the sub-millimeter wave is the Fabry-Perot interference effect due to the multi-layer structure. The dielectric constant of each layer of skin was modeled using the Debye dielectric relaxation theory and the dielectric constant of the stratum corneum was derived by fitting the experimental results measured with VNA at W-band. The simulation results in this section are used to simulate the dielectric constant of the stratum corneum at subsequent section.

Bibliography

[1] E. Berardesca, P. Elsner, K.-P. Wilhelm, and H. I. Maibach, *Bioengineering of the skin: methods and instrumentation*, vol. 3. CRC Press, 1995.

[2] J. Sandby-Møller, T. Poulsen, and H. C. Wulf, "Influence of epidermal thickness, pigmentation and redness on skin autofluorescence," *Photochemistry and photobiology*, vol. 77, no. 6, pp. 616–620, 2003.

[3] O. P. Gandhi and A. Riazi, "Absorption of millimeter waves by human beings and its biological implications," *IEEE Transactions on Microwave Theory and Techniques*, vol. 34, no. 2, pp. 228–235, 1986.

[4] J. D. Jackson, *Classical electrodynamics*. John Wiley & Sons, 2007.

[5] S. Huclova and J. Fröhlich, *Modeling of Cell Suspensions and Biological Tissue for Computational Electromagnetics* . PhD thesis, University of Bern, 2011.

[6] D. Bruggeman, "Berechnung verschiedener physikalischer konstanten von heterogenen substanzen. iii. die elastischen konstanten der quasiisotropen mischkörper aus isotropen substanzen," *Annalen der Physik*, vol. 421, no. 2, pp. 160–178, 1937.

[7] K. Asami, "Characterization of heterogeneous systems by dielectric spectroscopy," *Progress in polymer science*, vol. 27, no. 8, pp. 1617–1659, 2002.

[8] O. Spathmann, M. Zang, J. Streckert, V. Hansen, M. Saviz, T. M. Fiedler, K. Statnikov, U. R. Pfeiffer, and M. Clemens, "Numerical Computation of Temperature Elevation in Human Skin Due to Electromagnetic Exposure in the THz Frequency Range," *Terahertz Science and Technology, IEEE Transactions on*, vol. 5, pp. 978–989, Nov. 2015.

[9] Y. Feldman, A. Puzenko, P. Ben Ishai, A. Caduff, I. Davidovich, F. Sakran, and A. J. Agranat, "The electromagnetic response of human skin in the millimetre and submillimetre wave range," *Physics in Medicine and Biology*, vol. 54, pp. 3341–3363, May 2009.

[10] M. Ney and I. Abdulhalim, "Modeling of reflectometric and ellipsometric spectra from the skin in the terahertz and submillimeter waves region," *Journal of Biomedical Optics*, vol. 16, no. 6, p. 067006, 2011.

[11] Y.-S. Lee, *Principles of Terahertz Science and Technology*. Springer, Oct. 2010.

[12] D. Huang, E. A. Swanson, C. P. Lin, J. S. Schuman, W. G. Stinson, W. Chang, M. R. Hee, T. Flotte, K. Gregory, C. A. Puliafito, *et al.*, "Optical coherence tomography," *Science (New York, NY)*, vol. 254, no. 5035, p. 1178, 1991.

[13] T. Gambichler, V. Jaedicke, and S. Terras, "Optical coherence tomography in dermatology: technical and clinical aspects," *Archives of Dermatological Research*, vol. 303, pp. 457–473, June 2011.

[14] M. R. Hee, D. Huang, E. A. Swanson, and J. G. Fujimoto, "Polarization-sensitive low-coherence reflectometer for birefringence characterization and ranging," *JOSA B*, vol. 9, no. 6, pp. 903–908, 1992.

[15] V. Westphal, S. Yazdanfar, A. M. Rollins, and J. A. Izatt, "Real-time, high velocity-resolution color doppler optical coherence tomography," *Optics Letters*, vol. 27, no. 1, pp. 34–36, 2002.

[16] S. TAKAGI and M. TAGAWA, "Predominance of right-handed spirals in the intraepidermal sweat ducts in man and the primates," *The Japanese journal of physiology*, vol. 7, pp. 113–118, 1957.

[17] I. M. Freedberg, *Dermatology*, vol. 282 of *Fitzpatrick's Dermatology in General Medicine, vols 1-2*. JAMA, Aug. 1999.

[18] S. R. Tripathi, E. Miyata, P. B. Ishai, and K. Kawase, "Morphology of human sweat ducts observed by optical coherence tomography and their frequency of resonance in the terahertz frequency region," *Scientific Reports*, vol. 5, p. S266, Mar. 2015.

[19] "CST." `https://www.cst.com/`. Accessed: 2017-07-22.

[20] N. A. Taylor and C. A. Machado-Moreira, "Regional variations in transepidermal water loss, eccrine sweat gland density, sweat secretion rates and electrolyte composition in resting and exercising humans," *Extreme Physiology & Medicine*, vol. 2, no. 1, p. 4, 2013.

[21] R. H. Cole, "Time domain reflectometry," *Annual review of physical chemistry*, vol. 28, no. 1, pp. 283–300, 1977.

[22] S. I. Alekseev, A. A. Radzievsky, M. K. Logani, and M. C. Ziskin, “Millimeter wave dosimetry of human skin,” *Bioelectromagnetics*, vol. 29, pp. 65–70, Jan. 2008.

Chapter 4

Spectroscopic Study on Hydration Dynamics of Friction Ridge

4.1 Introduction

Holding a glass of water, manipulating touch displays, and assessing the nature of the objects are every daily task that involve the friction between the fingertip skin and the physical environment [1]. Central nerve system controls moisture by perspiration and trans-epidermal water loss to regulate the temperature and hydration level of outermost skin, called stratum corneum [2], thus affecting tactile perception [3, 4, 5, 6] and object manipulation [7, 8, 9] by altering friction properties of skin. Considering together the central role of moisture level to fingertip-surface friction in both tactile perception and object manipulation and the highest density of sweat glands on fingertip in our body [10], it is not surprising that many studies attempt to reveal friction mechanism between fingertip and contacting surface under perspiration or moist condition [11, 12, 13]. The use of impermeable flat surfaces to examine friction evolution under perspiration or moist condition strongly prove that a fingertip moisture has dominant role in producing wide-ranging values for friction [14]. At the beginning of the moisture increase, the frictional force gradually increases, and when the water level

exceeds the threshold value, the frictional force drops. This phenomenon is described by the bell-curve behavior because the friction mechanism change from capillary adhesion to mixed lubrication when skin become wet [12]. Recently, Andre et al. [15] reported that fingertip moisture tended toward optimum value at which grip friction is maximal during object manipulation. A full understanding of physical mechanism behind moisture regulation has proven elusive. Recent development of high-resolution optical coherent tomography (OCT) has clearly revealed that the fingerprint has a trapezoidal semi-periodic three-dimensional lattice structure with a period of half mm on average and a depth of 0.1 mm [16, 17]. The structure of the fingerprint is very similar to the grating structure used in spectroscopy, holograms, and vacuum electronic devices. Therefore, it can be inferred that it can act as a resonant circuit capable of interacting with the structure size of the fingerprint and the appropriate wavelength, ie, THz wave (0.3 - 3 THz, wavelength 0.1 - 1 mm). THz wave shows high absorption by water due to the rearrangement of water molecules at the molecular level. As a result, it shows a large contrast ratio in the spectrum depending on the presence of water molecules, so it is very easy to sense the moisture of the skin [18, 19].

Here, spectral resonance and dynamics of friction ridge skin will be presents. This results implies that the moisture regulation effect cannot be fully explained without considering morphology of friction ridges.

4.2 Effect of Skin Hydration on Friction

In this section, effect of skin hydration on skin friction will be presented. Skin surface constantly exposed by ambient atmosphere. To prevent from dehydration of skin, moisture are constantly perspired from beneath of the skin [20]. This phenomena causes occlusive hydration when finger touches object surface. Hydration of outer most skin, called stratum corneum, make skin less stiff and it affect to skin friction properties.

4.2.1 Perspiration of Palm Skin

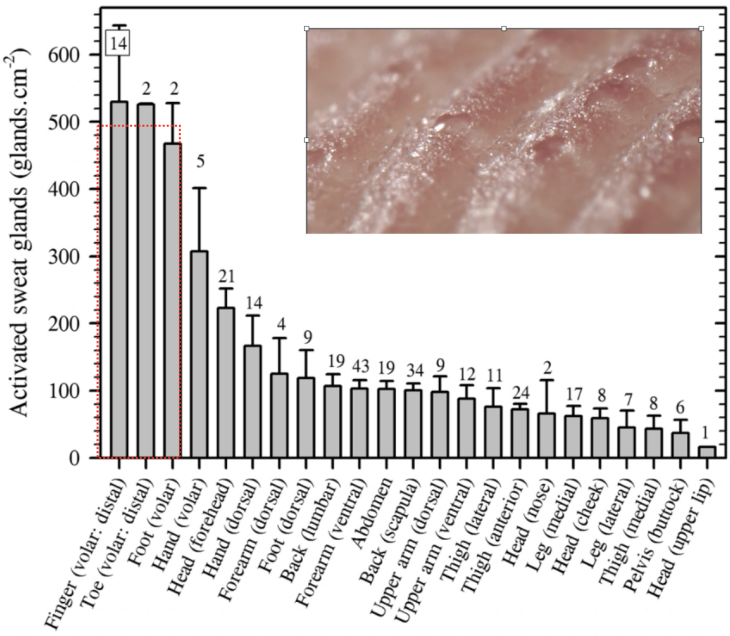

Figure 4.1: Regional variation of sweat glands duct density [10]. Inset shows finger pad in sweating condition. Sweat is secreted along the ridge of fingerprint.

The human skin has sweat glands that are directly secreted to the skin surface by apocrine sweat glands (fluid), exocrine sweat glands (intestinal fluids), and apocrine sweat glands (intestinal fluids). The focus of this section is the eclectic sweat glands, which are mainly distributed on palm skin. Figure 4.1 shows that the number of activated sweat gland duct in sweating for friction ridge skin including palm is highest than other skin position in body [10]. In palm skin, sweat pores are only located in ridge of fingerprint or friction ridge as shown in inset of Figure 4.1. Sweat bound in the stratum corneum [21] or in the form of liquid films in the interface [22] is most important single factor influencing the friction of human skin. The hydration of the human skin is controlled through physiological processes, physical activity and environmental condition (humidity and temperature).

4.2.2 Friction of Skin in Moist Condition

With increasing hydration, the corneocytes on the stratum corneum becomes softer [22, 23]. The protrusions on the moist skin surface can be more easily flattened, thereby increasing the contact area. As a result, friction increases. As the water content of the skin surface increases due to perspiration, the local formation of the meniscus is promoted, and when the lubrication effect occurs, the friction force may decrease. Increasing the coefficient of friction of moist skin compared to dry skin and reducing the frictional force of excess water on the contact surface is depicted as bell-curve behavior in Figure 4.2 [24].

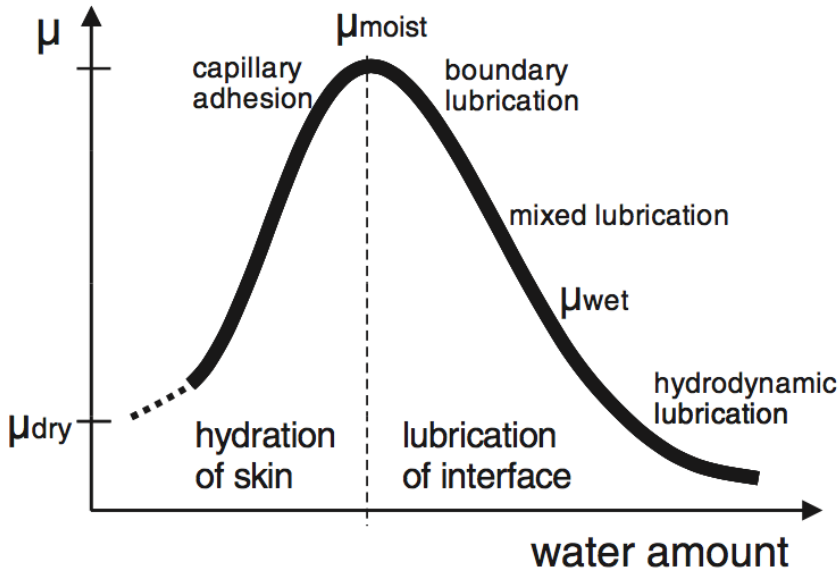

Figure 4.2: The bell-curve behavior of the friction coefficient μof human skin as a function of skin hydration. [24].

4.3 Experimental Investigation of Skin Hydration and Friction Dynamics

4.3.1 Hydration Sensing using Capacitive Sensor

A capacitance sensor (Corneometer CM 825) was used to measure the hydration of ridge part of the friction ridge skin. This subsection is mainly concerned with the description of the measurements principle of the skin hydration sensor using capacitance method. Using the proper design of the alternating electrodes, the frequency of the current and the vibrating electronic circuit, the Corneometer device measures the capacitance contribution of the skin in contact with the measuring electrode.

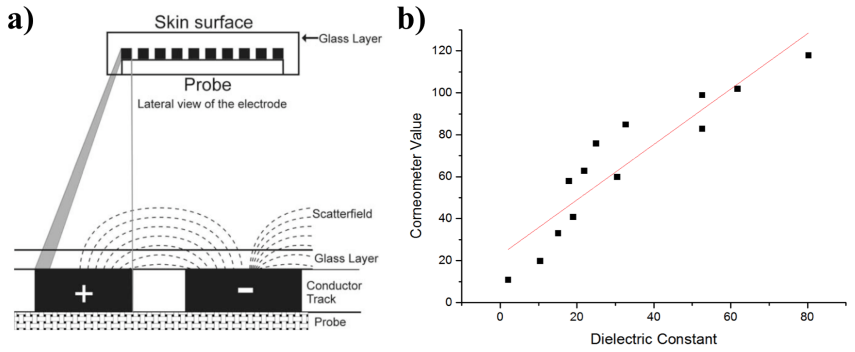

Figure 4.3: a) Schematic representation of the measuring probe of the capacitance apparatus, Corneometer CM 825. b) Corneometer values shows linear relation with dielectric constant which in linked to hydration level. Date in [25] is reploted.

The active area of the electrode covers a surface of 7 x 7 mm. The width of the electrode is 50 µm and the interdigital spacing is 75 µm. The electrodes are covered with a low dielectric glass material with a thickness

of 20 μm (Figure 4.3). When an alternating current is applied to the surface of the skin, the shape and depth of the electric field in the skin contact the dielectric material (constant capacitance C_0) covering the electrode and the skin (variable capacitance C). As a result, the entire system (the top of the electrode and the skin) has variable capacitance. The total capacitance is affected by changes in the dielectric constant of the biomaterial contacting the electrode. The overall capacitance of this system varies according to hydration level, especially the stratum corneum. The instrument's resonance system measures the frequency shift of the oscillating system due to changes in the total capacitance of the surface. Operating frequency of corneometer shifts from 1.15 MHz (dry) to 0.95 MHz (hydrated) according to skin hydration level [26]. All measurement to obtain hydration level of skin were performed under normal force at 1 ± 0.5N.

4.3.2 Friction Measurement Setup

To measure finger friction, a method of putting a finger on a moving plate with a motor was adopted. The friction measurement setup used in this experiment is shown in Figure 4.4. The unit consists of two load cells, one of which is used to catch the lateral force and is placed on the side of the plate and the other is placed under the plate to measure the normal load when the plate is moving.

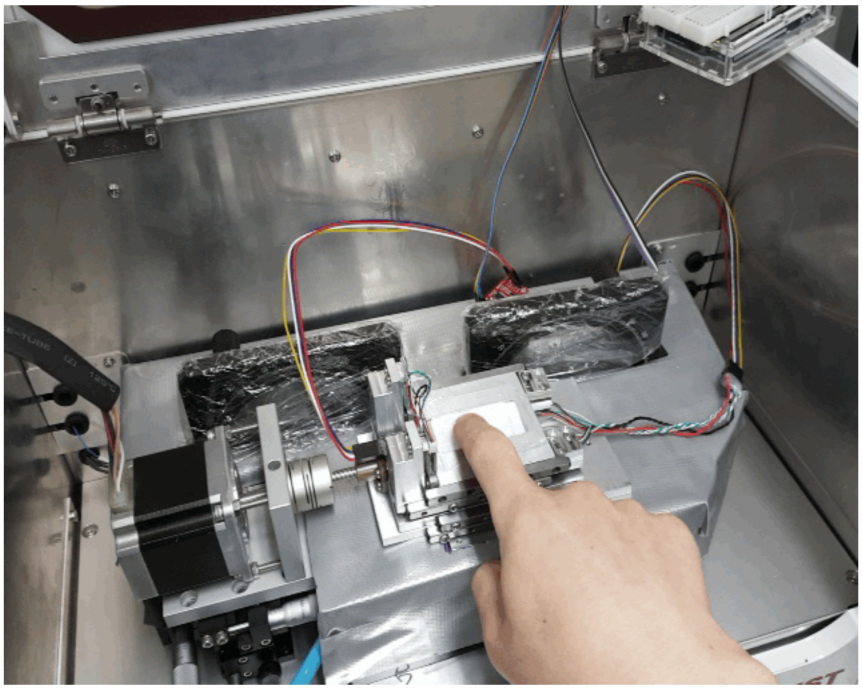

Figure 4.4: Finger friction measurement setup combined with motorized stage.

4.3.3 Measurement Procedure

All measurements were performed in an environmental control laboratory at 23.5 $\pm$ 0.5 °C and 40 $\pm$ 2% relative humidity. A middle finger of left hand of a young healthy male adult (age 31) was used for all the experiments reported here. Before each experiment, subjects flushed their fingers with a dilute aqueous solution of a weak anionic surfactant and removed any remaining water with a dry towel. After then, subject stayed in the environmental control laboratory for about 10 minutes. All nominal 'dry' measurements were taken after exposure to the dry, high pressure nitrogen gas

for at least 30 seconds. The 'wet' state (ie, the state where the excess liquid was added) was measured without removing remaining water after dipping the finger in the desalted water for 1 second. The 'sweating' measurement was performed after 10 minutes of light walking within the environmental control laboratory with the latex gloves in hand.

4.3.4 Results and Discussion

Fingerprint hydration measurement and friction measurement were performed to reveal the rrelation between the fingerprint structure, hydration and friction force. The level of hydration was measured using Corneometer as described in Section 4.3.1 and the home-made system introduced in Section 4.3.2 was used for friction measurement. All measurements were performed under the protocol described in Section 4.3.3. First, the hydration of skin surface was measured over time for flat skin (forearm, thigh) and friction ridged skin (finger, toe) to compare the hydration dynamics. In the case of skin with friction ridge structure, it took about 50 seconds for the hydration to saturate, whereas for skin without friction ridge structure, saturation of the hydration level was not observed during measurement for 5 minutes.

The finger contact area was measured by the ink imprint method to compensate for the reduction of the sensor value due to the reduction of the contact surface due to the fingerprint structure (Figure 4.5). The actual contact area of friction ridge skin with respect to the sensor measurement area was reduced to 60% - 70%. This is in agreement with the value of the literature studied for the reduction of the contact surface due to the fingerprint

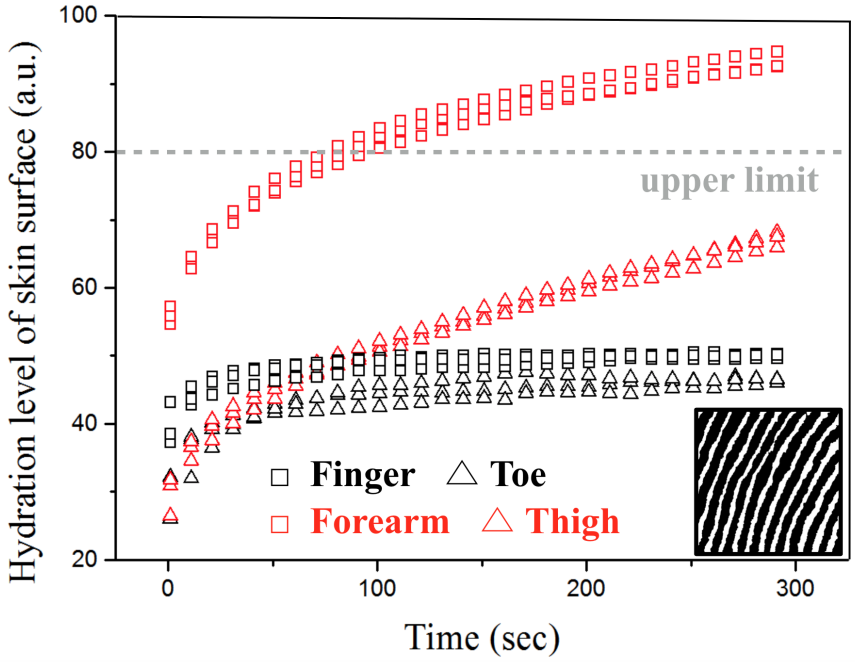

Figure 4.5: Dynamics of hydration level of skin surfaces. The tendency of hydration according to time of fingerprinted skin and fingerprintless skin shows different behavior. Gray dashed line indicates saturation of hydration value of friction ridge skin normalized by its contact area (inset).

structure [27]. The normalized value of the measured contact surface does not exceed 80 (a.u.). If the ridge is hydrated by moisture from sweat, it will have a rising value that does not saturate within measurement period, like other skin areas that do not have a fingerprint structure. This suggests that the structure of the friction ridge might have moisture control function that is not yet proove. To ensure that the hydration of the Friction ridge skin is controlled, we have artificially created a situation where the hydration levels at the beginning of the measurement are different, as described in Section 4.3.3. Three measurements were performed in each of the 'dry', 'sweating'

and 'wet' conditions, and each measurement was rested for at least 10 minutes in an environmental control laboratory to initialize skin hydration.

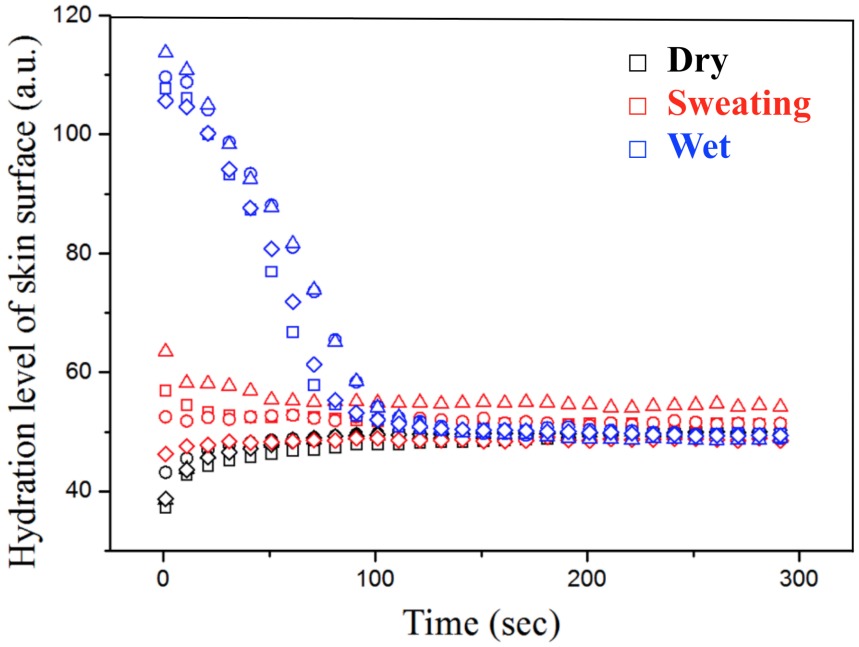

Figure 4.6: Dynamics of hydration level of skin surfaces of different initial conditions.

As shown in Figure 4.6, initial hydration levels of the skin were formed below 40 (a.u.) and above 100 (a.u.) in the 'dry' and 'wet' states, respectively. In the 'sweating' state, the hydration level was formed between 45 and 65 (a.u.). Surprisingly, it has been observed that the hydration dynamics over time converge to a constant value regardless of the initial hydration level of the friction ridge skin. The temporal changes of friction force were measured for 'dry' and 'wet' states with lower and upper limits of skin hydration level (Figure 4.7). The initial value of the coefficient of friction at

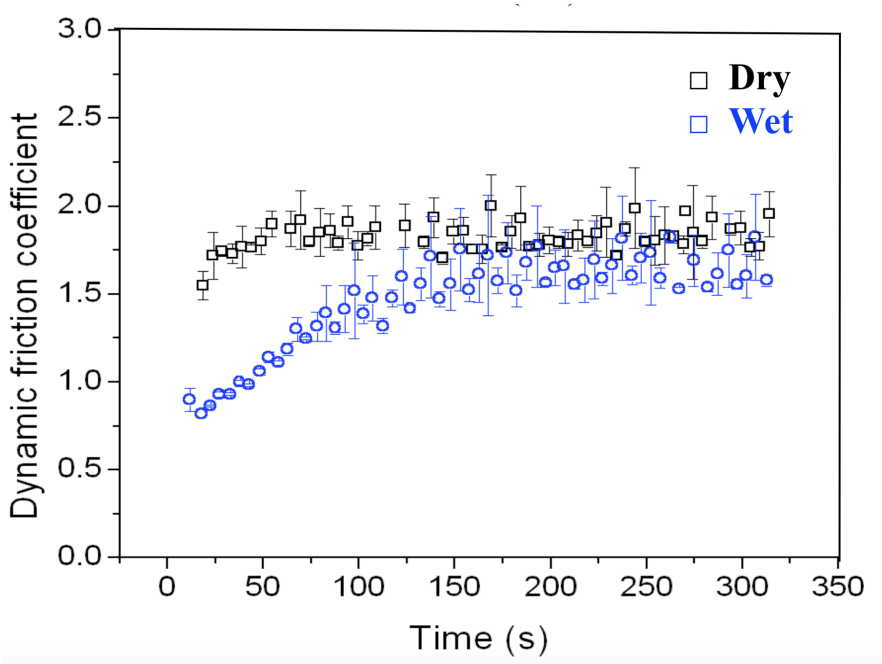

Figure 4.7: Dynamics of friction coefficient of fingerprint in different initial conditions.

'wet' state is lower than at 'dry' state, which is interpreted to be due to the fact that the liquid water at the skin surface is present at the interface between the skin and the contact surface and acts like a lubricant [22]. As time elapsed, the friction coefficient also tended to converge to the same value regardless of the initial hydration level of the skin, similar to the dynamics of the skin hydration level. The tendency of friction coefficient with skin hydration appears clearly When the coefficient of friction and hydration level are plotted as a one-to-one matching of measurement time (Figure 4.8). It is interesting to observe that most of the data point are concentrated around the intermediate level of hydration (50 a.u.). Moreover, these results sug-

gest that there is an optimal level of hydration at which friction force is maximized.

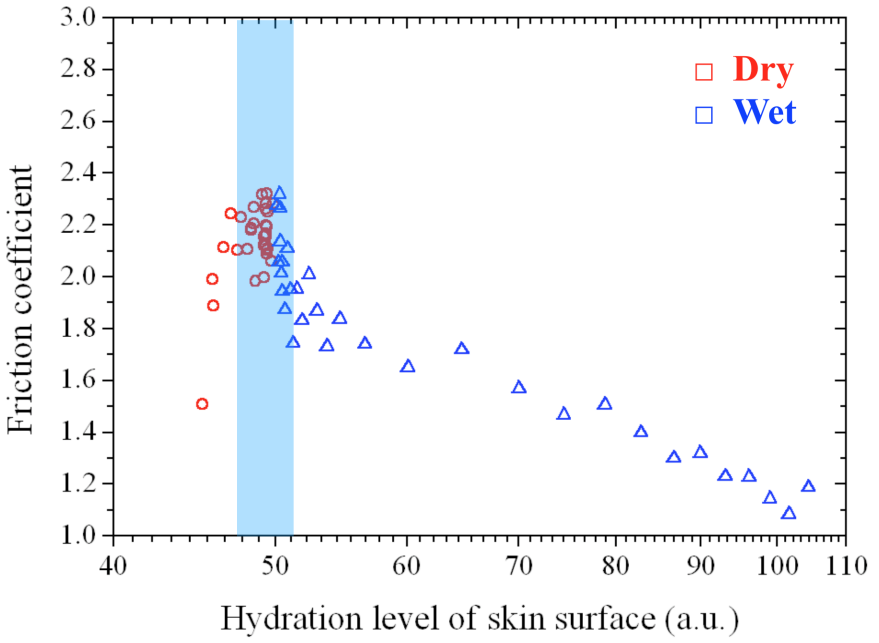

Figure 4.8: Relationship between friction coefficient and hydration level for friction ridge skin.

The present results implies that hydration level of friction ridge skin is controlled and controlled value of hydration provides the optimum friction force. This results are consistent with claims of previous study [15] which suggests that the skin's moisture level is modulated to maximize the grip force. In addition, it gives a better understanding that the hydration level is controlled by the presence of the friction ridge structure.

4.4 Resonant Behavior of Friction Ridge Skin

Friction ridge structure is a half periodic structure with a period of half-mm and a depth of 0.1 mm. Interestingly, the dimensions of this structure are very similar to the wavelength of THz wave. In addition, THz wave has a huge interaction with water and therefore has high contrast to transmitted or reflected signal according to presence of water. Therefore, it can be assumed that this electromagnetic wave could be an optimized tool for studying the hydration level of the friction structure. In this section, study of the THz wave spectrum of the friction ridge structure will be present.

4.4.1 Morphology of Friction Ridge

Here, we use sweep source OCT (Thorlab, MEMS-VESEL SSOCT) to obtain morphology of the friction ridge structure was. The measurement volume was set as 10 x 5 x 2.84 mm3 and the measured permittivity was set as 1.4, which is the normal skin permittivity at 1300 nm wavelength [28]. The pixels in the image are 1012 x 500 x 405, and the resolution per pixel in each axis is x = 9.88 μm, y = 10 μm, z = 7.02 μm. As can be seen in Figure 4.9, the friction ridge skin is formed in a semi-periodical trapezoidal lattice structure. The height of ridge to valley and distance between the ridges were measured based on spatial coordinates of green dot markers shown in Figure 4.9 c). The height of the fingerprints measured is 83.7 μ m $\pm$ 10.8 μ m and the average spacing in the measured cross section is 432 μ m $\pm$ 31.5 μ m.

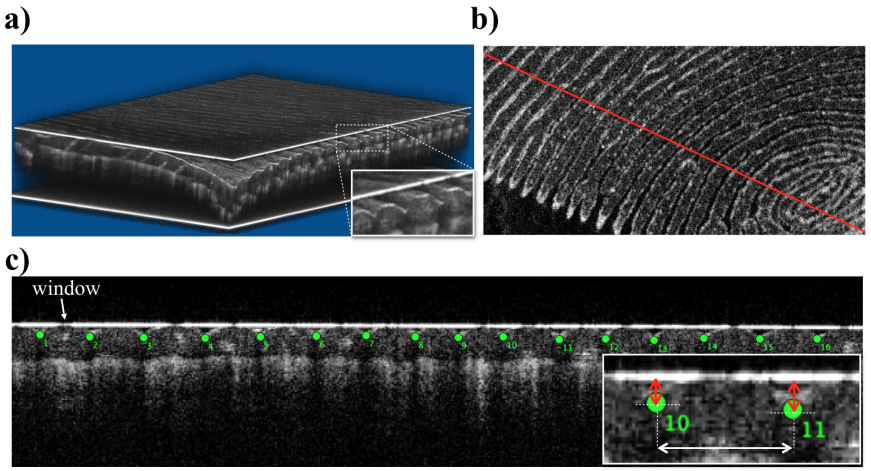

Figure 4.9: Morphology of friction ridge obtained by OCT. a) 3D view of finger pad morphology. It is clearly shown that friction ridge has trapezoidal shaped (Inset). b) Top view and c) cut view of finger pad. White solid line shown in a) and c) is window/air or window/ridge interface. Solid red line in b) indicated cut line for cut view. Height and distance between ridges are measure with help of green dot marker in c). Inset of c) shows how to measure height and distance between ridges.

4.4.2 Estimation of Spectral Response of Friction Ridge

A friction ridge structure with semi-periodic trapezoidal lattice structure can be modeled as a trapezoidal dielectric grating structure with its period D and height h, as shown in Figure 4.10. When the incident wave is incident on the structure, the reflected wave can exist in a superposition of 0th order and higher order diffractions as described in Figure 4.10. In this section, it will be discussed on the 0th order diffraction, in other words reflection, which has the strongest reflection wave intensity. If higher order diffractions are excluded, wavenumber of reflected wave from the friction ridge structure are preserved in the x direction; direction perpendicular to the

fingerprint texture. Therefore, effective two-layer dielectric slab model can be approximated as discussed in Section 3.4.1. The first layer has an average

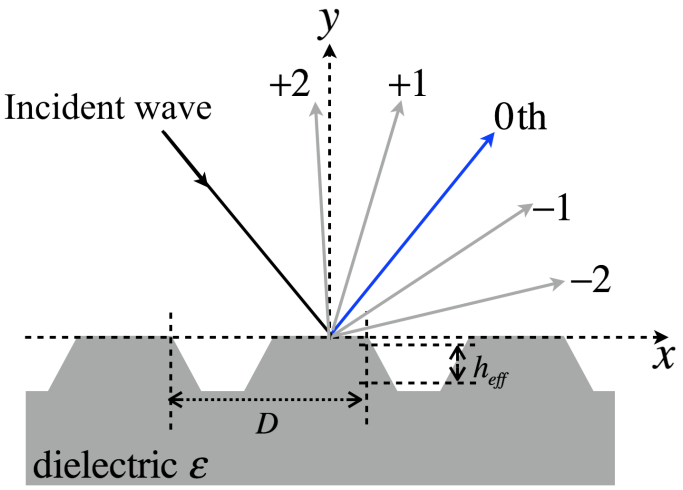

Figure 4.10: Diffraction modes of trapezoidal dielectric grating structure. D and h_{eff} represent period and effective height. Due to periodical structure, reflection (0th) and diffraction (nth) modes can be occur.

dielectric constant of air and a dielectric as ε_{eff} with effective thickness h_{eff}. The second layer is approximated by an infinite thickness dielectric with a dielectric constant ε. In this case, the electric field of reflected wave from approximated two-layers system can be expressed as Equation 4.1. Here, r_{ridge} is a reflection coefficient of the electromagnetic wave reflected from the ridge portion of the fingerprint and r_{valley} is the reflection coefficient of the electromagnetic wave reflected from the fingerprint valley portion. σ indicates the polarization of the incident electromagnetic wave. With similar discussion as in Section 3.4.1, Fabry-Perot resonance can appear in friction

ridge structure, which can be expressed by Equation 4.2.

$$E_{0th} = E_0(r_{ridge} + r_{valley}(\sigma)) \tag{4.1}$$

$$f = c\frac{0.5 + \Phi(\varepsilon)/2\pi}{2\mathrm{Re}\left(\sqrt{\varepsilon}\right) h_{eff}\sqrt{1 - \left(\sin(\theta_i)/\mathrm{Re}\left(\sqrt{\varepsilon}\right)\right)^2}} \tag{4.2}$$

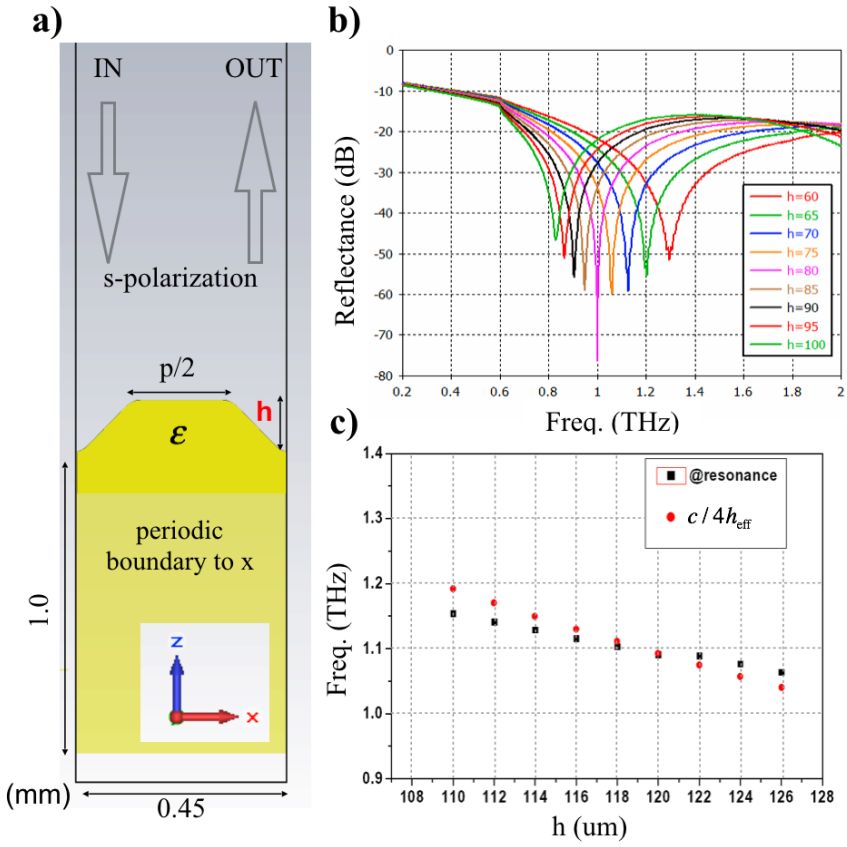

Figure 4.11: a) Simulation geometry. b) Ridge height dependence of resonance frequency. c) Comparison of resonance frequency obtained from simulation and calculation using equation 4.2 respectively.

The spectral response of the friction ridge skin in reflection geometry were confirmed using the FDTD method of CST Microwave Studio. Figure 4.11 a) shows the simulation geometry. In the simulation, the unit of length was set to 'μm', frequency was set to 0.2 - 2 THz and background was set to 'normal'. The boundary condition was set to 'periodic'. The size of the unit cell was set to a = 450 μm on one side. This is a value corresponding to 500 duct/cm^2 density of sweat glands in palm skin [10] as discussed in Section 3.4.2. Simulation results confirm that the friction ridge structure has resonance as analyzed in effective slab model and its frequency is proportional to $1/h_{\mathrm{eff}}$ as shown in Equation 4.2. (Figure 4.11 b and c)

4.4.3 THz Time Domain Polarimetry

Polarization measurement in the THz spectrum region is potentially a powerful tool in non-contact Hall measurement by Hofmann [29], detection of chiral molecules, chiral structures of proteins and DNA [30] A number of studies have therefore been reported to attempt to develop polarimetry in the THz domain [31, 32, 33]. In this study, polarization measurement setup is constructed to examine that THz spectral response of the friction ridge skin. The frequency and polarization dependence of various parts of the finger and palm were measured using a modified reflection module of the THz-TDS system with polarization tunable section(TAS7500SP, Advantest Corporation, Tokyo, Japan). THz freestanding wire grid polarizers were used (G30$\times$10-L, Microtech Instruments, Inc.) to change the direction of the polarized light incident on the skin. Figure 4.12 a) is a schematic diagram of a polarization tunable THz-TDS setup. When a femtosecond laser

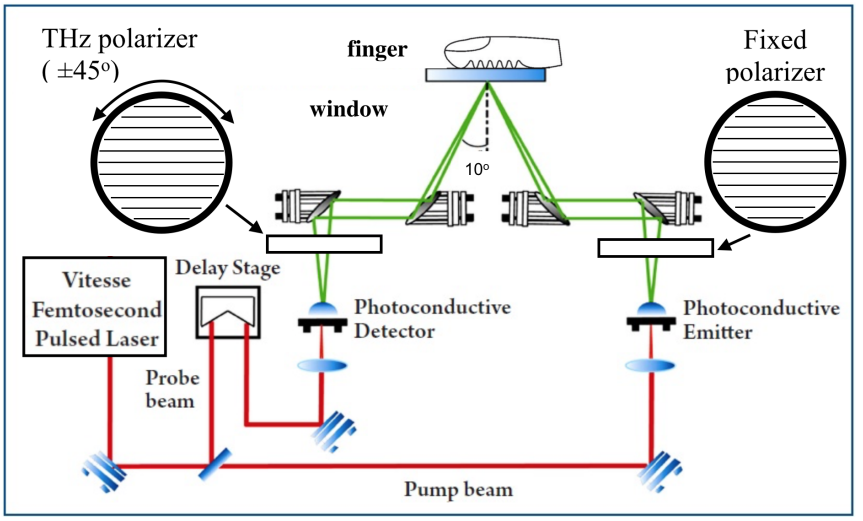

Figure 4.12: Schematic of THz time domain polarimetry.

is irradiated onto a linear dipole-shaped metal pattern (photo-conductive antenna)on an LT-GaAs substrate, a pulse with strong linear polarization of a broadband (0.1-3 THz) frequency is generated. This pulse changes polarization between -45 degrees and +45 degrees through two polarizers. Then polarized THz pulse is reflected from the sample and enters the detector. Since the detection part also uses a linear dipole antenna on the LT-GaAs substrate, it reacts sensitively to only one component of the electric field. Figure 4.12 b) shows that the graph of the electric field amplitude of the wave detected along the angle of the polarizer changes with the square of the theoretical predicted as $cos\theta$.

4.4.4 Reconstruction of Time Domain Signal

The advantage of THz-TDS is that it can analyze the structure of the sample through a pulse signal on the reflected or transmitted time domain. This method is quite similar to TDR, typically used to measure reflection site and noise elimination at the frequency of a sub-THz wave band in VNA as mentioned in Section 3.5. The skin is divided into stratum corneum, epidermis and dermis. Time delay of the pulse are used to analyze for each layer interface to verify skin disease [34, 35, 36, 37], to analyze tooth vacancy and multi-layered dielectric medium [38], to calculate the permittivity and thickness of the skin as shown in Section 3.4.1 and literature [39]. The human friction ridge located at finger-pad has height less than 0.1 mm from the surface of the skin. In order to calculate the distance between reflection surfaces through pulse delays in the time domain signal, re-shaping is essential to make indistinguishable pulse shapes from the initial broad one.

$$\mathrm{FFT}(\mathrm{impulse}) = \mathrm{FFT}(\mathrm{filter}) \otimes \mathrm{FFT}(\mathrm{signal}) \tag{4.3}$$

To do this, several studies have been carried out to modify the pulse shape to clearly distinguish the reflection plane using frequency-wavelet domain deconvolution technique using Equation 4.3 [34, 35, 40].

$$f(t) = A + B\exp\left(-(\ln(t/C))^2/2D^2\right)/\sqrt{2\pi}Dt \tag{4.4}$$

In this study, we used a log-normal Equation 4.4 as a filter function and

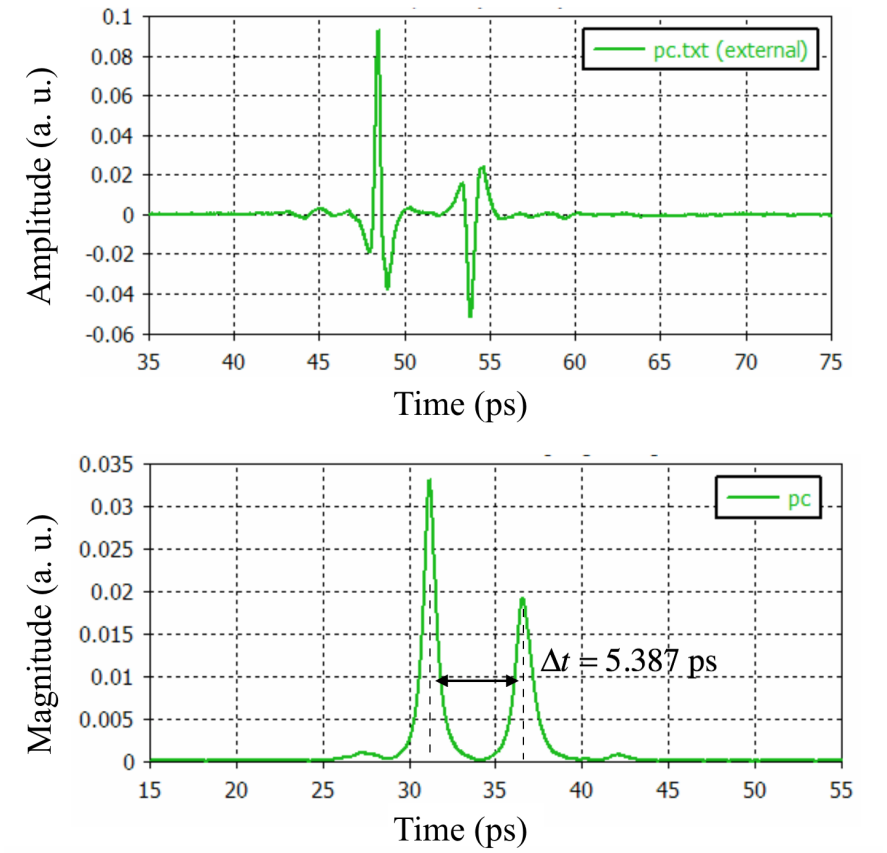

Figure 4.13: a) Raw data of reflected wave on polycarbonate with thickness of 0.5 mm. b) Reshaped signal of a).

applied it to polycarbonate with known thickness of 0.5 mm. As a result, it was confirmed that a clear reflection surface was obtained (Figure 4.13) and applied to reflected signal from friction ridge skin. We confirmed that it has a reflecting surface and analyzed it by multi-lognormal fitting method to derive the distance between two reflecting surfaces (Figure 4.14).

$$\Delta t \sim 2nd \tag{4.5}$$

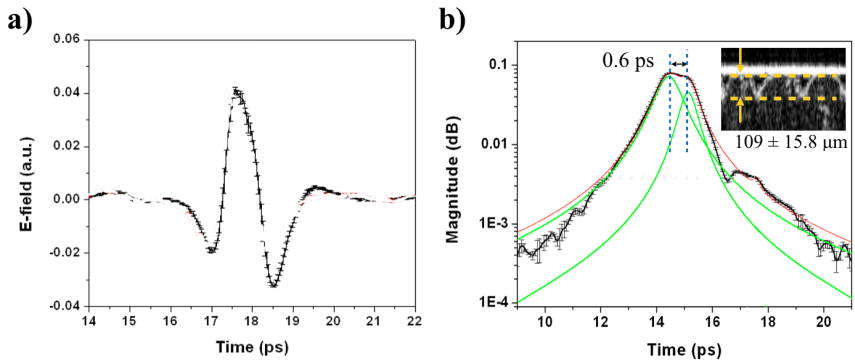

Figure 4.14: a) Typical waveform of reflected wave on friction ridge skin. b) Reflected wave reconstruction to impulse function. Green solid represents fitting curve to distinguish overlapped waves. Inset shows morphology of measurement position.

Analysis of the waveform reflected from the subject's left middle finger showed that the permittivity is reflected from two sites of 90μm distance separation using Equation 4.5. The comparison between the OCT data presented in Section (4.4.1) and the calculated values confirmed that the two reflection sites are ridge and valley of fingerprint.

4.4.5 Polarization Dependence of Resonance Spectrum

Polarization measurement setup is used to examine the THz spectral response of the friction ridge skin. If the structure of the fingerprint affects the THz reflection spectrum, the spectrum will show different dependence depending on the polarization direction due to the trapezoidal lattice structure. The frequency and polarization-dependent reflectance of the finger and palm parts were measured using the reflection module of the THz-TDS polarimetry system described in Section 4.4.3. The THz pulse changes polarization

between -45 degrees and +45 degrees using two polarizers. The polarized THz pulse is reflected from the friction ridge skin and enters the detector.

When the polarization of the THz wave is parallel to the direction of the

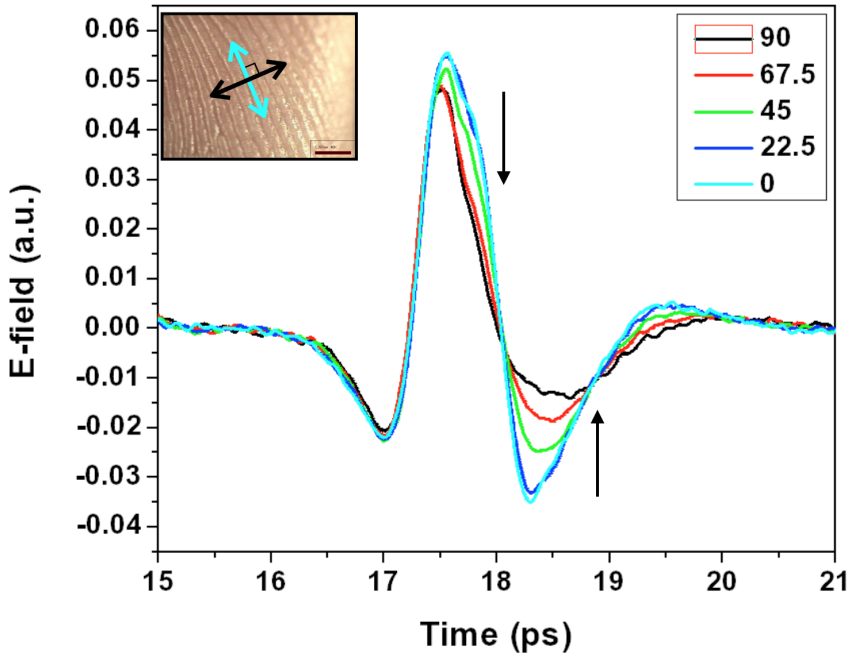

Figure 4.15: Polarization dependence of reflected signal. Tale part of reflected signal reduced when polarization of incident THz wave become perpendicular to friction ridge.

fingerprint, it is called 0 degree. When it is incident perpendicular to the direction of fingerprint resolution, it is called 90 degrees. As can be seen in Figure 4.15, the signal in the time domain reflected from the friction ridge skin changes dynamically according to the direction of incident polarization. In particular, it can be seen that as the direction of polarization approaches 90 degrees, the signal at the tail of the measured signal decreases.

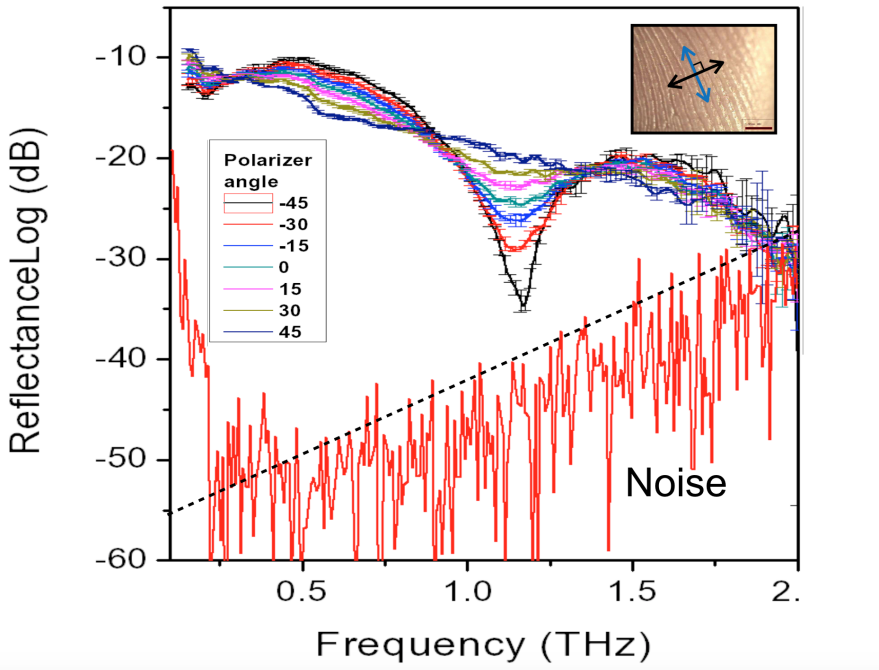

Figure 4.16: Polarization dependence of resonance spectrum. Resonance become week when polarization of incident THz wave become perpendicular to friction ridge. Resonance spectrums are located above the noise level, which confirms validity of data.

This indicates that the signal in the valley part of the fingerprint is reduced on the basis of pulse reconstruction analysis in Section 4.4.4. The reflected time domain signal is converted by FFT to confirm the THz spectrum (Figure 4.16). It is observed strong dependence on the direction of polarization to resonant behavior when the THz wave was incident in parallel to fingerprint texture. Interestingly, the resonance disappears when the direction of polarization is perpendicular to the fingerprint texture. Since the friction ridge skin has been confirmed to be polarization dependent, it can be said that the fingerprint structure has a strong influence on the THz spectrum and

causes resonance. All data validity are confirmed by checking that hey exist above the noise level of THz-TDS system.

4.5 Hydration Dynamics of Friction Ridge Skin

The results in Section 4.3.4 confirmed that hydration levels are controlled and friction values are optimized for contact with objects in friction ridge skin. In this section, monitoring of resonance frequency under occlusion condition were performed to examine how friction ridge structure play a role in hydration level of fingerprint. In the same environment as the friction force experiment and the hydration level measurement experiment, THz spectrum of finger-pad were measured in an environmental control laboratory at 23.5 $\pm$ 0.5 °C and 40 $\pm$ 2% relative humidity. A middle finger of left hand of a young healthy male adult (age 31) was used for all the experiments presented here. Before each experiment, subjects flushed their fingers with a dilute aqueous solution of a weak anionic surfactant and removed any remaining water with a dry towel. After then, subject stayed in the environmental control laboratory for about 10 minutes. All measurements were taken after exposure to the dry, high pressure nitrogen gas for at least 30 seconds. Figure 4.17 shows the spectral variation over time of middle finger in occlusion state followed by touch action. The resonance behavior is observed in the vicinity of about 1.1 - 1.2 THz frequency and It changes with a certain tendency depending on time. The resonance frequency with the time shows a gradual blue shift tendency. As discussed in the previous section 4.4.2, the origin of resonance is due to the destructive interference

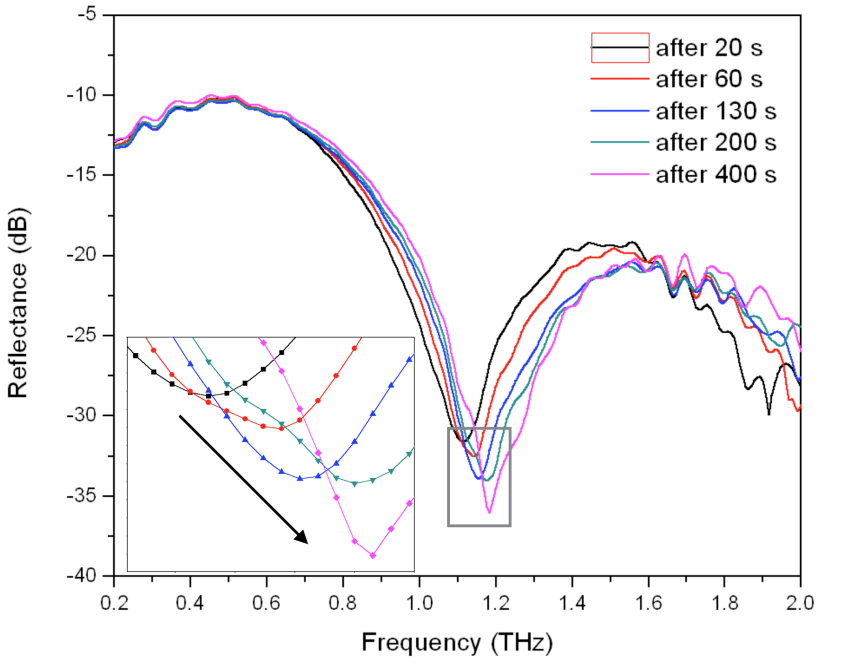

Figure 4.17: Dynamics of resonance frequency during touch action.

between ridge and valley parts of the fingerprint, hence it implies that the reflection coefficient of each part changes with time. To confirm that this is a phenomenon due to the hydration of the fingerprint structure, relative humidity (RH%) around the fingerprint is measured simultaneously with the THz resonance during whole measurement. The RH% sensor for this purpose has a measurement range of 0-100 RH% and operates with an error range of ± 2 RH% (SHT75, Sensirion). A strong correlation between the resonance frequency and the RH% adjacent to friction ridge skin surface is clearly observed. The correlation was quantified in terms of the correlation

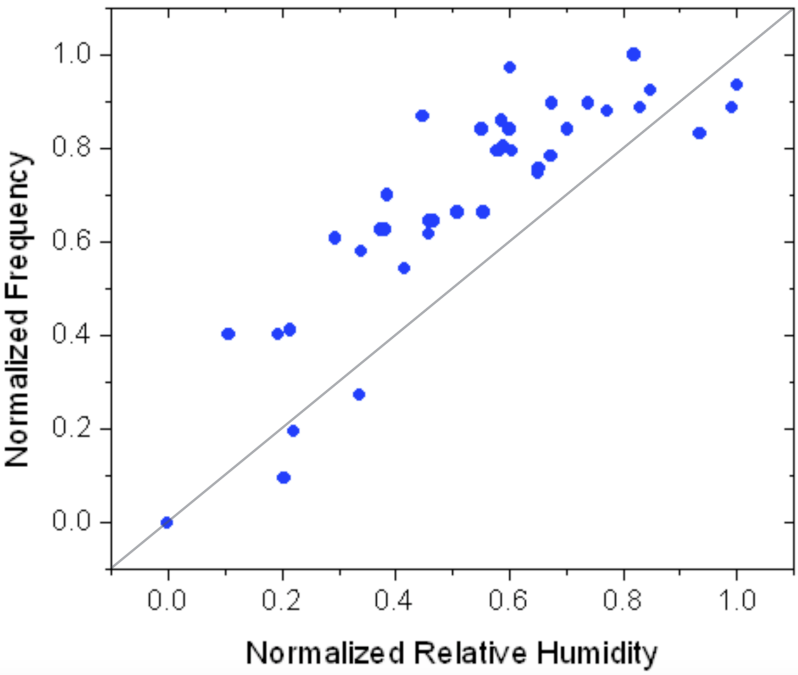

Figure 4.18: The correlation graph between normalized RH% and resonance frequency, obtained for 300 sec after touch action.

parameter given by

$$r = \frac{\sum_{i=1}^{n}(x_i - \bar{x})(y_i - \bar{y})}{\sqrt{\sum_{i=1}^{n}(x_i - \bar{x})^2}\sqrt{\sum_{i=1}^{n}(y_i - \bar{y})^2}}, 0 \leq r \leq 1. \tag{4.6}$$

The value of r for the correlation between the resonance frequency and the RH% was found to be r = 0.851 (Figure 4.18). This indeed indicates the significant correlation between them and expresses the fact that essentially they exhibit similar temporal behavior. In order to substantiate that the observed phenomena are related in function of friction ridge on hydration control, a FDTD simulation was performed assuming that excess moisture due

to sweat builds up in the valley of fingerprint structure. Interestingly, as the amount of water (represented by height) accumulated in the valley of fingerprint structure increases, the spectral resonance of the friction ridge structure gradually tends to shift blue similar to the experiment (Figure 4.19). Thus, it is possible that the observed resonance shift phenomena reflect changes that occur in the water accumulation in the valley of the fingerprint structure. That is, the structure of the fingerprint serves as a reservoir of moisture, which implies the possibility of controlling the contact surface moisture.

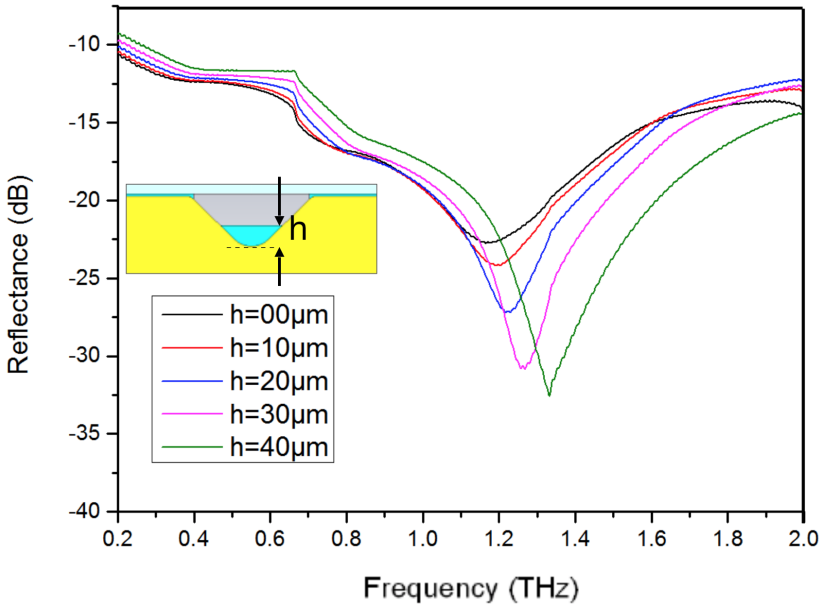

Figure 4.19: FDTD simulation results on the assumption sweat accumulation in valley of friction ridge. Inset shows simulation geometry. *h* indicates moisture accumulation height in valley of fingerprint structure.

4.6 Conclusion

In this study, we used a time domain THz spectroscopy to monitor changes in moisture of fingerprint structure. We found that the structure of the fingerprint has resonance in the THz frequency range. We found that the change of resonance with time has a strong correlation with the humidity around the finger. It is shown that this resonance varies with time, which is strongly correlated with the humidity around the finger. This phenomenon can be caused by the adsorption of moisture on the surface of the fingerprint structure. This result is well matched with expectation of FDTD simulation that the permittivity and structure of the fingerprint structure changes due to the adsorption of moisture. It is observed that the touch friction force was kept constant despite the continuous increase in the amount of moisture adsorbed to the fingerprint due to occlusion. Moreover, it is observed that the frictional force was maximized when the hydration level of ridge portion of friction ridge saturated. This implies that the fingerprint structure might helps to keep the friction force constant by controlling moisture in touch action.

Bibliography

[1] L. A. Jones and S. J. Lederman, *Human hand function*. Oxford University Press, 2006.

[2] P. Agache and P. Humbert, *Measuring the skin*. Berlin, Heidelberg: Springer Berlin Heidelberg, 2004.

[3] A. Kl cker, M. Wiertlewski, V. Th ate, V. Hayward, and J.-L. Thonnard, "Physical Factors Influencing Pleasant Touch during Tactile Exploration," *PLOS ONE*, vol. 8, p. e79085, Nov. 2013.

[4] P.-H. Cornuault, L. Carpentier, M.-A. Bueno, J.-M. Cote, and G. Monteil, "Influence of physico-chemical, mechanical and morphological fingerpad properties on the frictional distinction of sticky/slippery surfaces," *Journal of The Royal Society Interface*, vol. 12, p. 20150495, Aug. 2015.

[5] D. Gueorguiev, S. r. n. Bochereau, A. Mouraux, V. Hayward, and J.-L. Thonnard, "Touch uses frictional cues to discriminate flat materials," *Scientific Reports*, vol. 6, p. 4486, May 2016.

[6] M. l. Wiertlewski, R. Fenton Friesen, and J. E. Colgate, "Partial squeeze film levitation modulates fingertip friction," *Proceedings of the National Academy of Sciences*, vol. 113, pp. 9210–9215, Aug. 2016.

[7] T. Andre, V. Levesque, V. Hayward, P. Lefevre, and J. L. Thonnard, "Effect of skin hydration on the dynamics of fingertip gripping contact," *Journal of The Royal Society Interface*, vol. 8, pp. 1574–1583, Sept. 2011.

[8] N. K. Veijgen, M. A. Masen, and E. van der Heide, "Relating Friction on the Human Skin to the Hydration and Temperature of the Skin," *Tribology Letters*, vol. 49, pp. 251–262, Nov. 2012.

[9] S. Kondo and H. Hasegawa, "Sweat Absorption Reduces the Frictional Force Between a Finger Pad and the Surface of a Flat Plate," *ITE Transactions on Media Technology and Applications*, vol. 5, no. 1, pp. 17–23, 2017.

[10] N. A. Taylor and C. A. Machado-Moreira, "Regional variations in transepidermal water loss, eccrine sweat gland density, sweat secretion

rates and electrolyte composition in resting and exercising humans," *Extreme Physiology & Medicine*, vol. 2, no. 1, p. 4, 2013.

[11] S. M. Pasumarty, S. A. Johnson, S. A. Watson, and M. J. Adams, "Friction of the Human Finger Pad: Influence of Moisture, Occlusion and Velocity," *Tribology Letters*, vol. 44, pp. 117–137, Aug. 2011.

[12] S. E. Tomlinson, R. Lewis, X. Liu, C. Texier, and M. J. Carré, "Understanding the Friction Mechanisms Between the Human Finger and Flat Contacting Surfaces in Moist Conditions," *Tribology Letters*, vol. 41, pp. 283–294, Oct. 2010.

[13] B. M. Dzidek, M. J. Adams, J. W. Andrews, Z. Zhang, and S. A. Johnson, "Contact mechanics of the human finger pad under compressive loads," *Journal of The Royal Society Interface*, vol. 14, p. 20160935, Feb. 2017.

[14] S. Derler and L. C. Gerhardt, "Tribology of Skin: Review and Analysis of Experimental Results for the Friction Coefficient of Human Skin," *Tribology Letters*, vol. 45, pp. 1–27, Oct. 2011.

[15] T. Andre, P. Lefevre, and J. L. Thonnard, "Fingertip Moisture Is Optimally Modulated During Object Manipulation," *Journal of Neurophysiology*, vol. 103, pp. 402–408, Jan. 2010.

[16] P. Cimalla, J. Walther, M. Mehner, M. Cuevas, and E. Koch, "Simultaneous dual-band optical coherence tomography in the spectral domain for high resolution in vivo imaging," *Optics Express*, vol. 17, no. 22, p. 19486, 2009.

[17] M. J. Adams, S. A. Johnson, P. Lefevre, V. Levesque, V. Hayward, T. Andre, and J. L. Thonnard, "Finger pad friction and its role in grip and touch," *Journal of The Royal Society Interface*, vol. 10, pp. 20120467–20120467, Dec. 2012.

[18] S. Fan, Y. He, B. S. Ung, and E. Pickwell-MacPherson, "The growth of biomedical terahertz research," *Journal of Physics D: Applied Physics*, vol. 47, pp. 374009–9, Aug. 2014.

[19] B. C. Q. Truong, H. D. Tuan, A. J. Fitzgerald, V. P. Wallace, and H. T. Nguyen, "A Dielectric Model of Human Breast Tissue in Terahertz Regime," *IEEE Transactions on Biomedical Engineering*, vol. 62, no. 2, pp. 699–707, 2015.

[20] G. Yosipovitch, A. Maayan-Metzger, P. Merlob, and L. Sirota, "Skin Barrier Properties in Different Body Areas in Neonates," *Pediatrics*, vol. 106, pp. 105–108, July 2000.

[21] A. O. Barel, M. Paye, and H. I. Maibach, *Handbook of cosmetic science and technology*. CRC Press, 2014.

[22] M. J. Adams, B. J. Briscoe, and S. A. Johnson, "Friction and lubrication of human skin," *Tribology Letters*, vol. 26, pp. 239–253, Mar. 2007.

[23] L.-C. Gerhardt, V. Strässle, A. Lenz, N. Spencer, and S. Derler, "Influence of epidermal hydration on the friction of human skin against textiles," *Journal of The Royal Society Interface*, vol. 5, no. 28, pp. 1317–1328, 2008.

[24] S. Derler, R. M. Rossi, and G. M. Rotaru, "Understanding the variation of friction coefficients of human skin as a function of skin hydration and interfacial water films," *Proceedings of the Institution of Mechanical Engineers, Part J: Journal of Engineering Tribology*, vol. 229, pp. 285–293, Mar. 2015.

[25] E. Berardesca, H. Maibach, and K. Wilhelm, *Non invasive diagnostic techniques in clinical dermatology*. Springer Science & Business Media, 2013.

[26] E. Berardesca, H. I. Maibach, and K.-P. Wilhelm, eds., *Non Invasive Diagnostic Techniques in Clinical Dermatology*. Berlin, Heidelberg: Springer Berlin Heidelberg, 2014.

[27] P. H. Warman and A. R. Ennos, "Fingerprints are unlikely to increase the friction of primate fingerpads," *Journal of Experimental Biology*, vol. 212, pp. 2016–2022, June 2009.

[28] M. J. Adams, S. A. Johnson, P. Lefevre, V. Levesque, V. Hayward, T. Andre, and J. L. Thonnard, "Finger pad friction and its role in grip and touch," *Journal of The Royal Society Interface*, vol. 10, pp. 20120467–20120467, Dec. 2012.

[29] T. Hofmann, U. Schade, C. M. Herzinger, P. Esquinazi, and M. Schubert, "Terahertz magneto-optic generalized ellipsometry using synchrotron and blackbody radiation," *Review of Scientific Instruments*, vol. 77, pp. 063902–13, June 2006.

[30] K. Yamamoto, K. Tominaga, H. Sasakawa, A. Tamura, H. Murakami, H. Ohtake, and N. Sarukura, "Terahertz Time-Domain Spectroscopy of Amino Acids and Polypeptides," *Biophysical Journal*, vol. 89, pp. L22–L24, Sept. 2005.

[31] N. van der Valk, W. van der Marel, and P. Planken, "Terahertz polarization imaging," *Optics Letters*, vol. 30, no. 20, pp. 2802–2804, 2005.

[32] N. Kanda, K. Konishi, and M. Kuwata-Gonokami, "Terahertz wave polarization rotation with double layered metal grating of complimentary chiral patterns," *Optics Express*, vol. 15, no. 18, pp. 11117–11125, 2007.

[33] L. Wang, X. W. Lin, W. Hu, G. H. Shao, and P. Chen, "Broadband tunable liquid crystal terahertz waveplates driven with porous graphene electrodes," *Light: Science & ...*, 2015.

[34] R. M. Woodward, B. E. Cole, V. P. Wallace, R. J. Pye, D. D. Arnone, E. H. Linfield, and M. Pepper, "Terahertz pulse imaging in reflection geometry of human skin cancer and skin tissue," *Physics in Medicine and Biology*, vol. 47, pp. 3853–3863, Oct. 2002.

[35] E. Pickwell, B. E. Cole, A. J. Fitzgerald, M. Pepper, and V. P. Wallace, "In vivo study of human skin using pulsed terahertz radiation," *Physics in Medicine and Biology*, vol. 49, pp. 1595–1607, Apr. 2004.

[36] C. B. Reid, A. Fitzgerald, G. Reese, R. Goldin, P. Tekkis, P. S. O'Kelly, E. Pickwell-MacPherson, A. P. Gibson, and V. P. Wallace, "Terahertz pulsed imaging of freshly excised human colonic tissues," *Physics in Medicine and Biology*, vol. 56, pp. 4333–4353, June 2011.

[37] E. P. J. Parrott, S. M. Y. Sy, T. Blu, V. P. Wallace, and E. Pickwell-MacPherson, "Terahertz pulsed imaging in vivo: measurements and processing methods," *Journal of Biomedical Optics*, vol. 16, no. 10, p. 106010, 2011.

[38] E. Pickwell, V. P. Wallace, B. E. Cole, S. Ali, C. Longbottom, R. J. M. Lynch, and M. Pepper, "A Comparison of Terahertz Pulsed Imaging with Transmission Microradiography for Depth Measurement of Enamel Demineralisation in vitro," *Caries Research*, vol. 41, pp. 49–55, Dec. 2006.

[39] S. R. Tripathi, E. Miyata, P. B. Ishai, and K. Kawase, "Morphology of human sweat ducts observed by optical coherence tomography and their frequency of resonance in the terahertz frequency region," *Scientific Reports*, vol. 5, p. S266, Mar. 2015.

[40] Y. Chen, S. Huang, and E. Pickwell-MacPherson, "Frequency-wavelet domain deconvolution for terahertz reflection imaging and spectroscopy," *Optics Express*, vol. 18, no. 2, p. 1177, 2010.

Chapter 5

Compact THz Source Development: Electron Source

5.1 Introduction

Electrons from a solid can be emitted into vacuum through quantum electron tunneling by applying substantial electric fields. Unlike conventional hot cathodes, electron emission from field emitters provide high-quality electron beams due to low thermal energy dispersion. In conventional electron devices such as X-ray sources, electron microscopes, or cathode ray tubes using thermionic emission, energy dispersion acts as noise and blurs the images; hence, field emission cathodes are attractive for obtaining clearer or higher magnification images [1, 2, 3]. Thermionic cathodes have been utilized in vacuum electronic devices to generate high-power electromagnetic waves; however, they are problematic in the high frequency range because they are bulky and cause the heating of the surrounding device housing [4], providing an emission current density that is insufficient for overcoming electron thermal random motion [5]. Therefore, cold cathode emitters that remain at room temperature (300 K) and provide a high current density at a low electric field are desirable and have been studied for various applications such as X-ray sources for medical imaging [6], high-resolution field emis-

sion electron microscopes [7], flat panel displays [8], and vacuum electronic devices [9] for border security or satellite communication. Field emission occurs in high electric fields at approximately 10–100 MV/cm, which is beyond the typical vacuum breakdown strength at approximately 100 kV/cm. In order to avoid breakdown and meet the above condition, field emitters are required to have highly sharp emission surfaces, of several to several tens of nanometers, for enhancing the electric field, with a high aspect ratio emission surface such as in a lightning rod [10].

In many of the applications mentioned above, the uniformity of the emitted electron beam is crucial for a stable and high performance. Thus, it is critical to control the sharp, high aspect ratio emission surface morphology imposed for large field enhancements. In the case of the field emission electron microscope, reactive ion etching (RIE) [11], electrical discharge machining [12], electrical aging [13], and focused ion beam (FIB) machining [14] have been used to uniformize the emission surface of a point emitter such as an LaB6 single crystal or a carbon nanotube (CNT) tip. On the other hand, flat panel displays and X-ray sources use array [15, 16], flake [17, 18] or yarn emitters [8, 19], formed by a collection of individual electron emission elements in order to obtain large emission areas and emission currents, respectively. These types of emitters are usually fabricated by microelectromechanical system technology for Si and metal-based emitters [16] and by chemical vapor deposition [20], printing methods [21], and electrophoretic deposition [17] for carbon-based emitters. Due to the limitations of the fabrication method, the individual field emission points are not equal, resulting in an uneven field emission surface. Nonuniform field

emission points inevitably result in local high field emission, accompanied by the local evaporation of the emission element and therefore, electrical breakdown due to poor vacuum [22]. This not only causes non-uniform electron emission but is also a critical obstacle in determining the lifetime of field emission devices. In order to solve these issues, it is necessary to uniformize the individual field emission points and to treat the surface using methods such as plasma treatments [23, 24], laser surface treatments [25], electrical discharging machining [26], and controlled electrical break treatments [27]. Although it is possible to obtain more stable and uniform field emissions using these methods, the random nature of the individual field emission points embedded in the fabrication method cannot be completely compensated. Therefore, most field emission cathodes have problems in that their stability and lifetime are significantly lower than those of the well-established thermionic cathodes. Recently, a field emission cathode using a graphene oxide film was developed using the modified Hummer method; it could be cut freely, mechanically, to form the desired field emission surface [28]. However, uniform control of the surface morphology has not yet been achieved in microscopic regions of the order of tens of nanometers from the surface, where field emission occurs.

Of late, graphene has generated significant interest because of its unique properties [29] and potential applications in nanoelectronics [30, 31], supercapacitors [32], field effect transistors [33], and field emitters [18, 34, 35]. The advantages of graphene over the other field emitters such as CNT is that it has a greater emission area, rendering it an excellent field emitter following the Fowler-Nordheim (F-N) equation [36], as all the other field emitters.

In this study, a novel graphene-based freestanding film, which is thinner and harder than the previous graphene-based films, is fabricated using the modified Hummer method and a hydrothermal process with oxygen reduction by nitrogen annealing. Owing to the robustness of the film, it is possible to achieve precise mechanical cutting with a microtome; a uniform field emission surface was successfully obtained only through electrical conditioning using this knife-cut surface as the field emission surface. Electron microscopy images before and after conditioning show the existence of a well-defined uniform field emission surface with a roughness under several tens of nm and uniform electron beam emission was confirmed through field emission luminescence. In addition, due to the thinness and high aspect ratio of the film, the emission current density reaches up to 300 A/cm^2 and is not significantly reduced due to the screen effect of local electric field [37] between the individual emission points, which occurs in the conventional array, flake and paste-type graphene, or in the CNT field emission cathode. As this type of field emission device can increase the theoretically infinite length, it is possible to obtain a high current. In this study, we obtained an emission current of several mA, while maintaining the current density level in the order of hundreds of A/cm^2, using a film several mm in length. The graphene-based film field emitter presented in this paper can be adopted for various applications, particularly, for miniaturized terahertz vacuum electronic devices requiring uniform high current densities and currents.

5.2 Preparation of Graphene-based Films for Field Emitters

5.2.1 Film Synthesis

Recent reports have shown that free-standing reduced graphene oxide (rGO) films can be fabricated by a chemical process using the modified Hummer method [38], followed by hydrothermal synthesis. These films are

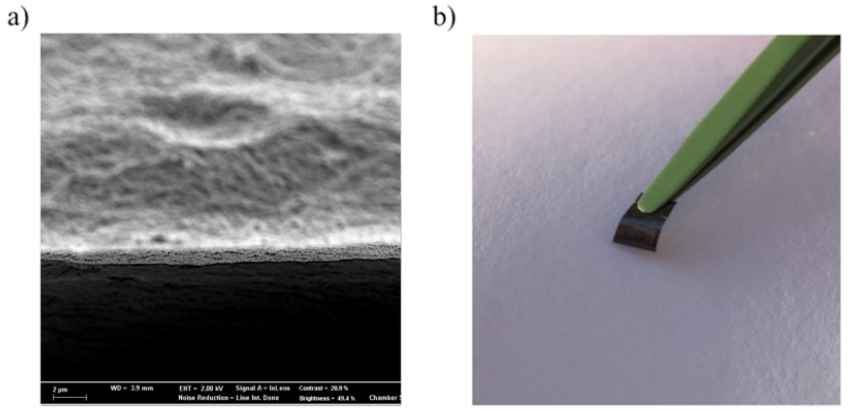

Figure 5.1: a) Fabricated reduced graphene oxide (rGO) film. b) Sufficiently robust for mechanical handling.

free-standing, highly flexible, easy to handle, and have a controllable thickness [39, 40]. In this study, we have adopted the above-mentioned method for synthesizing the films. During the hydrothermal process, the oxygen functional groups in these films are reduced to partially recover the original graphene properties. It is advantageous for our application, which requires high electrical and thermal conductivities. The field emission scanning electron microscope (SUPRA, 55 VP) image in Figure 5.1 a) depicts a multilay-

ered rGO film with a thickness of a few micrometers. Its high length-to-thickness aspect ratio enables a high enhancement factor, under an applied electric field. As shown in Figure 5.1 b), the fabricated rGO film is flexible and sufficiently robust for manual handling. For further reduction, the synthesized films are annealed in a furnace at a temperature of 800 °C, under a nitrogen environment. After the annealing process, the films are examined using energy-dispersive X-ray spectroscopy (EDS) to confirm the reduction of their oxygen ratio. The wt% of carbon and oxygen before annealing were determined to be 69% and 24%, respectively, whereas, after annealing they became 79% and 12%, respectively. This implies that the broken sp2 bonding, due to the oxygen in the graphene structure, are partially recovered after annealing [41].

5.2.2 Mechanical Shaping

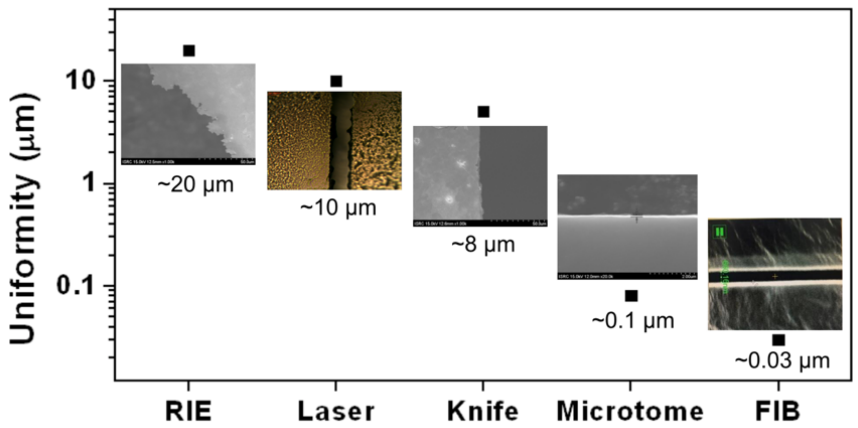

Figure 5.2: Uniformity of the rGO-film cut edge using various cutting methods.

The prepared rGO film was cut by various methods such as the RIE, laser cutting, knife cutting, microtome, and FIB to produce a uniform field emission surface. Figure 5.2 depicts the tolerances of the graphene-film sections cut using various methods. Although the FIB method provides the highest uniformity, it is inefficient and time consuming because graphene and its relatives, such as the rGO film, are strong against ion collision [42], which is the mechanism of the FIB cutting method. As the prepared rGO film is free standing for the enhancement of the field emission performance, it is difficult to mask the film tightly against ion etching. Therefore, the RIE method, which cannot provide uniform etching, is not suitable because the uniformity of the cut edge is critical. The laser-cutting method is also not suitable for rendering a uniform emission edge because it easily forms debris, as shown in the inset of Figure 5.2 because it concentrates high-density energy on a local spot and burns the material. On the other hand, due to the excellent flexibility and stiffness of the rGO film, it can be handled manually, rendering it possible to be mechanically cut; this would not be possible with ordinary graphene-film surface treatment. It exhibits good surface uniformity, even with knife cutting and microtome. In order to apply the microtome, rectangularly preshaped rGO films, using the knife cutting method, are prepared and embedded in paraffin wax, for holding, during the microtome operation. After shaping using the microtome, the paraffin wax is removed using diluted xylene solution. The less-than-100-nm protrusions and nonuniform portions remaining on the emission edge are uniformized through electrical aging by field emission.

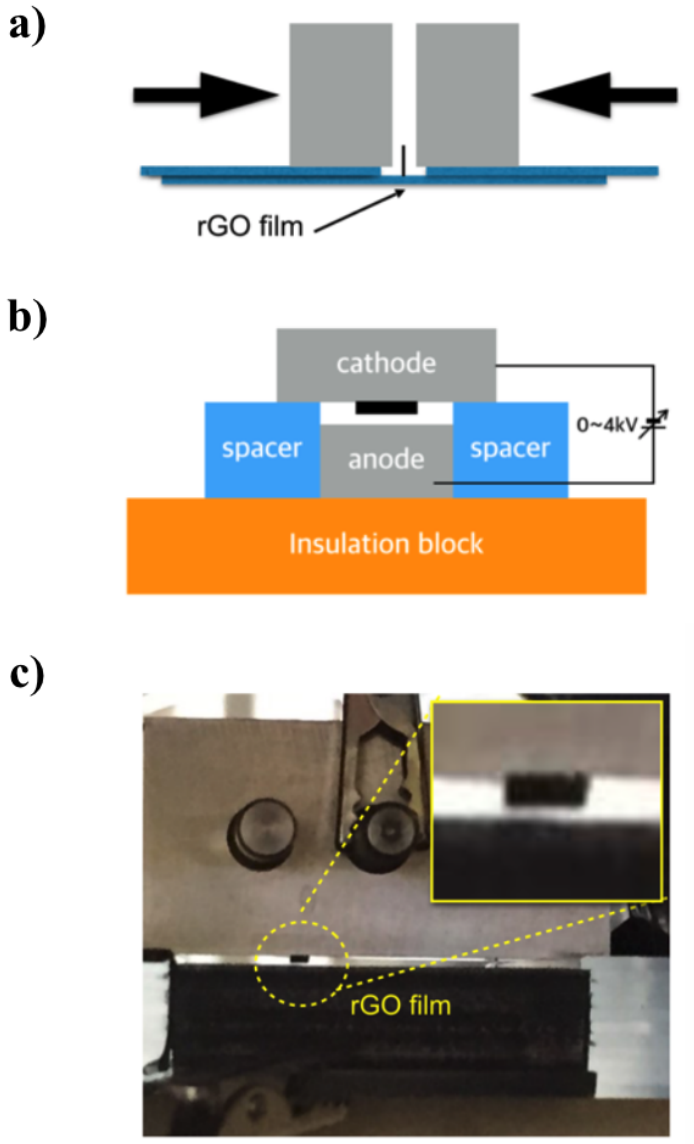

Figure 5.3: Schematic of the a) rGO film mounting method b) total test setup; c) Experimental setup installed in a vacuum chamber. Inset shows the vertically aligned rGO film between the anode and cathode blocks.

5.3 Experimental Results

The prepared rGO film was cut into a rectangular shape with an emission edge length of 3 mm and height of 5 mm. A well-shaped rGO film was sandwiched between the cathode block, made of stainless steel and screwed such that the height of the film protruding from the cathode surface was 0.5 mm (Figure 5.3 a). For electrical aging and the field emission tests, an ultra-high vacuum chamber equipped with a rotary pump (Varian, SD-300), turbo pump (Varian, Turbo-V301), and an ion pump (Varian, Vacion plus 500) was used. A diode-type experimental setup was prepared

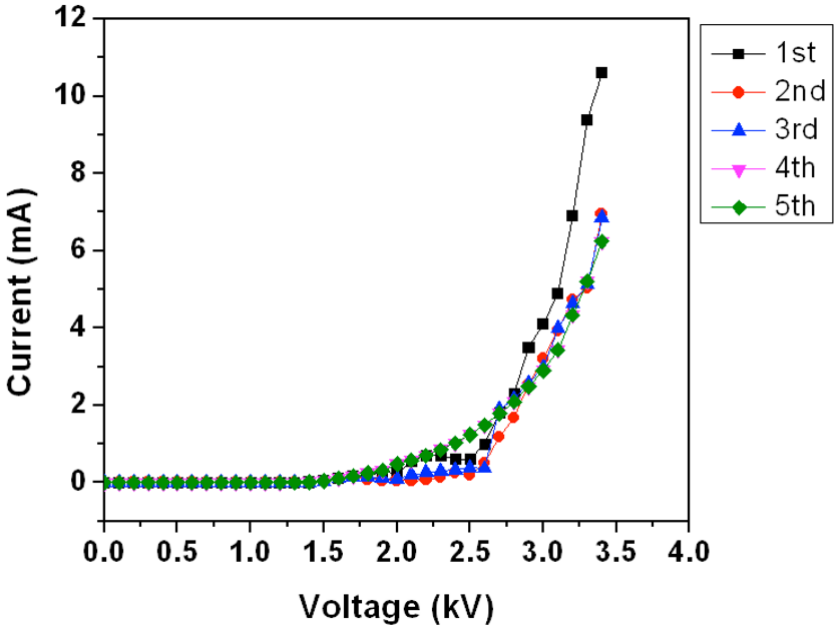

Figure 5.4: Field emission tendency to be saturated by sequential electrical aging.

by inserting a ceramic insulator spacer between the film-mounted cathode

blocks and the molybdenum anode, and carefully placed in the prepared vacuum chamber. The thickness of the ceramic insulator was 1 mm and the height of the mounted film was maintained at 0.5 mm such that the distance from the field emission surface to the anode was maintained at 0.5 mm. The schematic and photographic image of the test setup, configured with a diode setup, are displayed in Figure 5.3 b) and c), respectively. Before the start of the experiment, a vacuum level of 10^{-7}–10^{-8} Torr was created; this is retained during the experiment also. A dc voltage source (Glassman High Voltage Inc., EQ005R240C22) with the maximum output voltage of 5 kV and current of 250 mA was used; a current meter with a nano-ampere range (NI PXI-4071, 7 1/2-digit FlexDMM), connected to a computer, was used to measure the output current. There was a high risk

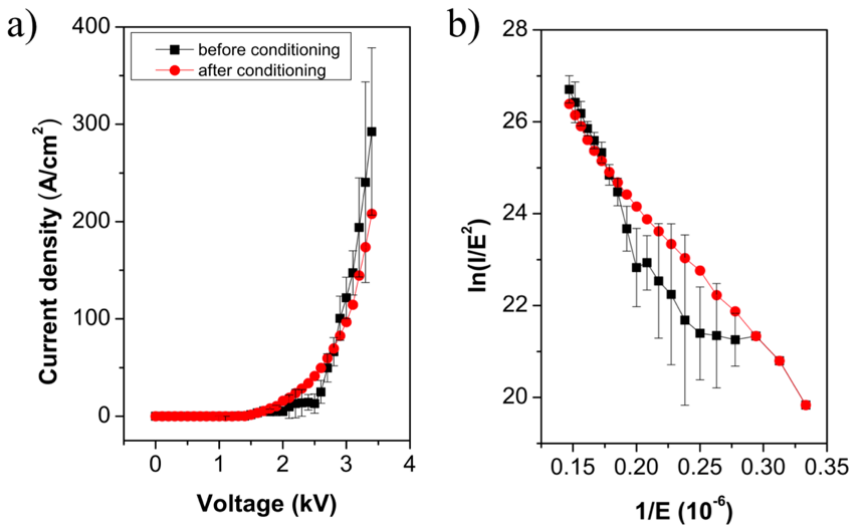

Figure 5.5: (a) I-V curves of the rGO field emitter before (red) and after (blue) treatment and (b) F-N plot of the rGO field emitter before (red) and after (blue) treatment.

of sudden electrical breakdown due to the heavy degassing rate generated by the electrons striking the anode surface. To avoid this, during the early stage of the experiment, a low step up voltage was applied for a sufficient time. To create a uniform emitting surface by electrical treatment, a design process that stepped up the applied voltage with step of 100 V was implemented. As shown in Figure 5.4, as the number of voltage cycles increases, a lower voltage is required to achieve the same field emission current level in the low voltage regime (1.5–2.5 kV). This is a variation from the carbon nanotubes that emit electrons at much lower fields, before conditioning, as presented in literature [43]. Also from Figure 5.4, as the conditioning process continues, the emission current becomes increasingly stable. In order to avoid vacuum breakdown, we maintained the upper applied-voltage limit to 3.5 kV, during conditioning. As seen in Figure 5.4, the I-V curves finally reach a narrow range with a stable emission current (the 4th and 5th curves). The surface emission current density was calculated by dividing the current obtained immediately after mounting and the saturated current after conditioning, by the emission area (Figure 5.5 a). The error bar was calculated as the deviation of first and last three experimental values, before and after conditioning, respectively. The variation in the current density before conditioning is considerable; however, it is negligible, after conditioning. This indicates that the emission edges of the rGO film become gradually clean after a series of electrical aging, as shown in Figure 5.4. The I-V characteristics, in stable operation, demonstrate that the emission current reaches up to approximately 7 mA, at an applied DC voltage of 3.5 kV. The calculated maximum current density was approximately 200 A/cm^2, (Figure 5.4 b),

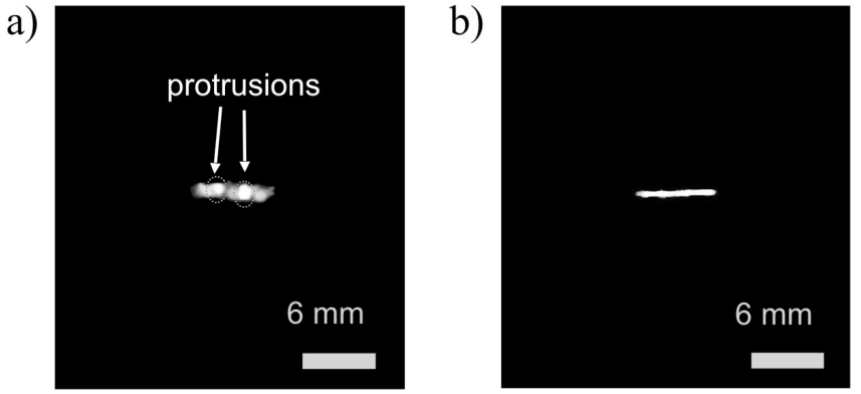

Figure 5.6: a) Before electrical conditioning and b) after electrical conditioning. It can be clearly seen that the protrusions are removed after electrical aging, in the beam images.

which is one of the highest for a free standing rGO film in stable condition, till date. Figure 5.5 b) shows the F-N plot, used to examine the field emission property of the cathode from the I-V curve; after conditioning, the gradient of the F-N plot recovered its linearity. This implies that the emission current fully originated from field-induced quantum tunneling [10].

To characterize the emission uniformity, field emission luminescence was performed using a phosphor screen on a conductive ITO glass, used as the anode. To avoid burning the phosphor elements on the ITO glass, the applied potential was retained below 2.5 kV to emit a lower current. The emission current was less than 1.25 mA, when the photograph of the ITO glass surface was taken. Before conditioning, it can be observed that the beam was broad and nonuniform, with extremely bright spots expected to be caused by a nonuniform surface with protrusions (Figure 5.6 a). On the other hand, a clear and uniform sheet-like beam mark was obtained after

electric conditioning, as in Figure 5.6 b). The width of the beam striking mark is well matched with that of the rGO emitter. Figure 5.7 shows the

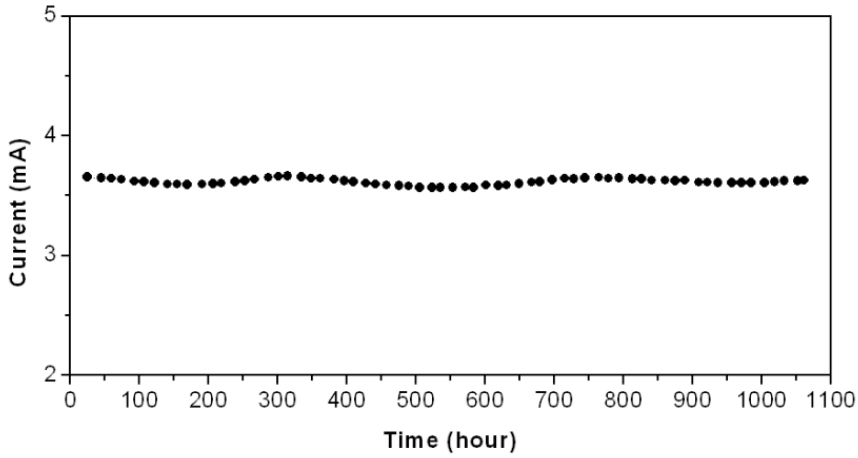

Figure 5.7: Long term field emission stability test in a DC voltage condition.

time trace of the current density at a fixed applied voltage of 3 kV for the vertically aligned rGO film, after the conditioning process. We determined the occurrence of stable electron emission for more than 40 days, under continuous operating conditions, due to the uniform emission surface obtained by electrical treatment, after mechanical shaping. Despite being operated at a higher current density of approximately 100 A/cm^2, compared to the other graphene-based field emitters, it shows a remarkable stability with fluctuations less than 5% of the emission current, during the entire stability test period. We believe that the excellent field emission properties of the rGO film edge emitter results from the higher electrical and thermal conductivities of the film, and the uniform emission surface, by emission surface conditioning. We also believe that the high aspect ratio and the vertically aligned thin

geometry increase the emission area and enhance the electric field applied to the emission surface, resulting in high current density and high current electron emission.

5.4 Conclusion

A vertically aligned freestanding graphene-based film field emitter was synthesized by annealing in nitrogen environment, after application of the modified Hummer method followed by a hydrothermal process. The field emission performance of the synthesized film was experimentally examined, using a diode configuration. Owing to its high aspect ratio with a thin film geometry, a significant current of more than 7 mA was obtained from a single field emitter by increasing the length of the emission edge, without current density loss (approximately 200 A/cm^2). The synthesized rGO films exhibited high robustness, sufficient for mechanical shaping, which is essential for obtaining uniform emission surfaces by removing the remaining small protrusions through field-induced electrical material evaporation. A controlled electrical aging process was performed to uniformize the emission edges of the rGO films, resulting in a uniform emission current and a highly-stable emission for a duration longer than 40 days, under a continuous operation condition with a negligible current degradation, less than 5% of the average emission current, during the life-time test. The high current and high current density, along with the uniform and stable field emission properties of the rGO films, are attributed to its excellent electrical, thermal, and mechanical properties, and the high aspect ratio with a vertically

aligned thin geometry; this resulted in a mechanically shape-able large emission edge with a high uniformity, without losses in the substantial electric field on the emission surface. This may pave the way for future devices, particularly, for miniaturized terahertz vacuum electronic devices that require high current, high current density, uniform, and long-term stable cold cathodes, compared to the existing ones.

Bibliography

[1] H. Nishijima, S. Kamo, S. Akita, Y. Nakayama, K. I. Hohmura, S. H. Yoshimura, and K. Takeyasu, "Carbon-nanotube tips for scanning probe microscopy: Preparation by a controlled process and observation of deoxyribonucleic acid," *Applied Physics Letters*, vol. 74, pp. 4061–4063, June 1999.

[2] N. De Jonge, Y. Lamy, K. Schoots, and T. H. Oosterkamp, "High brightness electron beam from a multi-walled carbon nanotube," *Nature Nanotechnology*, vol. 420, pp. 393–395, Nov. 2002.

[3] G. Gaertner, "Historical development and future trends of vacuum electronics," *Journal of Vacuum Science & Technology B, Nanotechnology and Microelectronics: Materials, Processing, Measurement, and Phenomena*, vol. 30, p. 060801, Nov. 2012.

[4] J. H. Booske, "Plasma physics and related challenges of millimeter-wave-to-terahertz and high power microwave generation," *Physics of Plasmas*, vol. 15, p. 055502, May 2008.

[5] S.-T. Han, J. Seok-Gy, Y.-M. Shin, K. H. Jang, J.-K. So, J.-H. Kim, S.-S. Chang, and G.-S. Park, "Experimental investigations on miniaturized high-frequency vacuum electron devices," *Plasma Science, IEEE Transactions on*, vol. 33, no. 2, pp. 679–684, 2005.

[6] E. Gidcumb, B. Gao, J. Shan, C. Inscoe, J. Lu, and O. Zhou, "Carbon nanotube electron field emitters for x-ray imaging of human breast cancer," *Nanotechnology*, vol. 25, p. 245704, May 2014.

[7] H. Zhang, J. Tang, J. Yuan, Y. Yamauchi, T. T. Suzuki, N. Shinya, K. Nakajima, and L.-C. Qin, "An ultrabright and monochromatic electron point source made of a LaB6 nanowire," *Nature Nanotechnology*, vol. 11, pp. 273–279, Nov. 2015.

[8] P. Liu, Y. Wei, K. Liu, L. Liu, K. Jiang, and S. Fan, "New-Type Planar Field Emission Display with Superaligned Carbon Nanotube Yarn Emitter," *Nano Letters*, vol. 12, pp. 2391–2396, May 2012.

[9] X. Yuan, W. Zhu, Y. Zhang, N. Xu, Y. Yan, J. Wu, Y. Shen, J. Chen, J. She, and S. Deng, "A Fully-Sealed Carbon-Nanotube Cold-Cathode Terahertz Gyrotron," *Scientific Reports*, vol. 6, p. 998, Sept. 2016.

[10] L. M. Baskin and G. N. Fursey, "Field emission from semiconductors," in *IVMC '95. Eighth International Vacuum Microelectronics Conference. Technical Digest (Cat. No.TH8012)*, p. 66, IEEE, 2007.

[11] M. A. R. Alves, D. F. Takeuti, and E. S. Braga, "Fabrication of sharp silicon tips employing anisotropic wet etching and reactive ion etching," *Microelectronics Journal*, vol. 36, pp. 51–54, Jan. 2005.

[12] W. J. Kim, J. S. Lee, S. M. Lee, K. Y. Song, C. N. Chu, and Y. H. Kim, "Better than 10 mA Field Emission from an Isolated Structure Emitter of a Metal Oxide/CNT Composite," *ACS nano*, vol. 5, pp. 429–435, Jan. 2011.

[13] H. Yamaguchi, K. Murakami, G. Eda, T. Fujita, P. Guan, W. Wang, C. Gong, J. Boisse, S. Miller, M. Acik, K. Cho, Y. J. Chabal, M. Chen, F. Wakaya, M. Takai, and M. Chhowalla, "Field Emission from Atomically Thin Edges of Reduced Graphene Oxide," *ACS nano*, vol. 5, pp. 4945–4952, June 2011.

[14] J. S. Lee, T. Kim, S.-G. Kim, M. R. Cho, D. K. Seo, M. Lee, S. Kim, D. W. Kim, G.-S. Park, D. H. Jeong, Y. D. Park, J.-B. Yoo, T. J. Kang, and Y. H. Kim, "High performance CNT point emitter with graphene interfacial layer," *Nanotechnology*, vol. 25, p. 455601, Oct. 2014.

[15] C. A. Spindt, C. E. Holland, A. ROSENGREEN, and I. Brodie, "Field-emitter arrays for vacuum microelectronics," *IEEE Transactions on Electron Devices*, vol. 38, no. 10, pp. 2355–2363, 1991.

[16] J. I. Sohn, S. Lee, Y.-H. Song, S.-Y. Choi, K.-I. Cho, and K.-S. Nam, "Patterned selective growth of carbon nanotubes and large field emission from vertically well-aligned carbon nanotube field emitter arrays," *Applied Physics Letters*, vol. 78, pp. 901–903, Feb. 2001.

[17] Z.-S. Wu, S. Pei, W. Ren, D. Tang, L. Gao, B. Liu, F. Li, C. Liu, and H.-M. Cheng, "Field Emission of Single-Layer Graphene Films Prepared by Electrophoretic Deposition," *Advanced Materials*, vol. 21, pp. 1756–1760, May 2009.

[18] Y. Song, D. Hoon Shin, Y.-H. Song, Y. Saito, and C. Jin Lee, "High performance field emission properties of graphite nanoplatelet field emitters," *Applied Physics Letters*, vol. 103, p. 073112, Aug. 2013.

[19] S. Sridhar, C. Tiwary, S. Vinod, J. J. Taha-Tijerina, S. Sridhar, K. Kalaga, B. Sirota, A. H. C. Hart, S. Ozden, R. K. Sinha, Harsh, R. Vajtai, W. Choi, K. Kordás, and P. M. Ajayan, "Field Emission with Ultralow Turn On Voltage from Metal Decorated Carbon Nanotubes," *ACS nano*, vol. 8, pp. 7763–7770, Aug. 2014.

[20] M. Zamri Yusop, G. Kalita, Y. Yaakob, C. Takahashi, and M. Tanemura, "Field emission properties of chemical vapor deposited individual graphene," *Applied Physics Letters*, vol. 104, p. 093501, Mar. 2014.

[21] Y. Zhou, L. Hu, and G. Gr ner, "A method of printing carbon nanotube thin films," *Applied Physics Letters*, vol. 88, p. 123109, Mar. 2006.

[22] J. H. Lee, S. H. Lee, W. S. Kim, H. J. Lee, J. N. Heo, T. W. Jeong, C. W. Baik, S. H. Park, S. Yu, J. B. Park, Y. W. Jin, J. M. Kim, J. W. Moon, M. A. Yoo, J. W. Nam, S. H. Cho, J. S. Ha, T. I. Yoon, J. H. Park, and D. H. Choe, "Current degradation mechanism of single wall carbon nanotube emitters during field emission," *Applied Physics Letters*, vol. 89, p. 253115, Dec. 2006.

[23] Y. Kanazawa, T. Oyama, K. Murakami, and M. Takai, "Improvement in electron emission from carbon nanotube cathodes after Ar plasma treatment," *Journal of Vacuum Science & Technology B: Microelectronics and Nanometer Structures*, vol. 22, no. 3, p. 1342, 2004.

[24] W. Takeuchi, H. Kondo, T. Obayashi, M. Hiramatsu, and M. Hori, "Electron field emission enhancement of carbon nanowalls by plasma surface nitridation," *Applied Physics Letters*, vol. 98, p. 123107, Mar. 2011.

[25] K. . Ohsumi, T. . Honda, W. S. Kim, C. . B. . Oh, K. Murakami, S. . Abo, F. . Wakaya, M. . Takai, S. . Nakata, A. . Hosono, and S. . Okuda, "KrF laser surface treatment of carbon nanotube cathodes with and without reactive ion etching," *Journal of Vacuum Science & Technology B: Microelectronics and Nanometer Structures*, vol. 25, no. 2, p. 557, 2007.

[26] J. G. Ok, B. H. Kim, W. Y. Sung, C. N. Chu, and Y. H. Kim, "Uniformity enhancement of carbon nanofiber emitters via electrical discharge machining," *Applied Physics Letters*, vol. 90, p. 033117, Jan. 2007.

[27] C.-W. Baik, J. Lee, D. S. Chung, J. H. Choi, I.-T. Han, H. J. Kim, S. H. Park, S. I. Kim, Y. W. Jin, J.-M. Kim, J. Y. Kim, S. Yu, K.-H. Jang, and G.-S. Park, "Controlled Vacuum Breakdown in Carbon Nanotube Field Emission," *IEEE Transactions on Nanotechnology*, vol. 6, no. 6, pp. 727–733, 2007.

[28] Liu, Jianlong, Zeng, Baoqing, Wang, Wenzhong, Li, Nannan, Guo, Jing, Fang, Yong, Deng, Jiang, Li, Jiangnan, and Hao, Chenchun, "Graphene electron cannon: High-current edge emission from aligned graphene sheets," *Applied Physics Letters*, vol. 104, p. 023101, Jan. 2014.

[29] A. K. Geim, "Graphene: Status and Prospects," *Science*, vol. 324, pp. 1530–1534, June 2009.

[30] H. Yang, J. Heo, S. Park, H. J. Song, D. H. Seo, K. E. Byun, P. Kim, I. Yoo, H. J. Chung, and K. Kim, "Graphene Barristor, a Triode Device with a Gate-Controlled Schottky Barrier," *Science*, vol. 336, pp. 1140–1143, May 2012.

[31] H. L. Calvo, P. M. Perez-Piskunow, S. Roche, and L. E. F. Foa Torres, "Laser-induced effects on the electronic features of graphene nanoribbons," *Applied Physics Letters*, vol. 101, p. 253506, Dec. 2012.

[32] Y. Fang, B. Luo, Y. Jia, X. Li, B. Wang, Q. Song, F. Kang, and L. Zhi, "Renewing Functionalized Graphene as Electrodes for High-Performance Supercapacitors," *Advanced Materials*, vol. 24, pp. 6348–6355, Sept. 2012.

[33] S. Some, J. Kim, K. Lee, A. Kulkarni, Y. Yoon, S. Lee, T. Kim, and H. Lee, "Highly Air-Stable Phosphorus-Doped n-Type Graphene Field-Effect Transistors," *Advanced Materials*, vol. 24, pp. 5481–5486, Aug. 2012.

[34] U. A. Palnitkar, R. V. Kashid, M. A. More, D. S. Joag, L. S. Panchakarla, and C. N. R. Rao, "Remarkably low turn-on field emission in undoped, nitrogen-doped, and boron-doped graphene," *Applied Physics Letters*, vol. 97, p. 063102, Aug. 2010.

[35] K. S. Novoselov, "Electric Field Effect in Atomically Thin Carbon Films," *Science*, vol. 306, pp. 666–669, Oct. 2004.

[36] R. H. Fowler and L. Nordheim, "Electron Emission in Intense Electric Fields," *Proceedings of the Royal Society A: Mathematical, Physical and Engineering Sciences*, vol. 119, pp. 173–181, May 1928.

[37] S. H. Jo, Y. Tu, Z. P. Huang, D. L. Carnahan, D. Z. Wang, and Z. F. Ren, "Effect of length and spacing of vertically aligned carbon nanotubes on field emission properties," *Applied Physics Letters*, vol. 82, pp. 3520–3522, May 2003.

[38] C. Liu, F. Hao, X. Zhao, Q. Zhao, S. Luo, and H. Lin, "Low temperature reduction of free-standing graphene oxide papers with metal iodides for ultrahigh bulk conductivity," *Scientific Reports*, vol. 4, p. 6203, Feb. 2014.

[39] Y. Xu, K. Sheng, C. Li, and G. Shi, "Self-Assembled Graphene Hydrogel viaa One-Step Hydrothermal Process," *ACS nano*, vol. 4, pp. 4324–4330, July 2010.

[40] J. Kim, W.-H. Khoh, B.-H. Wee, and J.-D. Hong, "Fabrication of flexible reduced graphene oxide-TiO_2 freestanding films for supercapacitor application," *RSC Advances*, vol. 5, no. 13, pp. 9904–9911, 2015.

[41] S. Pei and H.-M. Cheng, "The reduction of graphene oxide," *Carbon*, vol. 50, pp. 3210–3228, Aug. 2012.

[42] C. Li, M. T. Cole, W. Lei, K. Qu, K. Ying, Y. Zhang, A. R. Robertson, J. H. Warner, S. Ding, X. Zhang, B. Wang, and W. I. Milne, "Highly Electron Transparent Graphene for Field Emission Triode Gates," *Advanced Functional Materials*, vol. 24, pp. 1218–1227, Sept. 2013.

[43] Z. Xiao, J. She, S. Deng, Z. Tang, Z. Li, J. Lu, and N. Xu, "Field Electron Emission Characteristics and Physical Mechanism of Individual Single-Layer Graphene," *ACS nano*, vol. 4, pp. 6332–6336, Nov. 2010.

Chapter 6

Conclusion

In this thesis, spectroscopic study on hydration dynamics of the human skin are presented. The sub-structure of palm skin was measured using OCT. The major sub-structures were the multilayered skin and the helical sweat duct in stratum corneum and friction ridge, called fingerprint. In order to obtain dielectric constant of skin layers, the skin is simplified to a dielectric material with a stratum corneum and a epidermal/dermal layer. FDTD results shows that the main reason for determining the reflection spectrum of the skin in the sub-millimeter wave is the Fabry-Perot interference effect due to the multi-layer structure, effect of helical sweat duct are slight. Debye dielectric relaxation theory was adopted to estimate dielectric constant of skin layers.

In terahertz frequency region, it is revealed that the fingerprint structure is the most important structure that can affect the skin reflection spectrum. It is found that the structure of the fingerprint has resonance in the terahertz frequency range. We found that the change of resonance with time has a strong correlation with the humidity around the finger. It is shown that this resonance varies with time, which is strongly correlated with the humidity around the finger. On the other hand, It is observed that the touch friction force was kept constant despite the continuous increase in the amount of moisture adsorbed to the fingerprint due to occlusion. Taken together with

the frictional force optimization when the hydration level of ridge portion of friction ridge saturated, it implies that the fingerprint structure might helps to keep the friction force constant by controlling moisture in touch action.

In order to expend terahertz wave to general skin applications, a vertically aligned freestanding graphene-based film field emitter was synthesized. Owing to its high aspect ratio with a thin film geometry, a significantly high current of more than 7 mA was obtained from a single field emitter with high current density (approximately 200 A/cm2). The synthesized rGO films exhibited high robustness, sufficient for mechanical shaping, which is essential for obtaining uniform emission surfaces by removing the remaining small protrusions through field-induced electrical material evaporation. A controlled electrical aging process was performed to uniformize the emission edges of the rGO films, resulting in a uniform emission current and a highly-stable emission for a duration longer than 40 days, under a continuous operation condition with a negligible current degradation, less than 5% of the average emission current. This graphene-based electron beam emitter will accelerate the realization of compact high power terahertz source applicable to skin as well as existing applications such as field emission.

Appendix

MATLAB Code : Fast Fourier Transform

```
function [S11] = FFT_tmp(TDR)
%%
Source = load('85_105GHz_signal.txt');
Source = interp1(Source(:,1),Source(:,2),TDR(:,1),'line');
dt = TDR(2,1) - TDR(1,1);
FL = 1/dt;
TL = length(TDR(:,2));
TDR = TDR(:,2);
Extend = zeros(9*TL,1);
TDR = [TDR;Extend];
Source = [Source;Extend];
S11(:,1) = (linspace(0,FL,length(TDR)))';
S11(:,2) = fft(TDR)./fft(Source);
```

MATLAB Code : Inverse Fast Fourier Transform

```
function [TDR] = IFFT_tmp
%%
[filename, pathname] = uigetfile({'*.txt';},'S11 Data');
cd(pathname);
sample = load(filename);
%%
source = load('85_105GHz_signal.txt');
Time = source(:,1);
Source = source(:,2);
Freq = sample(:,1);
S11 = sample(:,2) + 1i*sample(:,3);
TL = 1/(Time(2) - Time(1));
FL = 1/(Freq(2) - Freq(1));
%%
Source = fft(Source);
Freq_Source = ( linspace(0, TL, length(Source)) )';
Source = interp1(Freq_Source,Source,Freq,'line');
S11 = Source.*S11;
F0_Mesh = fix( length(Freq)*Freq(1) / (Freq(end)- Freq(1)) );
Extend_F = zeros(F0_Mesh,1);
Extend = zeros(30*F0_Mesh,1);
Source = [Extend_F; Source; Extend];
S11 = [Extend_F; S11; Extend];
Source = [Source;flipud(Source)];
S11 = [S11;flipud(S11)];
TDR = ifft(S11);
Nomalize = 1/max(abs(real(ifft(Source))));
TDR(:,2) = real(TDR*Nomalize);
TDR(:,1) = (linspace(0,FL,length(TDR)))';
TDR = CUT(TDR,0,2.0);
```

MATLAB Code : Time Domain Reflectometry

```
clear all; clc; clf; tic;
%%%%%%%%%%%%
% set file path
cd 'file_path'
%%%%%%%%%%%%
% S11 data load (type: freq(GHz), real, image)
sample = load('result.dat');
%%%%%%%%%%%%
% time range setup (set resolution = 0.0001 ns)
t_i = 0; %(ns)
t_f = 50; %(ns)
t_stop = 50; % magnification of ungated time domain signal
n_cycle =30;
%%%%%%%%%%%%
% making S11
freq = sample(:,1);
s11 = sample(:,2) + sample(:,3).*1i;
%%%%%%%%%%%%
% excitation signal
fc=(freq(1)+freq(end))/2; % center freq
bw=(fc-freq(1))/fc; % bandwith
tc = gauspuls('cutoff',fc,bw,[],-100);  % excitation time/2
fs = 20*freq(end);          %sampling frequency
ts = 1/fs;                  % sampling time
fa = freq(2)-freq(1);       % analysis frequency
n = 10*freq(end)/fa;        % point # of excitation signal
time = 0 : ts : (n-1)*ts; % time array
source_amp = gauspuls(time - tc,fc,bw); % excitation signal
%%%%%%%%%%%%
% n_cycle
% time array
source_amp_n = zeros(length(source_amp)*n_cycle,1);
    for j=1:length(source_amp)
    source_amp_n(j) = source_amp(j);
```

```
    end
%%%%%%%%%%%%
% source FFT
source_fft = fft(source_amp_n);
dt = time(2) - time(1);
f_max = 1/(2*dt);
f_range_new = (linspace(0,2*f_max,length(source_amp_n)))';
source_fft1=interp1(f_range_new,source_fft,freq,'spline');
%%%%%%%%%%%%
% ffted tdr signal
tdr_fft = source_fft1.*s11;
%%%%%%%%%%%%
% expend ffted tdr for ifft
aa = find(freq(1)<f_range_new,1);
bb = find(freq(end)<f_range_new,1)-1;
for i=aa:bb
    f_range_new_sub(i-aa+1) = f_range_new(i);
end
tdr_fft1= interp1(freq,tdr_fft,f_range_new_sub,'spline');
tdr_tot = zeros(length(source_fft),1);
for i=aa:bb
    tdr_tot(i) = tdr_fft1(i-aa+1);
    tdr_tot(length(tdr_tot)-i) = tdr_fft1(i-aa+1);
end
%%%%%%%%%%%%
% ifft & set time domain
w1 = 1;
yt = ifft(w1.*tdr_tot,length(tdr_tot));
yt_source = ifft(w1.*source_fft,length(source_fft));
t_max = 1/(f_range_new(2)-f_range_new(1));
time_new = (linspace(0,t_max,length(yt_source)))';
%%%%%%%%%%%%
% set the time gate
time_gate_sample = zeros(length(yt),1);
aa = find(t_i<time_new,1);
bb = find(t_f<time_new,1)-1;
for i=aa:bb
```

```
    time_gate_sample(i) = yt(i);
    time_gate_sample(length(tdr_tot)-(i))
    = yt(length(tdr_tot)-(i));
end
sample_fft = fft(time_gate_sample);
s11_new = sample_fft./source_fft;
s11_gated = interp1(f_range_new,s11_new,freq,'spline');
%%%%%%%%%%%
% Save option for s11_mod
s11_mod(:,1) = freq;
s11_mod(:,2) = real(s11_gated);
s11_mod(:,3) = imag(s11_gated);
r_VNA =abs(s11);
r = abs(s11_gated);
phase1 = unwrap(angle(s11).*180./pi);
phase2 = unwrap(angle(s11_gated).*180./pi);
toc;
results_s(:,1) = freq;
results_s(:,2) = r;
results_t(:,1) = time_new;
results_t(:,2) = abs(2*(yt));
subplot(2,2,1); plot(time_new,abs(2*(yt)))
title('Reflected signal');
xlim([0, t_stop]);
xlabel('Time (ns)'); ylabel('Linear magnitude');
subplot(2,2,2); plot(time_new,real(2*time_gate_sample))
title('Gated signal');
xlim([t_i, t_f]);
xlabel('Time (ns)'); ylabel('Linear magnitude');
subplot(2,2,3); plot(freq,r_VNA,'-',freq,r,'--')
title('S-parameter magnitude');
xlim([freq(1), freq(end)]);
xlabel('Frequency (GHz)'); ylabel('Linear magnitude');
subplot(2,2,4); plot(freq,phase1,'-',freq,phase2,'--')
title('Unwraped phase');
xlim([freq(1), freq(end)]);
xlabel('Frequency (GHz)'); ylabel('Dgree');
```

MATLAB Code : Debye Fitting for Two Layer Skin Model (Main Code)

```
% A program to find parameter values of a Debye model
% function providing the best fit to measured
% reflection data.
clear all;
clc;
clf;
tic
% INPUT DATA
% Setpath
format short
cd 'path'
aa = load('data.txt');
xdata = (1000*aa(:,1))';
ydata = aa(:,2)';
reference = [3.63; 9.7; 0; 6.9; 4.52; 27.2; 1.4; 7; 300];
lb = [2; 3; 0; 0; 2; 3; 0; 0; 250];
ub = [10; 15; 2; 10; 40; 200; 10; 40; 350];
x0 = (lb+ub)./1.8;
tic;
[x,resnorm] = lsqnonlin(@(x)reflec_skin(x,xdata,ydata),x0)
toc;
a = myfun1(x,xdata,0);
avg = mean(ydata);
temp1 = sum((a-avg).^2);
temp2 = sum((a-ydata).^2);
r_quare = 1.0 - temp2/temp1;
str1 = num2str(r_quare);
str2 = 'R^2 = ';
str = [str2 str1];
bb(:,1) = lb;
bb(:,2) = round(x.*100);
bb(:,2) = bb(:,2)./100;
bb(:,3) = ub;
```

```
bb(:,4) = reference;
display(r_quare)
display(bb(:,2))
subplot(2,1,1)
plot(xdata,ydata,'-',xdata, a,'--')
xlabel('Frequency (GHz)')
ylabel('Reflection Coefficient')
title('\it{TDS Measurement : skin measurement}','FontSize',16)
annotation('textbox', [ .3, .7, .1, .1], 'String', str);
dat = bb;
cnames = {'Lower Bound','Fitting Value',
'Upper Bound','Reference'};
rnames = {'1st e_inf','1st delta_e','1st cond.','1st tau.'
,'2nd e_inf','2nd delta_e','2nd cond.',
'2nd tau.','1st thickness'};
t = uitable('Data',dat,'ColumnName',cnames,
'RowName',rnames,'Position',[80 100 435 175]);
```

MATLAB Code : Debye Fitting for Two Layer Skin Model (Function Code)

```
function F = reflec_skin(x,xdata,ydata)
    e_win = 3.75;
    Eo = 8.854191;
    tau1 = 1+1i.*2.*pi.*xdata.*x(4)./10^3;
    tau2 = 1+1i.*2.*pi.*xdata.*x(8)./10^3;
    Eo_new = 1i.*2.*pi.*xdata.*Eo./10^3;
    k0 = 2.*pi.*10.*xdata./2.997;

    e1 = x(1) + x(2)./tau1 + x(3)./Eo_new;
    e2 = x(5) + x(6)./tau2 + x(7)./Eo_new;

    k1 = k0.*sqrt(e1);

    r0 = (sqrt(e_win) - sqrt(e1))./(sqrt(e_win) + sqrt(e1));
    r1 = (sqrt(e1) - sqrt(e2))./(sqrt(e1) + sqrt(e2));

    gamma1 = exp(-2.*1i.*k1.*(x(9)/1000000));

    rc = abs((r0+r1.*gamma1)./(1+r1.*r0.*gamma1))-ydata;
    F = rc;
end
```

Publication List

[1] **I.-K. Baek**, R. Bhattacharya, J. S. Lee, S. Kim, D. Hong, M. A. Sattorov, S.-H. Min, Y. H. Kim, and G.-S. Park, "Uniform high current and current density field emission from the chiseled edge of a vertically aligned graphene-based thin film," *Journal of Electromagnetic Waves and Applications*, vol. 420, pp. 1–10, July 2017.

[2] **I.-K. Baek**, M. Sattorov, R. Bhattacharya, S. Kim, D. Hong, S.-H. Min, and G.-S. Park, "Origin of Sideband and Spurious Noises in Microwave Oven Magnetron," *IEEE Trans. Electron Devices*, vol. PP, no. 99, pp. 1–8, 2017.

[3] S.-H. Min, O. Kwon, M. Sattorov, **I.-K. Baek**, S. Kim, J.-Y. Jeong, D. Hong, S. Park, and G.-S. Park, "Miniaturized two-stack Blumlein pulser with a variable repetition-rate for non-thermal irreversible-electroporation experiments," *Review of Scientific Instruments*, vol. 88, pp. 014704–11, Jan. 2017.

[4] S.-H. Min, O. Kwon, M. Sattorov, H. Jung, **I.-K. Baek**, S. Kim, A. Bera, R. K. Barik, R. Bhattacharya, and G.-S. Park, "Design Study of GW-THz Wave Transmission Without Mode Competition in an Oversized Relativistic Backward Wave Oscillator," *Plasma Science, IEEE Transactions on*, vol. 45, no. 4, pp. 610–622, 2017.

[5] S.-H. Min, O. Kwon, M. Sattorov, H. Jung, S.-H. Shin, **I.-K. Baek**, S. Kim, S. Park, and G.-S. Park, "Characteristics of a transient axial mode from the formation of anode plasma in a gigawatt-class L-band magnetically insulated transmission line oscillator," *Physics of Plasmas*, vol. 23, p. 063120, June 2016.

[6] K. Lee, J. Jeong, Y.-M. Bahk, J. Rhie, **I.-K. Baek**, B. J. Lee, Y. H. Kang, S. Hong, G.-S. Park, and D.-S. Kim, "Microwave Funneling through Sub-10 nm Nanogaps," *ACS Photonics*, vol. 3, pp. 537–542, Apr. 2016.

[7] M. Sattorov, E. Khutoryan, K. Lukin, O. Kwon, S.-H. Min, R. Bhattacharya, **I.-K. Baek**, S. Kim, M. Yi, J. So, and G.-S. Park, "Automodulation Processes in Clinotrons With Low-Focusing Magnetic Field," *IEEE Trans. Electron Devices*, vol. 62, no. 5, pp. 1617–1621, 2015.

[8] E. Khutoryan, M. Sattorov, K. A. Lukin, O.-J. Kwon, S.-H. Min, R. Bhattacharya, **I.-K. Baek**, S. Kim, M. Yi, J. So, and G.-S. Park, "Theory of Multimode Resonant Backward-Wave Oscillator With an Inclined Electron Beam," *IEEE Trans. Electron Devices*, vol. 62, no. 5, pp. 1628–1634, 2015.

[9] O. Kwon, M. Sattorov, S.-H. Min, **I.-K. Baek**, S. Kim, A. Bera, R. K. Barik, R. Bhattacharya, J.-Y. Jeong, J.-H. Won, and G.-S. Park, "Efficient terahertz oscillation using a half-period staggered grating resonator," *Japanese Journal of Applied Physics* vol. 53, no. 6, p. 066201, 2014.

[10] A. Bera, R. K. Barik, M. Sattorov, O. Kwon, S.-H. Min, **I.-K. Baek**, S. Kim, J.-K. So, and G.-S. Park, "Surface-coupling of Cerenkov radiation from a modified metallic metamaterial slab via Brillouin-band folding," *Optics Express*, vol. 22, no. 3, p. 3039, 2014.

[11] R. K. Barik, A. Bera, R. S. Raju, A. K. Tanwar, **I. K. Baek**, S. H. Min, O. J. Kwon, M. A. Sattorov, K. W. Lee, and G. S. Park, "Development of alloy-film coated dispenser cathode for terahertz vacuum electron devices application," *Applied Surface Science*, vol. 276, pp. 817–822, July 2013.

[12] R. K. Barik, A. Bera, A. K. Tanwar, **I. K. Baek**, and S. H. Min, "A novel approach to synthesis of scandia-doped tungsten nano-particles for high-current-density cathode applications," *International journal of Refractory Metals and Hard Materials*, 2013.

국문초록

본 연구의 목적은 서브 테라헤르츠 및 테라헤르츠파 주파수 범위의 손바닥 피부의 분광 특성을 이해하고, 추후 피부에 적용 가능한 소형 고출력 테라헤르츠파 발생원을 위한 새로운 전자빔 소자를 개발하는 것이다. 피부에 대한 연구는 주로 생리 현상으로 인한 피부 표면 및 피부층의 유전 특성 변화뿐만 아니라 주로 손바닥 피부의 구조적 특성으로 인한 서브테라헤르츠 및 테라헤르츠파의 특성을 이해하는 것에 중점을 두었다. 스펙트럼에 영향을 줄 수 있는 손바닥 피부의 하위구조인 각질층, 표피층, 진피층의 두께 및 나선형 땀샘관과 지문의 구조를 광간섭 단층촬영(Optical Coherence Tomography) 를 이용하여 측정하였다. 각각의 피부층의 유전율은 드바이(Debye) 유전완화모델을 기반한 피팅모델로 추정하였다. 또한 지문구조가 테라헤르츠파 주파수 영역에서 공진을 갖는 구조이며, 공진이 교합에 의해 변조되는 것을 관측하였다. 테라헤르츠 공진 주파수의 모니터링을 통해 피부가 물체와 접촉시 발생하는 교합에 의한 지문 각질층의 수화다이나믹스를 분석하였다. 지문구조의 각 부분에 대한 수화동역학의 실험적 관측결과는 지문의 구조가 수화조절을 통해 손가락 마찰력에 영향을 줄 수 있는 구조임을 암시한다.

이렇듯 테라헤르츠파가 피부의 생리적 특성진단에 매우 중요한 도구이지만 피부 연구 및 응용에 적용 가능한 소형 고출력 발생원이 부족한 것이 매우 큰 문제이다. 이를 해결하기 위해서 테라헤르츠파 발생원을 위한 그래핀 기반 전자빔 소자를 제작하였다. 제작된 그래핀 필름은 뛰어난 역학 강인도로 인하여 정밀하게 제단할 수 있으며 높은 종횡비를 가지는

모서리 부분을 통해 장시간 동안 균일한 전자빔 방출특성을 보였다. 해당 전자빔 소자는 전계방출 디스플레이, 전자 현미경등의 기존 응용범위 뿐 아니라 피부에 적용가능한 소형 고출력 테라헤르츠 발생원 실현을 앞당길 것이다.

주요어 : 피부 유전율, 테라헤르츠 분광학, 피부수화, 지문, 그래핀 전계 방출 음극

학번 : 2009-20412